

**Eigenspannungsanalyse und Ermüdungsverhalten
von mechanisch oberflächenbehandelten
Titanlegierungen**

**Dissertation
zur Erlangung des Doktorgrades
der Ingenieurwissenschaften**

**vorgelegt von
Emad Kamel Soliman Maawad, M.Sc.
Aus Alexandria, Ägypten**

**genehmigt von der Fakultät für Natur- und Materialwissenschaft
der Technischen Universität Clausthal
Deutschland**

**Tag der mündlichen Prüfung
23.04.2012**

Vorsitzender der Promotionskommission: Prof. Dr.-Ing. habil. Joachim Deubener

Hauptberichterstatter: Prof. Dr. rer. nat. Dr.-Ing. habil. Heinz-Günter Brokmeier

Mitberichterstatter: Prof. Dr.-Ing. habil. Lothar Wagner

**Residual Stress Analysis and Fatigue Behavior of
Mechanically Surface Treated Titanium Alloys**

Dissertation

**To be awarded the degree
Doctor of Engineering (Dr.-Ing.)**

Submitted by

**Emad Kamel Soliman Maawad, M.Sc.
from Alexandria, Egypt**

**Approved by the Faculty of Natural and Materials Science
Technical University of Clausthal
Germany**

**Date of oral examination
23.04.2012**

Chairperson of the Board of Examiners: Prof. Dr.-Ing. habil. Joachim Deubener

Chief Reviewer: Prof. Dr. rer. nat. Dr.-Ing. habil. Heinz-Günter Brokmeier

Reviewer: Prof. Dr.-Ing. habil. Lothar Wagner

Preface

This thesis has been submitted in partial fulfilment of the requirements for a doctoral degree in the Faculty of Natural and Materials Science of Clausthal University of Technology in Germany. This research was carried out between November 2007 and October 2011 in the framework of a project supported by the German Research Foundation (DFG) through BR 961/5-2 and WA 692/32-2. This project aimed at enhancing the fatigue performance of various titanium alloys by performing various mechanical surface treatments. The process-induced residual stresses were evaluated by using diffraction methods. I am indebted to the German Research Foundation for financial support. It is a pleasure to thank Prof. Dr. H.-G. Brokmeier for giving me a chance to achieve my doctoral research under his great supervision and Prof. Dr. L. Wagner for reviewing my thesis. I am very grateful for their helps and valuable discussions during my work. I would also like to thank Dr. M. Wollmann for his help.

I acknowledge the Helmholtz-Zentrum Berlin – Electron storage ring BESSY II for provision of synchrotron radiation at beamline EDDI and I would like to thank Prof. Dr. Ch. Genzel and Dr. M. Klaus for assistance. The research leading to these results has received funding from the European Community's Seventh Framework Program (FP7/2007-2013) under grant agreement No. 226716. I also acknowledge the Forschungsneutronenquelle Heinz Maier-Leibnitz in Garching (FRM II) for using neutron diffraction at beamline STRESS-SPEC. I would like to thank Dr. M. Hofmann and Dr. W. Gan for assistance. In addition, I would like to show my gratitude to the Helmholtz-Zentrum Geesthacht for measuring the global crystallographic texture by using neutron diffraction at beamline TEX-2 as well as to Deutsches Elektronen-Synchrotron (DESY) in Hamburg for carrying out in situ tensile testing, micro-computed tomography and phase analysis measurements by using synchrotron radiation. I would like to thank Dr. F. Beckmann, Mr. C. Randau, Mr. B. Schwebke and Mr. M. Jiang for assistance.

Furthermore, I owe my deepest gratitude to Dr. Y. Sano of Toshiba Corporation, Japan, for performing laser shock peening, Dr. M. Mhaede of IWW for his help in performing shot peening as well as Mr. H. Polanetzki of MTU Aero Engines GmbH, Munich, for providing ultrasonic shot peening treatments.

I would like to show my gratitude to Mr. P. König, Mr. U. Körner, Mr. J. Schumann and Mr. U. Hanke for sample machining and metallographic preparation of numerous samples.

I owe my deepest gratitude to Prof. Dr. A. El-Ashram, Prof. Dr. M. Hamed and Prof. Dr. I. Abdullah of the production engineering department, Alexandria university in Egypt for their supervisions and valuable discussions during my whole research work in Egypt.

Finally, I am indebted to my parents, my brother and my sister for their supports during my study.

Clausthal-Zellerfeld, October 2011

Emad Kamel Soliman Maawad

Publications

- 2012** E. Maawad, Y. Sano, L. Wagner, H.-G. Brokmeier, Ch. Genzel, *Int. Journal of Materials Science and Engineering A* 536 (2012) 82–91.
- 2011** E. Maawad, H.-G. Brokmeier, L. Wagner, Y. Sano, Ch. Genzel, *Int. Journal of Surface and Coatings Technology* 205 (2011) 3644–3650.
- K. Zay, E. Maawad, H.-G. Brokmeier, L. Wagner, Ch. Genzel, *Int. Journal of Materials Science and Engineering A* 528 (2011) 2554–2558.
- E. Maawad, H.-G. Brokmeier, L. Wagner, Ch. Genzel, M. Klaus, ICSP-11, South Bend, Indiana, USA, 12–16 September 2011, pp 147–152.
- 2010** E. Maawad, H.-G. Brokmeier, M. Hofmann, Ch. Genzel, L. Wagner, *Int. Journal of Materials Science and Engineering A* 527 (2010) 5745–5749.
- E. Maawad, H.-G. Brokmeier, L. Wagner, *Solid State Phenomena* Vol. 160 (2010) pp 141–146.
- W.M. Gan, E. Maawad, H. Chang, G.D. Fan, C. Randau, M.Y. Zheng, Wu, H.-G. Brokmeier, *Solid State Phenomena* Vol. 160 (2010) pp 117–121
- K. Wu, H. Chang, E. Maawad, W.M. Gan, H.G. Brokmeier, M.Y. Zheng, *Int. Journal of Materials Science and Engineering A* 527 (2010) 3073–3078
- 2009** H. Chang, M.Y. Zheng, W.M. Gan, K. Wu, E. Maawad, H.G. Brokmeier, *Scripta Materialia*, 61–72 (2009) 717–720.
- E. Maawad, H.-G. Brokmeier, L. Wagner and Ch. Genzel, PEDAC'2009, 10 -12 February 2009, Alexandria, Egypt.
- E. Maawad, S. Yi, H.-G. Brokmeier, M. Wollmann, L. Wagner, ICSP-10, Tokyo, Japan, 15–18 September 2009, pp 499–504.

Abstract

Recently, titanium alloys are extensively used in the aerospace field such as jet-engine blades and emerging fields such as tools and sport products for their superior mechanical properties. These components are subjected to fatigue and could fail due to flaws or cracks initiated on the surface. Therefore, surface layer properties of the components such as compressive layer play a major role in the fatigue performance. Compressive residual stresses on the surface retard the growth of surface-initiated cracks to which greatly prolongs the component life. Several processes are available for introducing beneficial compressive residual stresses to component surface layers to increase the fatigue performance. The most common of these methods is shot peening, but other emerging techniques such as laser shock peening and low plasticity burnishing are receiving increased attention. As a result of this variety of mechanical surface treatments, study of the influence of the surface layer properties on the fatigue performance of titanium alloys is becoming increasingly important in a variety of industrial fields. This is to achieve more gains by balancing between optimum conditions and costs. In the present study, shot peening (SP), ball-burnishing (BB), laser shock peening without coating (LPwC) and ultrasonic shot peening (USP) processes were performed on the α titanium alloy Ti-2.5Cu. Only in the past two decades there has been an increased interest in laser peening technology for applications ranging from aeronautic to automotive fields. Currently, major gas-turbine manufacturers brought in laser shock peening to improve fatigue performance of critical parts of engine components. Therefore, in the present work, the influence of LPwC on the residual stresses state and fatigue performance of the $\alpha + \beta$ titanium alloy TIMETAL 54M (in the following Ti-54M) as well as β titanium alloy TIMETAL LCB (in the following LCB) beside Ti-2.5Cu was also studied. The LPwC results were compared with SP, USP, and BB results. The high cycle fatigue (HCF) results were interpreted by examining the changes of fatigue crack nucleation site, surface morphology, work hardening and residual stress produced in the surface layer. Results indicate that the HCF performance of Ti-2.5Cu and LCB was more enhanced after LPwC compared to that after SP, while it was deteriorated in Ti-54M. BB resulted in much superior HCF performance of Ti-2.5Cu than SP or LPwC.

The non-destructive depth profiles of compressive and balancing tensile residual stresses were evaluated by combining laboratory or angle-dispersive X-ray diffraction using Cu-K α_2 -radiation (Lab-XRD) and energy-dispersive X-ray diffraction using synchrotron radiation (ED-XRD). Neutron diffraction was, in addition, used to evaluate the balancing tensile

residual stresses and zero-crossing depths (where the residual stress value of zero is reached) in Ti-2.5Cu after SP and BB as well as the penetration depths of compressive layers.

Thermal stability of residual stresses in surface treated Ti-2.5Cu was evaluated after annealing at various temperatures and exposure times by means of a Zener-Wert-Avrami-approach. The incremental hole drilling method was used for residual stress relaxation analysis. Results revealed that the compressive residual stress is thermally more stable in the surface layer after LPwC than that after SP, USP or BB. Changes of work hardening in the surface layers after each surface treatment were obtained by measuring microhardness and calculating full width at half maximum (FWHM) of a diffraction peak.

Local texture changes during mechanical surface treatments might affect surface and near-surface properties, such as the resistance to fatigue crack growth. Therefore, it was necessary to measure a local texture by using Lab-XRD compared with a bulk texture that was measured by neutron diffraction. To understand the role of the second phase Ti₂Cu in the texture components, in situ measurement of the texture variation was carried out by using monochromatic synchrotron X-ray radiation. It was observed that the local texture was changed during surface treatments.

Nomenclature and Abbreviations

Symbol	Description	Unit
c	Speed of light	[m/s]
$d_{0(hkl)}$	Unstrained interplanar spacing	[Å]
$d_{(hkl)}$	Strained Interplanar spacing	[Å]
E	Modulus of elasticity	[GPa]
$E_{(hkl)}$	Energy	[keV]
El	Elongation	[%]
F	Force	[N]
h	Planck's constant	[eV.s]
R	Stress ratio	
RS	Residual stress	[MPa]
Rz	Average absolute value of the five highest peaks and the five lowest valleys over the evaluation length	[µm]
N_f	Number of cycles to failure	[cycles]
S_1 & $\frac{1}{2} S_2$	Diffraction elastic constants	[MPa ⁻¹]
T	Temperature	[°C]
t	Time	[s] or [hr]
UTS	Ultimate tensile stress	[MPa]
2θ	Scattering angle	[°]
λ	Wavelength	[Å]
$\sigma_{0.2}$	Yield strength	[MPa]
σ_a	Stress amplitude	[MPa]
σ_m	Mean stress	[MPa]
σ_x	In-plane residual stress component perpendicular to rolling direction	[MPa]
σ_y	In-plane residual stress component parallel to rolling direction	[MPa]
σ_z	Residual stress normal to the surface	[MPa]
τ	Average penetration depth	[µm]
τ_{max}	Maximum penetration depth	[µm]

τ_{\min}	Minimum penetration depth	[μm]
φ	Rotation angle of sample	[$^{\circ}$]
ψ	Tilting angle of sample	[$^{\circ}$]

Phase	Description
α	Alpha phase of Ti-alloys with hcp crystal structure
β	Beta phase of Ti-alloys with bcc crystal structure

Abbreviation	Description
AMSS	Anomalous mean stress sensitivity
BB	Ball-burnishing
ED-XRD	Energy dispersive X-ray diffraction
EP	Electropolishing
EQ	Equiaxed
FWHM	Full width at half maximum
IHD	Incremental hole drilling
Lab-XRD	Laboratory X-ray diffraction
LCB	Low cost beta titanium alloy
LPwC	Laser shock peening without coating
LSP	Laser shock peening with coating
m.r.d	Multiple of random density
ODF	Orientation distribution function
RD	Rolling direction
RT	Room temperature
SEM	Scanning electron microscope
SHT	Solid heat treated
SHT + A	Solid heat treated followed by aging
SP	Shot peening
SR μ CT	Synchrotron radiation micro-computed tomography
TD	Transverse direction
USP	Ultrasonic shot peening

Table of Contents

1	Introduction and Aims	1
1.1	Introduction.....	1
1.2	Aims and Objectives.....	2
2	Literature Survey	5
2.1	Introduction.....	5
2.2	Titanium and its Alloys.....	5
2.2.1	Classification of Titanium alloys.....	7
2.3	Improvement of the Fatigue-Life by Mechanical Surface Treatments.....	9
2.3.1	Conventional Shot Peening Process.....	9
2.3.2	Ultrasonic Shot Peening.....	11
2.3.3	Burnishing Process.....	12
2.3.4	Laser Shock Peening.....	13
2.3.5	Surface Mechanical Attrition Treatment.....	15
2.4	The Influence of Mean Stress Sensitivity, Environment and Residual Stress on Titanium alloys.....	16
2.4.1	Mean Stress Sensitivity.....	16
2.4.2	Environmental Sensitivity.....	18
2.4.3	Residual Stress.....	18
2.5	Residual Stress Determination by Diffraction Methods.....	20
2.5.1	X-Ray Diffraction.....	21
2.5.2	Neutron Diffraction.....	26
2.6	Thermal Relaxation of Residual Stress.....	28
2.7	Deformation Behavior of Titanium and its Alloys.....	29
2.8	Crystallographic orientation.....	30
2.8.1	Description of the orientation.....	31
2.8.2	Texture Measurement.....	35
2.9	Texture in Ti-Cu alloy compared with other in hcp metals.....	36
2.10	Microtomography.....	37
2.10.1	X-Ray Microtomography.....	37
2.10.2	Neutron Microtomography.....	38
3	Materials and Methods	41
3.1	Introduction.....	41
3.2	Materials.....	41

3.3	Surface Treatments.....	42
3.4	Surface roughness	44
3.5	Microhardness	44
3.6	Residual Stress and Full Width at Half Maximum	44
3.6.1	Laboratory X-ray Diffraction (Lab-XRD)	44
3.6.2	Energy-Dispersive X-ray Diffraction using Synchrotron Radiation	46
3.6.3	Neutron Diffraction.....	51
3.6.4	Incremental Hole Drilling Method (IHD)	54
3.7	Crystallographic Texture.....	55
3.7.1	Local Crystallographic Texture Using Lab-XRD	55
3.7.2	Bulk Texture.....	55
3.8	Phase Analysis by Using Monochromatic Synchrotron Radiation	57
3.9	Synchrotron Radiation Micro-Computed Tomography (SR μ CT)	57
3.10	Fatigue Testing.....	58
4	Results and Discussions	61
4.1	Introduction.....	61
4.2	Microstructures and Phase Analysis	61
4.3	Surface Morphology.....	64
4.4	Microhardness-Depth Profiles	67
4.5	Residual Stress-Depth Profiles.....	71
4.5.1	Surface and Near-Surface Residual Stress by X-Ray Diffraction.....	71
4.5.2	Residual Stress Distribution by Combining X-Ray and Neutron Diffraction..	76
4.5.3	Thermal Stability of Residual Stress after Mechanical Surface Treatments....	80
4.6	High Cycle Fatigue Performance	86
4.7	Change of Local Crystallographic Texture after Various Surface Treatments.....	93
4.7.1	Global Crystallographic Texture.....	93
4.7.2	Texture Variation in the Mechanically Surface Treated Layers	96
	Conclusions and Recommendations	101
	References	103

1 Introduction and Aims

1.1 Introduction

Mitigation against the failure of engineering components exposed to cyclic loading below the ultimate yield strength (fatigue) can be achieved by applying conventional mechanical surface treatments such as shot peening (SP) or ball-burnishing (BB) as well as novel ones such as laser shock peening (LSP) or ultrasonic shot peening (USP). This is mainly result of induced plastic deformation and compressive residual stress in a surface layer. This compressive residual stress is balanced by tensile residual stresses generated below compressive layers. It is well known that rotating beam loading leads to a stress gradient in radial direction of a round sample. Therefore, the stress amplitude has a maximum on the sample surface and diminishes towards the sample axes, where the stress amplitude becomes zero for stress ratio $R = -1$ as illustrated schematically in Fig. 1.1a.

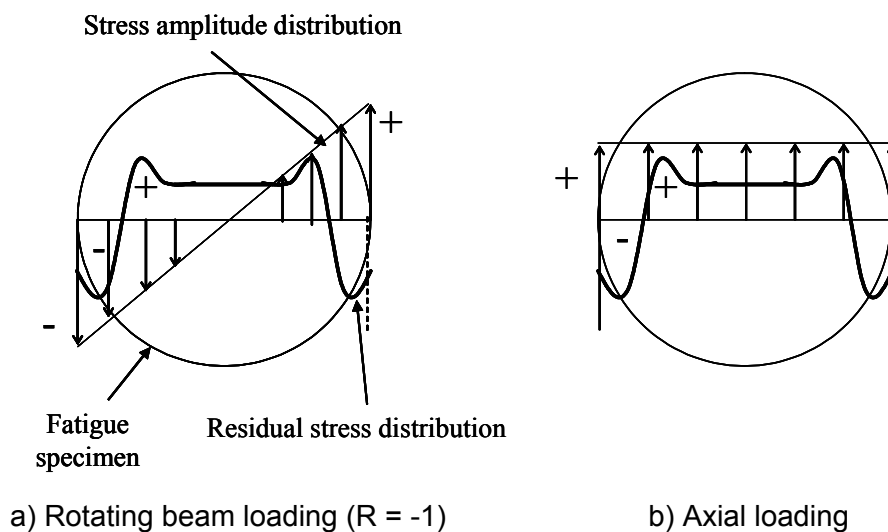


Figure 1.1: Schemes showing stress amplitude and residual stress distributions in round fatigue samples under rotating (a) and axial (b) beam loading.

Under this loading condition, the tensile residual stresses (far below the surface) might have no significant influence on the fatigue properties. On the other hand, axial loading with a homogeneous stress distribution (Fig. 1.1b) might lead to different results regarding to different balancing tensile residual stress distributions.

In order to study the role of residual stresses in fatigue performance, it is essential to determine firstly both compressive and balancing tensile residual stresses. Due to greater

penetration depths, diffraction methods such as X-ray and/or neutron diffraction should be used. Neutrons have relatively greater penetration depth in order to determine the residual stress in core regions, while X-ray diffraction is useful for near-surface stresses.

Anisotropic residual stresses could be obtained in the surface layer after performing mechanical surface treatments due to a severe plastic deformation. This could result in a local change of grain orientations or crystallographic texture and, therefore, might affect surface and near-surface properties such as the resistance to fatigue crack growth. X-ray diffraction is a useful tool to measure local textures developed in surface layers, while a bulk texture can be measured by using neutron diffraction.

1.2 Aims and Objectives

- Study the influence of novel surface treatments, such as laser shock peening without coating (LPwC) and USP, as well as conventional ones, such as SP and BB, on the high cycle fatigue (HCF) performance of Ti-2.5Cu, crack nucleation sites, surface topography, work hardening and residual stresses.
- Recently, major gas-turbine manufacturers brought in laser shock peening to improve fatigue performance of fatigue critical parts of engine components (e.g., engine blades). Therefore, in the present work, the influence of LPwC on the residual stresses state and fatigue performance of the $\alpha + \beta$ titanium alloy TIMETAL 54M (in the following Ti-54M), β titanium alloy TIMETAL LCB (in the following LCB) as well as Ti-2.5Cu was studied.
- Non-destructive residual stress analysis by combining laboratory X-ray, energy-dispersive X-ray and neutron diffraction in order to accurately determine both compressive and balancing tensile residual stresses induced in the core region of Ti-2.5Cu after performing mechanical surface treatments.
- Study the role of balancing tensile residual stress in fatigue performance.
- Investigation of the influence of pre-residual stress state on the residual stress distribution after applying mechanical surface treatments.
- Independent evaluation of generated residual stresses in α - and β -phases of LCB after LPwC by using energy-dispersive X-ray diffraction.

- Study whether there is any influence of the tensile residual stress to open cracks produced by manufacturing processes. This investigation was carried out by using synchrotron radiation micro-computed tomography.
- Investigation of thermal stability of residual stresses generated by SP, BB, USP and LPwC by annealing several samples of aged Ti-2.5Cu at different temperatures for different times by means of a Zener-Wert-Avrami approach.
- Texture evolution during plastic deformation by in situ tensile testing using synchrotron radiation in order to understand the role of the second phase Ti₂Cu in changes of the texture component(s).
- Study the changes of the local textures in the surface layers after applying various surface treatments by using laboratory X-ray diffraction.

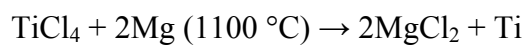
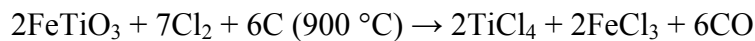
2 Literature Survey

2.1 Introduction

The main target of this chapter is to briefly introduce a literature survey on classification of titanium alloys and various methods of mechanical surface treatments to enhance the fatigue performance. Furthermore, a brief introduction to residual stresses, crystallographic textures as well as crack distributions by using microtomography is given.

2.2 Titanium and its Alloys

Titanium (Ti) is a low-density metallic element that is plentiful in the earth crust in mineral sands containing ilmenite (FeTiO_3) or rutile (TiO_2). Ti could be extracted commercially by reducing titanium tetrachloride (TiCl_4) by combining it with the reducing agent magnesium; this process is called the *Kroll process* as explained with other processes in Ref. [1].



Ti has a density of 4.50 g/cm^3 and has about half the specific weight of steel or nickel. Due to a relatively high strength and excellent corrosion resistance of Ti and its alloys as compared to other structural metallic materials based on Fe, Ni and Al as seen in Table 2.1.

Table 2.1: Some important characteristics of Ti and Ti-based alloys as compared to other structural metallic materials based on Fe, Ni and Al [2].

	Ti	Fe	Ni	Al
Melting Temperature ($^\circ\text{C}$)	1670	1538	1455	660
Allotropic Transformation ($^\circ\text{C}$)	882 ($\beta \rightarrow \alpha$)	912 ($\gamma \rightarrow \alpha$)	-	-
Crystal Structure	bcc \rightarrow hcp	fcc \rightarrow bcc	fcc	fcc
Room Temperature E (GPa)	115	215	200	72
Density (g/cm^3)	4.50	7.90	8.90	2.70
Comparative Corrosion Resistance	Very High	Low	Medium	High
Comparative Reactivity with Oxygen	Very High	Low	Low	High
Comparative Price of Metal	Very High	Low	High	Medium

In addition, to compare Ti-alloys to other alloys, it is not just strength that is important, but both strength and density (specific strength). Therefore, a preferable way to select materials during design is to plot two material properties on a graph which will show the property-space occupied by each family or class of materials and the sub-fields occupied by individual materials. The kind of graph produced is called a materials selection chart (*Ashby Chart*) as shown in Fig. 2.1 [3]. It is shown that the maximum strength of Ti-alloys is as same as the maximum strength of steel and Ni-alloys but having a lower density. On the other hand, although the density of Al-alloys is lower than that in Ti-alloys, Al-alloys are not able to be used under relatively higher stresses as well as at relatively higher temperature as compared to Ti-alloys.

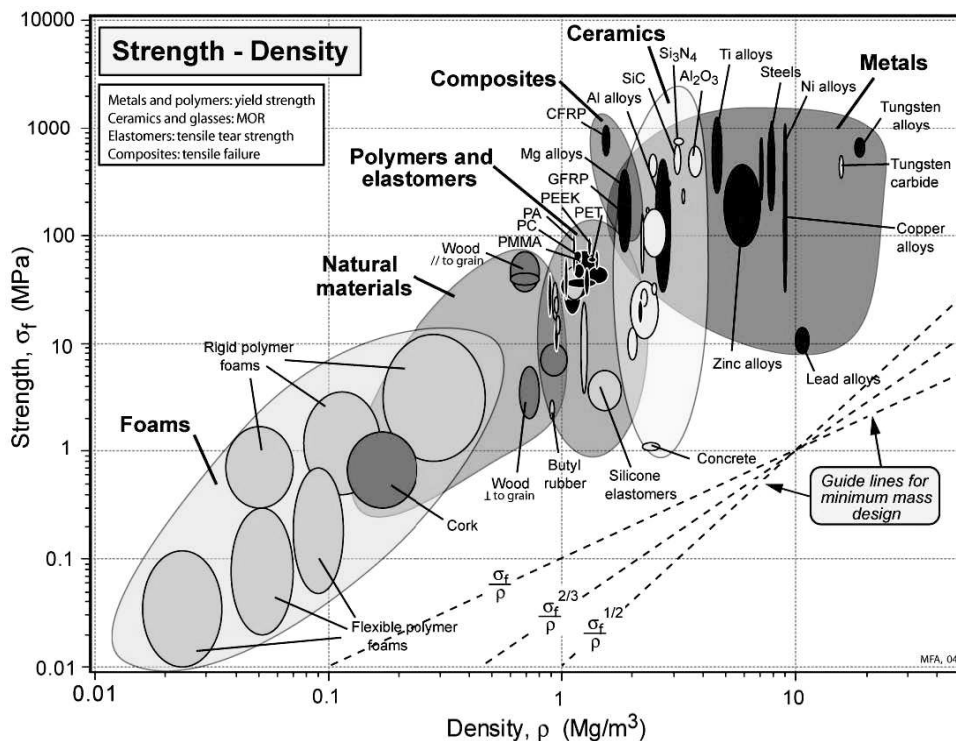


Figure 2.1: Strength-density materials selection chart (*Ashby Chart*) [3].

Pure Ti, as well as many Ti-alloys, exhibits an allotropic phase transformation at 882 °C, changing from a body-centered cubic crystal structure (bcc) as β -phase (see Fig. 2.2a) above 882 °C to a hexagonal closed-packed crystal structure (hcp) as α -phase (see Fig. 2.2b) below it. The value of the lattice parameter of the β -phase unit cell at 900 °C is $a = 0.332$ nm (Fig. 2.2a), while the lattice parameters of the α -phase unit cell at room temperature are $a = 0.295$ nm and $c = 0.468$ nm (Fig. 2.2b). The c/a ratio for pure α -Ti is 1.587, smaller than the ideal ratio of 1.633 for the hexagonal closed-packed crystal structure. This results in the three most densely packed types of the lattice planes, basal planes $\{00.1\}$, prismatic planes $\{10.0\}$ and pyramidal planes $\{10.1\}$ with the directions $\langle 11.0 \rangle$. In contrast, the most densely packed

planes in the unit cell of β -phase are $\{110\}$ with the directions $\langle 111 \rangle$. Furthermore, it should pay attention to the transformation from β -phase to α -phase upon cooling. The orientations of the slip planes and slip directions are given by the following Burgers relationship [4]:

$$\{00.1\}_{\alpha} // \{110\}_{\beta}$$

$$\langle 11.0 \rangle_{\alpha} // \langle 111 \rangle_{\beta}$$

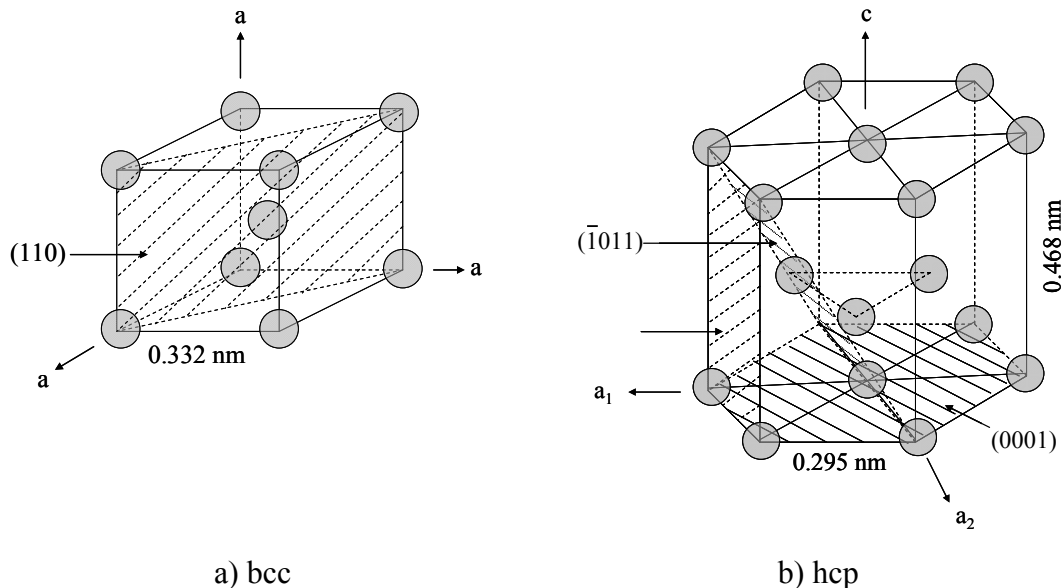


Figure 2.2: Crystal structure of β -Ti (a) and α -Ti (b) [4].

2.2.1 Classification of Titanium alloys

Alloying of Ti is controlled by the ability of elements to stabilize either α - or β -phase as illustrated in Fig. 2.3. Elements such as Al and O those dissolve in the α -phase raise the α/β transus. In this system, it is noted that aging of these alloys with an Al content above 5-6% can lead to the formation of a finely dispersed hexagonal phase (α_2) having a general formula Ti_3X . β -stabilizing elements are subdivided into β -isomorphous and β -eutectoid elements.

β -isomorphous elements, such as Mo and V, exhibit complete mutual solubility with β -Ti and progressively depress the transformation showing the martensite start (M_s) and martensite finish (M_f). On the other hand, β -eutectoid elements, such as Cu, Fe and Mn, have restricted solubility in β -Ti and form intermetallic compounds by eutectoid decomposition of the β -phase, e.g., formation the intermetallic compound Ti_2Cu in Ti-2.5Cu. Examples are the binary systems Ti-Fe and Ti-Mn and these alloys behave as if they conformed to the β -isomorphous phase diagram; hence the arrows shown in Fig. 2.3.

Furthermore, there are some elements, such as Zr and Sn, behave neutrally. More details are described in [5].

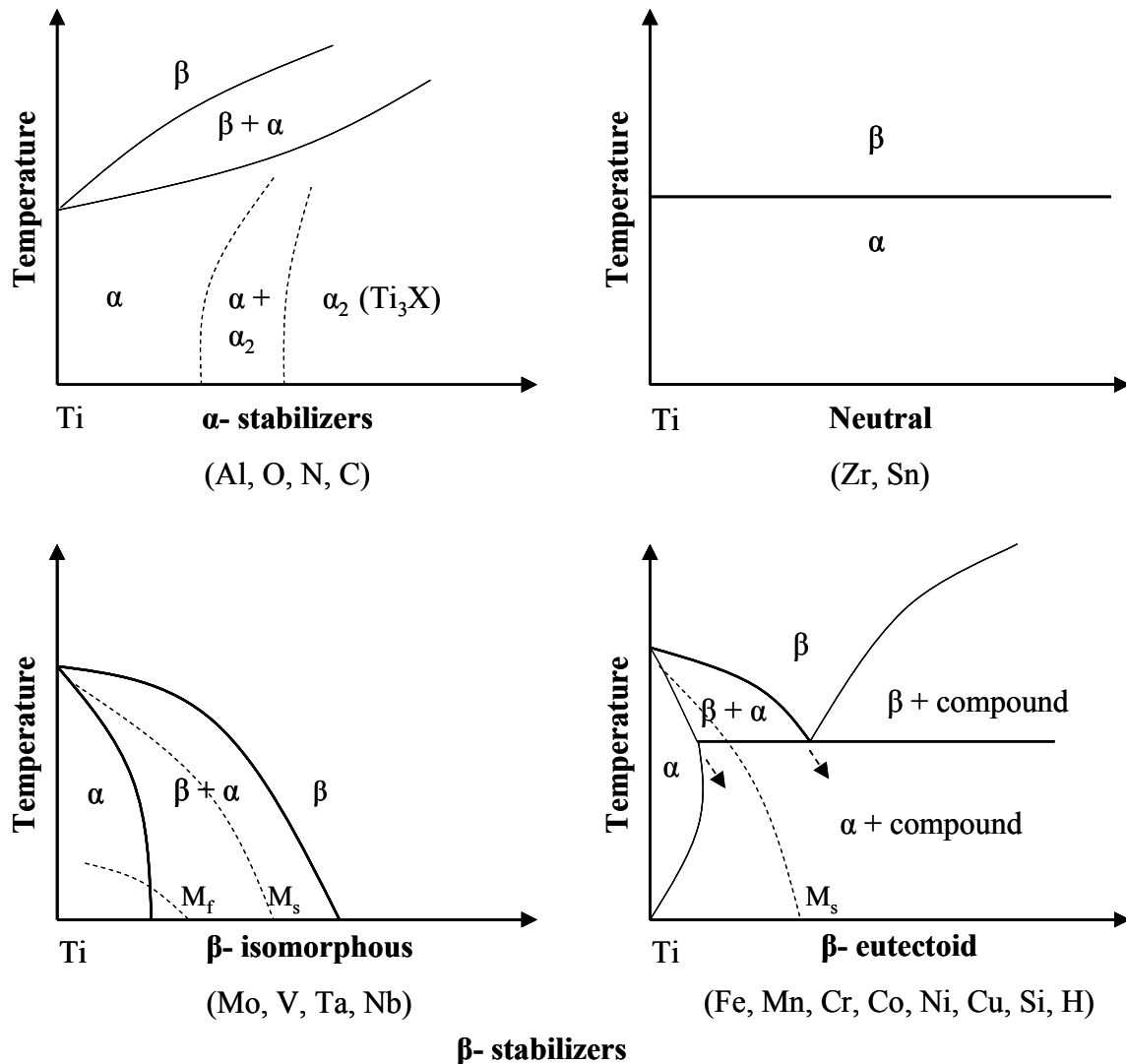


Figure 2.3: Classification scheme of Ti-alloys phase diagrams.

In the present study, three different Ti-alloys have been investigated: α Ti-alloy Ti-2.5Cu, ($\alpha + \beta$) Ti-alloy TIMETAL 54M (in the following Ti-54M) and the metastable β Ti-alloy TIMETAL LCB (in the following LCB). Ti-2.5Cu or IMI 230 (ASM) combines the formability and weldability of unalloyed Ti with improved mechanical properties, particularly at elevated temperatures. This alloy is used in the annealed condition as sheets, forgings and extrusions for fabricating component such as bypass ducts of gas turbine engines [7]. Ti-54M was newly developed by TIMET, Henderson, NV (USA) with nominal composition (wt. %) Ti-5Al-4V-0.6Mo-0.4Fe that can offer improved both machinability and formability as compared to the well-known Ti-6Al-4V [8]. This alloy is being evaluated for both aerospace and non-aerospace applications. LCB was developed targeting automotive suspension spring

applications. The nominal chemical composition (wt. %) of this alloy is Ti-1.5Al-6.8Mo-4.5Fe. The formulation cost of this alloy is lowered by adding Mo and Fe in the form of a ferro-molybdenum master alloy [9,10].

2.3 Improvement of the Fatigue Life by Mechanical Surface Treatments

Fatigue is defined as the changes in properties which can occur in metallic or non-metallic materials due to repeated application of stresses and strains which lead to cracking or failure. Fatigue life is affected by some factors such as cyclic stress state, sample geometry, surface quality, environment, temperature and residual stress. In present study, the mechanical surface treatments such as shot peening (SP), laser shock peening without coating (LPwC), ultrasonic shot peening (USP) or ball-burnishing (BB) were used. The beneficial influence of the mechanical surface treatments on the fatigue performance is often explained by surface strengthening by the process-induced high dislocation densities hindering crack nucleation at the surface and residual compressive stresses which retard microcrack growth from the surface [11]. Generally, the total fatigue life (N_F) of a component can be divided into a crack-free initial stage, i.e. the number of cycles to fatigue crack nucleation (N_I) and the number of cycles for propagating fatigue cracks (N_P) until final fracture: $N_F = N_I + N_P$. Table 2.2 summarizes the individual effects of the surface layer properties on fatigue life [12].

Table 2.2: Effects of surface layer properties on the various stages on fatigue life [12].

Surface layer property	Fatigue crack nucleation	Fatigue microcrack Propagation
Surface roughness	Accelerates	No effect
Cold work	Retards	Accelerates
Residual compressive stresses	Minor effect	Retards

2.3.1 Conventional Shot Peening Process

Shot peening (SP) is a process used to produce a compressive residual stress layer and modify mechanical properties of metals. The changes in the surface state due to SP are, for examples, changes of the residual stresses, microstructures, hardness by work hardening, surface roughness, cracks, crystallographic texture [13-15] and dislocation density as shown schematically in Fig. 2.4.

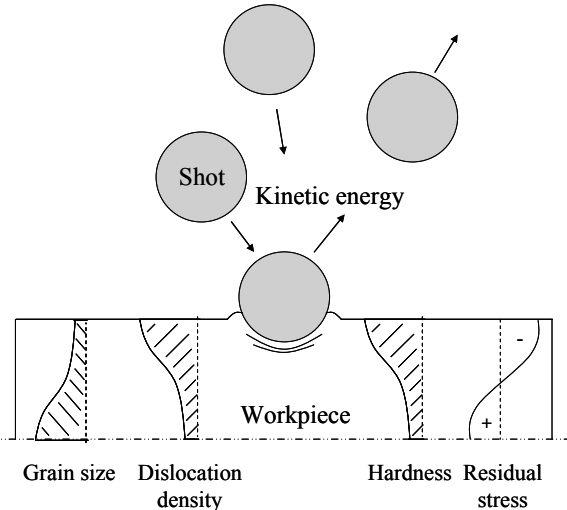


Figure 2.4: Principle of shot peening process.

It entails impacting a surface with shot (round metallic, glass or ceramic particles) with a kinetic energy sufficient to create plastic deformation, each piece of shot that strikes the material acts as a tiny peening hammer, imparting to the surface a small indentation or dimple. To create the dimple, the surface of the material must yield in tension. Below the surface, the material tries to restore its original shape, thereby producing below the dimple a hemisphere of cold-worked material highly stressed in compression.

There are many process parameters influencing on the surface characteristics after SP as listed in Table 2.3. Due to a large number of these parameters influencing on the results (Table 2.3), J. O. Almen (1940) developed a standard process to measure the kinetic energy transferred by a shot stream using Almen strip system as shown in Fig. 2.5 [16].

Table 2.3: Parameters influencing on the results of shot peening treatment.

Device	Shot	Workpiece
Shot velocity	Shape	Geometry
Impact angle	Hardness	Elastic-plastic-deformation behavior
Mass flow rate	Mass	Hardness
Peening time	Size	Crystal structure
Coverage	Material	Temperature
Nozzle diameter	Wear state	Pre-stress
Nozzle clearance		

As seen in Fig. 2.5, an Almen strip is a thin strip of SAE 1070 steel used to quantify the intensity of a shot peening process. They are classified into 3 types: 'N' (0.79 mm thick), 'A' (1.30 mm thick), and 'C' (2.38 mm thick). They differ in their thickness, while they have the

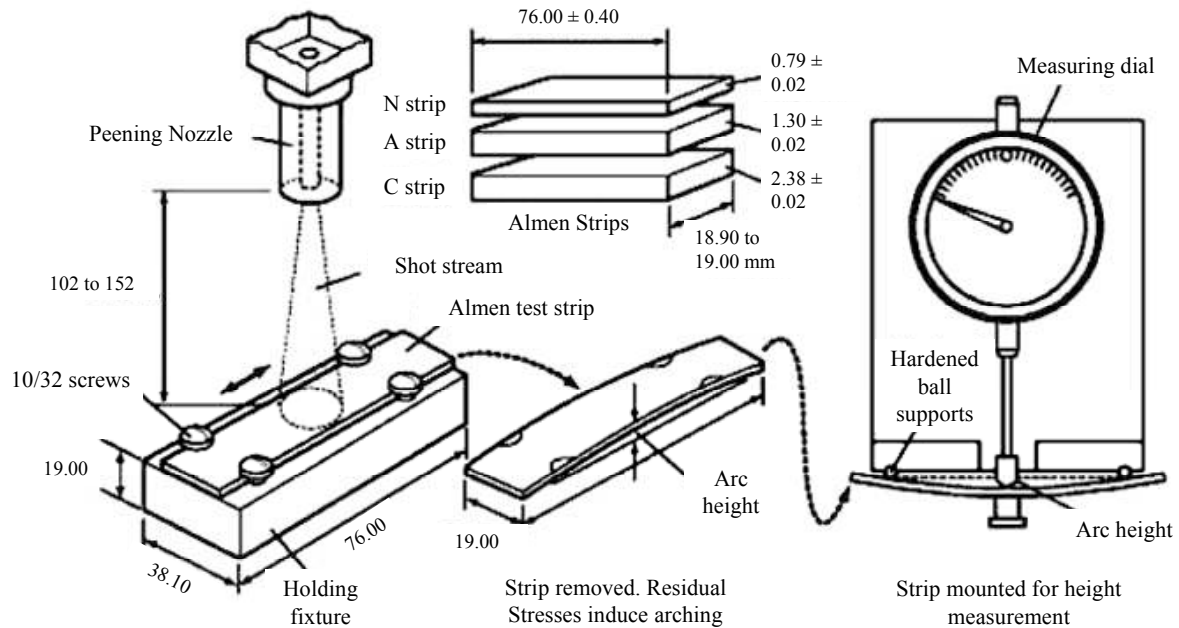


Figure 2.5: Almen strip system (All dimensions in mm) [16].

same length and width (76 mm long x 19 mm wide). SP specifications refer to this energy as intensity at saturation, which means the earliest point of the saturation curve that, if the exposure time is doubled, the arc height increased by 10% or less (Fig. 2.6 [17]). Complete coverage of a shot peened surface is crucial in performing high quality SP. Coverage is the ratio of the area covered by hits and the complete surface treated by SP.

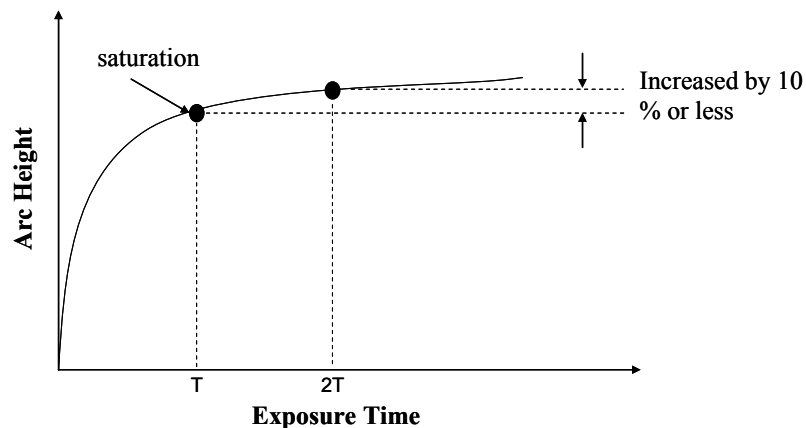


Figure 2.6: Arc height vs. exposure time scheme [17].

2.3.2 Ultrasonic Shot Peening

Recently, ultrasonic shot peening (USP) has been studied to improve the durability of structural parts [18]. In USP, unlike SP where the shot is propelled by compressed air, the shot is energized by a sonotrode vibrating at ultrasonic frequency. One of the USP devices

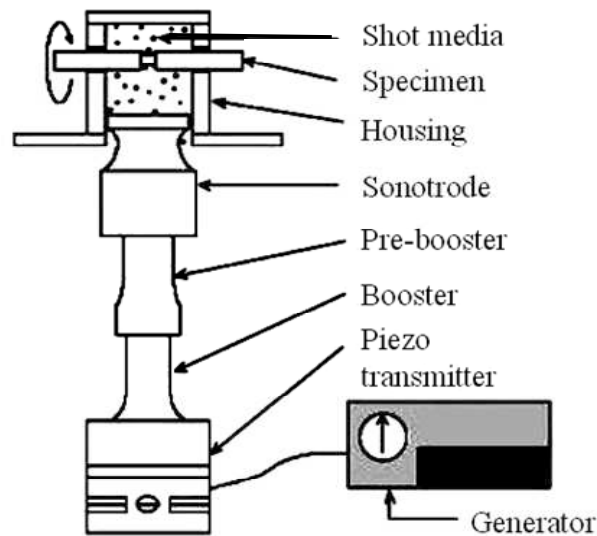


Figure 2.7: Illustration of Stresssonic[®] Treatment [19].

developed by SONTAS in France [19], called Stresssonic[®], is illustrated in Fig. 2.7. In this process, the shot is set into a random whirling motion inside a component-specific peening chamber to act on the component. The result of the peening action essentially depends on the arrangement of the sonotrode relative to the component. The main characteristic of such process could give a smooth surface compared to SP due to using polished bearing ball with a large diameter. Furthermore, it can give much energy in short time due to a high frequency [20].

2.3.3 Burnishing Process

Burnishing (Fig. 2.8) is the most sufficient mechanical process to improve the fatigue strength of dynamically loaded components. This can be performed using either rolls (called roll-burnishing) or balls (called ball-burnishing). The principle of the ball-burnishing (BB) process (or deep rolling) is based on the rolling movement of a ball with a normal force against the surface of the workpiece tool [21]. The hydrostatically loaded ball can freely rotate in any direction within the ball retainer, even at high speed. In addition, it can be applied with CNC-controlled lathes, drills, milling and manually controlled machines. As soon as the yield point of the material is exceeded, plastic flow of the original asperities takes place. This process leads to a smoother surface [22] and greater amount of compressive residual stress than SP process [23]. Moreover, compressive residual stress is induced in the surface layer, followed by strain hardening and a series of beneficial effect on mechanical properties leading to improve fatigue [24] and corrosion [25] resistance of different metals under dynamic loads.

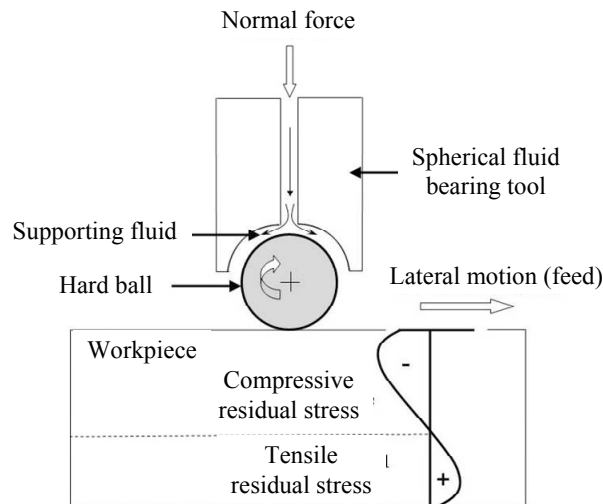


Figure 2.8: Principle of ball-burnishing process.

2.3.4 Laser Shock Peening

Laser shock peening (LSP) is an innovative surface treatment technique, which has been successfully applied to improve fatigue performance of metallic components. The key beneficial characteristic after LSP treatment is the presence of compressive residual stresses beneath the treated surface of by high magnitude shock waves. The principle of this process is schematically illustrated in Fig. 2.9.

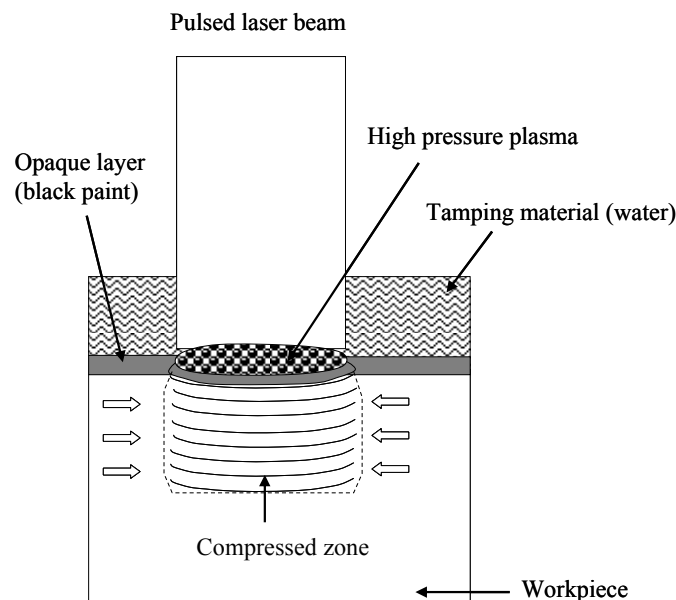


Figure 2.9: Principle of Laser shock peening process.

Prior to LSP, the material surface is plated with an opaque layer of black paint, metal foil or tape. The black layer is then covered with a transparent overlay (commonly flowing water).

The material of the black layer has low heat of vaporization. When the laser strikes the sample surface the pulses energy is absorbed by the opaque material, which heats up, vaporizes and forms high temperature plasma. The plasma gas is trapped between the sample surface and the transparent water layer limiting the thermal expansion of plasma gas. As a result the gas pressure increases to extremely high value. The high pressure is transmitted to the workpiece material producing a shock wave, which travels through the part material and generates compression stress. Effect of LSP is cold work (not heating nor melting). The purpose of water is to confine the high pressure plasma gas (not cooling the workpiece surface) [26].

LSP can produce greater amount and penetration depth of compressive residual stresses compared to SP [27] and used mainly for increasing fatigue strength [28]. The compressive residual stresses are produced with less work hardening than that with SP, allowing for less thermal relaxation of these stresses when subjected to high temperatures [29]. The influences of BB and LSP on the fatigue behavior of Ti-6Al-4V and austenitic steel AISI 304 were investigated by R.K. Nalla et al. [29] and I. Nikitin et al. [30], respectively. It was found that BB produced greater amount of the compressive residual stress and higher degree of the work hardening compared to LSP. Turski et al. [31] compared the efficacy of USP, LSP and water jet cavitation peening (WJCP) at introducing residual stresses and modifying the near-surface state compared to SP benchmark for AISI 304. It was concluded that WJCP and LSP introduced the lowest levels of surface roughening. Furthermore, the level of plastic work introduced by LSP and USP is considerably less than that by SP, although the depth of work hardening extends to greater depths. Crack initiation and early crack growth in Ti-6Al-4V aerofoil samples due to foreign object damage (FOD) and subsequent fatigue growth were examined after applying LSP [32]. It was found that LSP has improved the crack growth resistance post FOD. Delayed onset of crack initiation was observed in LSP samples compared to those without LSP under similar loading conditions.

Thermal stability of near-surface microstructures induced by BB and LSP in AISI 304 and Ti-6Al-4V using in situ transmission electron microscopy (TEM) was investigated by Altenberger et al. [33]. Results revealed that the near-surface nanocrystalline grain structure remained thermally stable up to 600–650 °C in AISI 304 after BB, while in AISI 304 after LSP, where a highly tangled and dense dislocation substructure formed rather than a nanocrystalline grain structure, the near-surface dislocation tangles were stable up to 800 °C approximately. Ti-6Al-4V also formed a nanocrystalline near-surface structure with high dislocation density after BB, which was stable up to 650 °C. Fretting fatigue experiments

were conducted using LSP treated Ti-6Al-4V [34]. It was found that LSP prolonged the fatigue life by a magnitude depending on the stress level. Fatigue crack initiation and propagation of 7050-T7451 aluminium alloy was investigated after performing LSP by X.D. Ren et al. [35]. It was concluded that greater depth of the residual compressive stress induced by LSP resulted in a slower fatigue crack growth rates, and the crack propagation life was considerably longer than that of the non-LSP case. It should be pointed out that the optimization design of LSP procedure for metal samples with complex shape is necessary to obtain better surface treatment [36].

The major disadvantage of LSP is that it currently requires an elaborated laser system specially designed for production runs with high average power and large pulse energy up to, for example, 100 J. On the other hand, laser shock peening without coating (LPwC) utilizes a commercially-available compact laser system with much smaller power and pulse energy of about 0.1 J to reduce thermal effects on the surface [37]. The process, effect and application of LPwC were studied [38]. It was concluded that LPwC prevents stress corrosion cracking (SCC) and prolongs fatigue life. Surface layer properties such as residual stress and work hardening in Ti-2.5Cu after LPwC was investigated and compared with those after SP, USP and BB [39]. Results revealed that LPwC produced the lowest work hardening in the surface layer, while BB produced the highest maximum compressive residual stress.

In the present work, the effectiveness of LPwC for improving the HCF performance in Ti-2.5Cu, Ti-54M and LCB Ti-alloys was examined and discussed.

2.3.5 Surface Mechanical Attrition Treatment

Recently, a new family of surface severe plastic deformation processes (SPD) using high-energy balls, widely known as the surface mechanical attrition treatment (SMAT), has been developed to induce in the workpiece routinely the desired nanocrystalline surface layer [40]. Figure 2.10 illustrates the experimental setup of the SMAT [41]. Spherical steel balls with smooth surface (or of other materials such as glass and ceramics) are placed in a reflecting chamber that is vibrated by a vibration generator. Typical ball sizes are 1–10 mm in diameter and that can be different for different materials. The vibration frequency of the chamber is in the range from 20 Hz to 50 kHz. When the balls are resonated, the sample surface to be treated is impacted by a large number of flying balls over a short period of time. The velocity

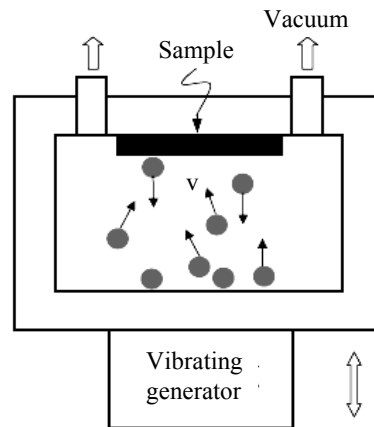


Figure 2.10: Schematic illustration of the surface mechanical attrition (SMAT) treatment setup [41].

of the balls is about 1-20 m/s, depending upon the vibration frequency, the distance between the sample surface to the balls, and the ball size. The impact directions of the balls onto the sample surface are rather random due to the random flying directions of the balls inside the vibration chamber. Each impact induces plastic deformation with a high strain rate in the surface layer of the sample. SMAT produces a thicker nanocrystalline surface layer, a deeper plastically deformed region with greater abundance of twins, faults and dislocations, and a thicker surface region with greater residual compressive stresses than SP [42,43]. These differences make SMAT more effective in improving the fatigue properties than SP.

2.4 The Influence of Mean Stress Sensitivity, Environment and Residual Stress on Titanium alloys

Many studies have been carried out to investigate of the response of various Ti-alloys to mechanical surface treatments. The following survey is divided into 3 sections involving the influence of mean stress sensitivity or stress ratio, environmental sensitivity and residual stress level on the high cycle fatigue (HCF) performance of mechanically surface treated Ti-alloys.

2.4.1 Mean Stress Sensitivity

The stress ratio or mean stress dependence of the 10^7 cycle fatigue strength of a material is usually evaluated from a so-called Smith diagram, where the maximum allowable stress is plotted versus the mean stress. If only the fully reversed HCF strength ($R = -1$) and the tensile

strength (UTS) are known, the allowable stress amplitude for a given tensile mean stress can be roughly estimated by the Eq. 2.1 as follows [44]:

$$\sigma_{10^7(\sigma_m > 0)} = \sigma_{a(\sigma_m = 0)} \left[1 - \frac{\sigma_m}{UTS} \right] \text{-----} (2.1)$$

Mean stress sensitivity could be either normal or anomalous depending upon fatigue crack mechanism, crystallographic texture or loading direction as explained elsewhere [45]. Normal and anomalous mean stress sensitivities (AMSS) are schematically illustrated in Fig. 2.11a and Fig. 2.11b, respectively, as predicted by the Goodman relationship [46]. It has been studied the effect of the stress ratio ($R = -1$ and $R = 0.1$) on HCF of α , ($\alpha + \beta$) and β Ti-alloys [9,44,47]. It was observed that α (e.g., Ti-2.5Cu) and β Ti-alloys (e.g., TIMETAL LCB) show normal mean stress sensitivity, while ($\alpha + \beta$) Ti-alloys could show AMSS.

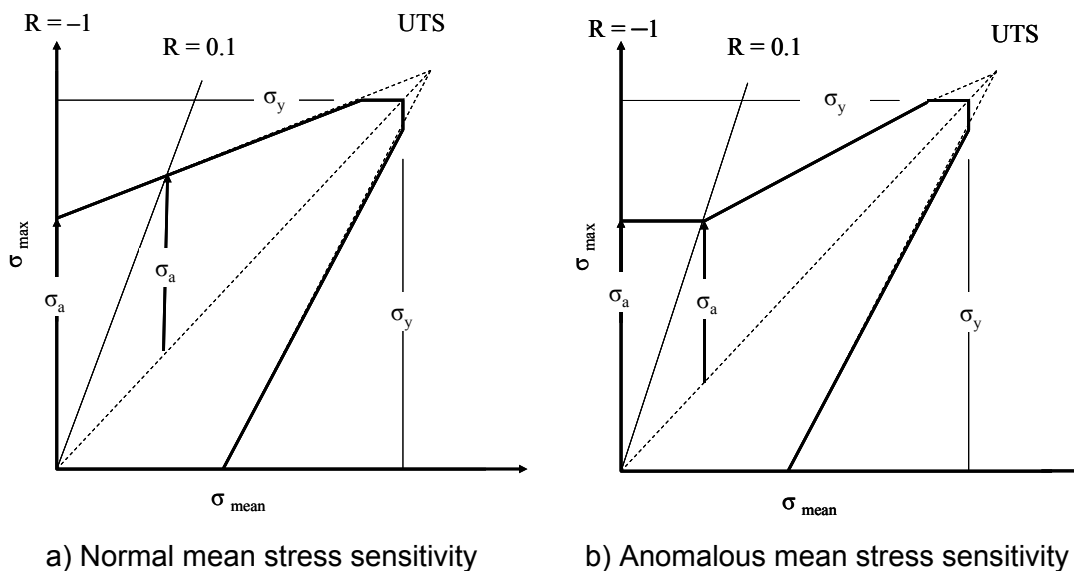


Figure 2.11: Schematic Smith diagram showing normal mean stress sensitivity (a) and anomalous mean stress sensitivity (b) [47].

It was argued that AMSS was caused by crack nucleation at α -grain or α -phase boundaries in tension-tension loading at comparatively low maximum applied tensile stress [48]. Furthermore, fully lamellar microstructure of ($\alpha + \beta$) Ti-alloys such as Ti-6Al-7Nb and Ti-6Al-4V shows normal mean stress dependence of the fatigue strength, while fully equiaxed or duplex microstructure shows AMSS. AMSS could be explained by the presence of micro-texture zones in the materials which stem from the ($\alpha + \beta$) processing [49].

In the aforementioned literatures, it was concluded that the different responses of the fatigue strength of Ti-alloys after SP or BB are attributed to both mean stress and environmental sensitivities. For example, the alloy Ti-2.5Cu shows normal mean stress sensitivity and,

therefore, a marked fatigue strength improvement by SP or BB. On the contrary, the equiaxed microstructure (EQ) in Ti-6Al-4V responds with a dramatic loss in HCF strength due to SP. This is explained by AMSS. Comparing results on EQ Ti-54M and EQ Ti-6Al-4V it is thought that the α -grain size is the main parameter in affecting mean stress sensitivity and thus the HCF response to SP and BB [48]. A loss was also found in LCB, although it shows normal mean stress sensitivity. This is described by environmental sensitivity as explained in the next section.

2.4.2 Environmental Sensitivity

The interaction of mechanical surface treatments and fatigue environment (air, vacuum or 3.5% aqueous NaCl) on the fatigue performance of α , ($\alpha + \beta$) or β Ti-alloys has been studied [9,47,50,51]. It was found that α (e.g., Ti-2.5Cu) and ($\alpha + \beta$) (e.g., Ti-6Al-4V and Ti-54M [48]) Ti-alloys exhibit HCF strengths in vacuum markedly higher than in air depending on microstructures. This effect is presumably described by detrimental hydrogen effects on the α -phase during fatigue testing in air [52]. Furthermore, the improvement of fatigue life in vacuum was discussed in association with enhancement of plastic deformability due to internal heating as well as the kinetics of molecular adsorption at the tip of growing crack [53]. On the contrary, no loss in HCF strength by a change in environment from vacuum to air was observed on β Ti-alloys (e.g., β -annealed LCB). This result indicated that the β -phase is hardly sensitive to hydrogen embrittlement. There is a direct effect of the dissolved hydrogen in the β -lattice structure [52]. The three most important concepts which are often referred to are (i) hydrogen-enhanced local plasticity [54,55], (ii) decohesion [56] and (iii) stress-induced hydride formation [57].

2.4.3 Residual Stress

Stresses in a part being present in the absence of any external loads are called residual stresses. Macroscopic residual stresses can be either detrimental or beneficial to the performance of materials [58]. Compressive residual stress is well known to enhance the fatigue performance and corrosion resistance by retarding or even suppressing microcrack growth from the surface into the interior. Residual stress distribution can be affected by different parameters of mechanical surface treatments. For example, changes in SP parameters, such as shot hardness (H_s), material hardness (H_m), shot velocity (V) and

coverage (C), influence on the compressive residual stress distribution as shown in Fig. 2.12 [59].

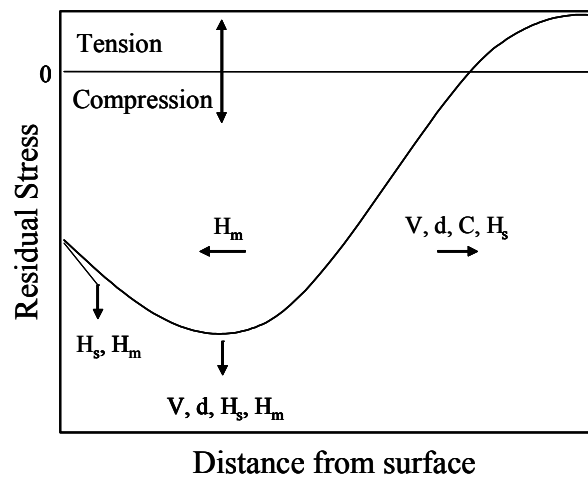


Figure 2.12: Shot peening parameters vs. residual stress distribution [59]

(V = shot velocity, d = shot size, C = coverage, H_s = shot hardness, H_m = material hardness).

Many researches have been carried out to study the influence of the mentioned SP parameters on the residual stress distributions. The influence of the mean shot velocity and the velocity distribution on the residual stress depth distribution was investigated on 42CrMo4 [60]. It was found that the thickness of the layer with compressive residual stress is increased by increasing shot velocity, whereas the amount of maximum residual stress below the surface does not depend on the mean shot velocity.

The effect of SP coverage on residual stress in Ni-Cr-Mo low alloy steel was studied [61]. It was concluded that complete coverage is not required to produce full benefits of SP. The magnitude of this compressive stress is a function of the mechanical properties of the target material and may reach values as high as 50 to 60 % of the material's ultimate tensile strength [62–64]. Its depth largely depends upon the peening intensity and the relative hardness of the shot and target material. For a relatively soft target material (230-300 HV), it is feasible to produce a compressive layer of 800 to 1000 μm deep, whilst for a harder material (700 HV), it can be difficult to produce a compressive layer of much more than 200 to 250 μm [65]. Compressive residual stresses can be produced deliberately by mechanical surface treatments to improve the HCF of various engineering materials [66–68]. Some studies have been carried out to investigate the influence of different compressive stress profiles on the fatigue performance of Ti-2.5Cu. It was found that BB produced relatively deeper and higher compressive residual stress compared to SP. This resulted in enhancement of 10^7 cycles fatigue strength in solid solution heat treated (SHT) Ti-2.5Cu by 45% after SP [47, 69,70] and

60 % after BB as well as by 24% after SP and 47 % after BB in double-aged Ti-2.5Cu [70] in rotating beam loading ($R = -1$). Such improvements have revealed that the failure is associated with subsurface fatigue crack nucleation. This phenomenon may be related to the presence of a process-induced tensile residual stress necessarily present below the mechanically treated surface and required to balance compressive residual stress induced by the surface treatment process. This balancing tensile residual stresses could be either of the following two forms: firstly in a constant form (full line in Fig. 2.13) as described in the core region of a thin shot peened AISI 4140 steel plates [71]; secondly in a concentrated form (dashed line in Fig. 2.13) as found in a relatively thin layer after SP, LSP or USP in 304 austenitic stainless steel [72]. Neutron diffraction is efficient in identification of the residual stresses in a variety of engineering materials which have experienced different SP treatments [73]. It was concluded that these stresses show surface compression balanced by subsurface tension of about one third of the surface compressive stress value. Furthermore, due to the finite volume of material needed for neutron measurements, it is difficult to produce precise measurements within the first 100 μm from the surface. Therefore, it is essential to introduce some methods used to determine residual stresses as mentioned in the following section.

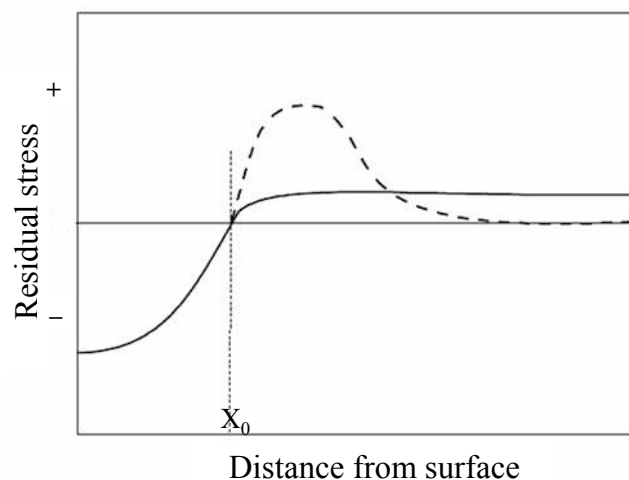


Figure 2.13: Schematic presentation of the residual-stress distribution which might be expected after mechanical treatments, x_0 denotes the zero-crossing depth [71].

2.5 Residual Stress Determination by Diffraction Methods

There are many methods to determine residual stresses including mechanical, magnetic, electrical, ultrasonic, thermoelastic, thermoplastic and diffraction methods as explained in Ref. [58]. In the present study, angle-dispersive X-ray, energy-dispersive and neutron diffraction were mainly used to determine macroscopic or first order residual stress (σ^1)

beside the incremental hole drilling technique as a mechanical method. σ^1 is constant over several grains and are in equilibrium within the whole body such as residual stresses induced by mechanical surface treatments. On the other hand, second order residual stress (σ^2) are constant within one crystallite and are compensated over a few crystallites such as residual stresses induced due to differences in thermal expansion between the single crystallites of a polycrystalline material. Third order residual stresses (σ^3) vary on an atomic scale and are compensated within one crystallite due to substitution or dislocations in the crystallites [74]. Second and third order residual stresses are called microscopic residual stresses. This is schematically shown in Fig. 2.14 [75].

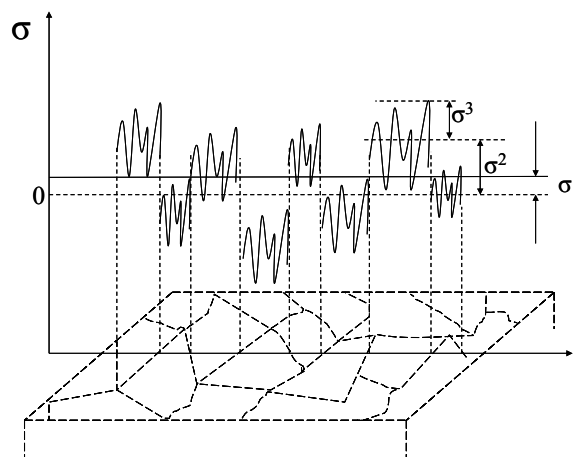


Figure 2.14: Schematic representation of residual stresses of types 1, 2 and 3 [75].

Diffraction methods of residual stress determination basically measure diffraction angle (θ) at which a maximum diffracted intensity takes place when a crystalline sample is subjected to X-rays or neutrons. From this angle, interplanar spacing (d) of the diffraction planes can be obtained using Bragg's law ($\lambda = 2d \cdot \sin\theta$), where λ is a beam wavelength. If residual stresses exist within the sample, then the d spacing will be different than that of an unstressed state. This difference is proportional to magnitude of the residual stress [76,77].

2.5.1 X-Ray Diffraction

In the present study, the laboratory or angle-dispersive X-ray diffraction (Lab-XRD) as well as the energy-dispersive X-ray diffraction using synchrotron radiation (ED-XRD) were used due to the advantages offered by each method. Synchrotrons or hard X-rays provide very intense beams of high energy X-rays. This leads to a relatively higher penetration depth in engineering components. Higher penetration depth is considered as one of the major

advantages of ED-XRD over Lab-XRD [78,79]. The measurement is also much faster than Lab-XRD. In contrast, due to a small penetration depth of Lab-XRD, the influence of stress gradients is in general less important. In addition, it is able to determine residual stresses at the surface or within a few micrometers in depth from the mechanically surface treated surface [80].

In ED-XRD using a white beam, the diffraction angle θ and the scattering angle 2θ can be chosen freely and remain fixed during the measurement (Fig. 2.15b). The correlation between the lattice spacing $d_{(hkl)}$ and the corresponding diffraction line $E_{(hkl)}$ on the energy scale follows immediately by inserting the energy relation $E_{(hkl)} = h \cdot c / \lambda$, where h is Planck's constant, and c is the speed of light. ED-XRD is given by the multitude of reflections (hkl) recorded simultaneously in one spectrum, which provide additional information, since they comprise different penetration depths $\tau_{(hkl)}$ [81]. On the other hand, in the case of Lab-XRD using a monochromatic beam, the wavelength (λ) is constant depending on target materials in X-ray tubes (e.g. $\lambda = 1.5418 \text{ \AA}$ for Cu-tube and $\lambda = 1.7902 \text{ \AA}$ for Co-tube) and the diffraction angle θ can be varied (Fig. 2.15a) [82].

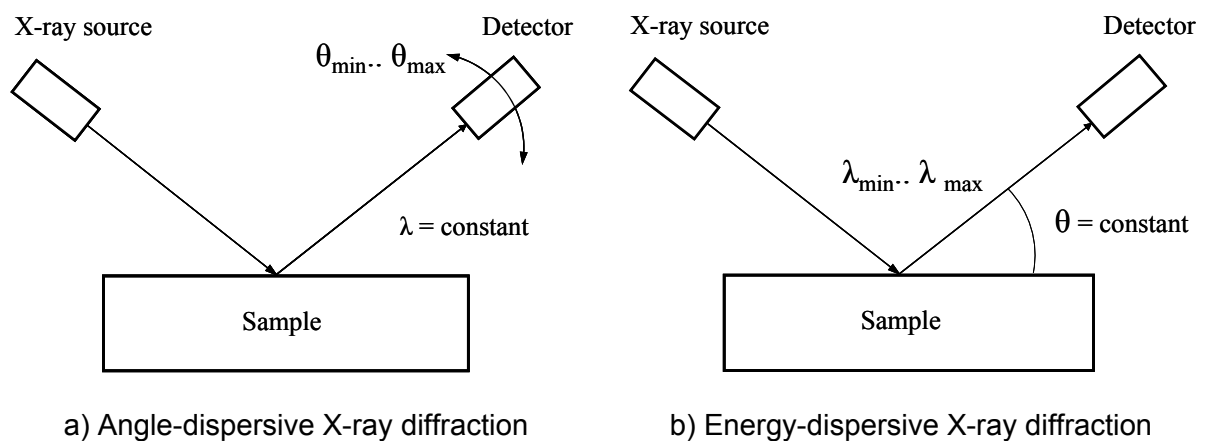


Figure 2.15: Comparison of angle-dispersive (a) and energy-dispersive X-ray diffraction (b) [82].

In both methods, residual stresses can be analyzed by using $\sin^2\psi$ method. This method is a sensitive and accurate technique to measure residual stresses in a fine grained, polycrystalline material. As shown in Fig. 2.16, the position of a diffraction peak will shift as the sample is tilted by an angle ψ . The magnitude of the shift will be related to the magnitude of the residual stress. Thus, if there is no residual stress, the shift will be zero. Since the X-ray penetration is extremely shallow using Lab-XRD, a condition of plane-stress is assumed to exist in the diffracting surface layer. The stress distribution is then described by principal stresses (σ_{11} and σ_{22}) in the plane of the surface, with no stress acting perpendicular to the free

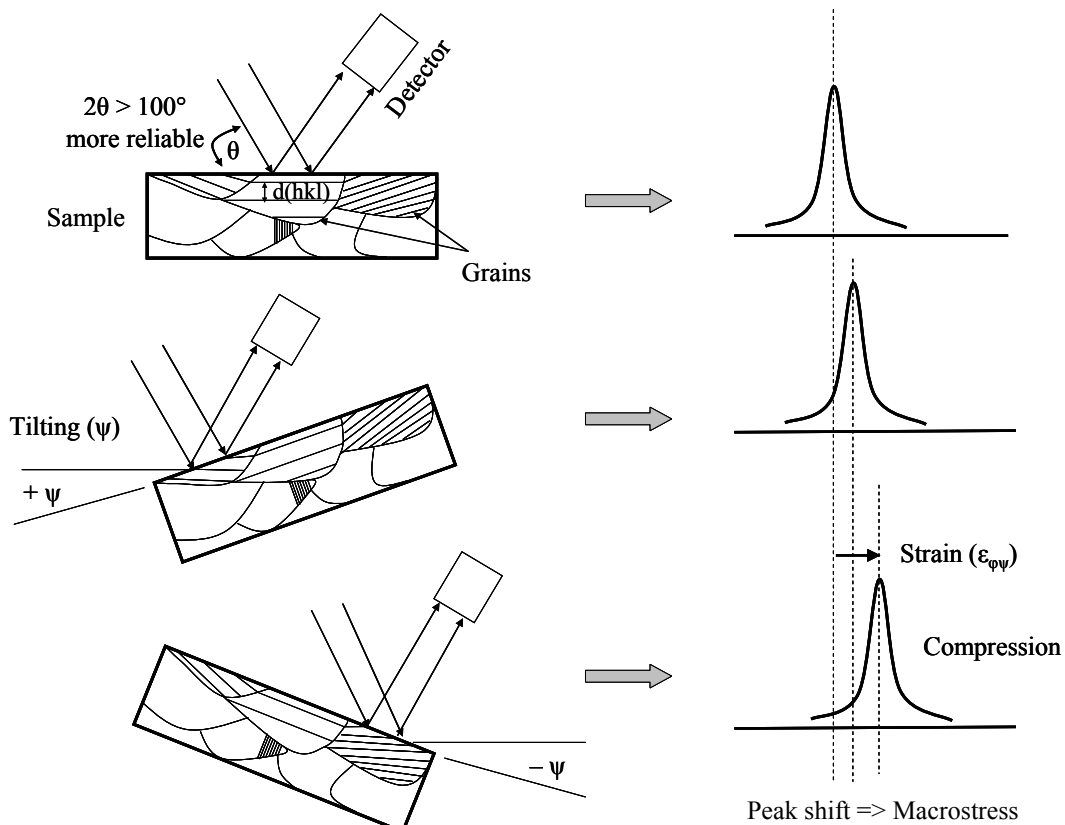


Figure 2.16: Scheme showing shift of diffraction peak with change in tilting angle ψ ($d_{(hkl)}$ = lattice spacing of hkl plane).

surface [83–86] as shown in Fig. 2.17

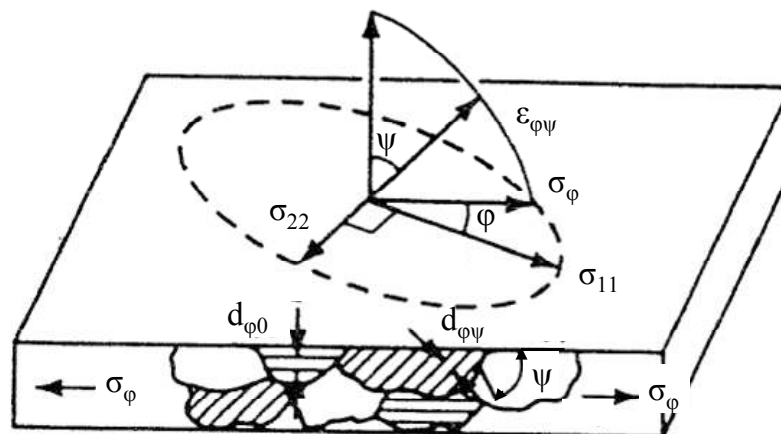


Figure 2.17: Plane stress at a free surface showing the change in lattice spacing with tilt ψ for a uniaxial stress σ_ϕ parallel to one edge [83].

In case of shot peened materials generally the normal component σ_{33} and the shear stresses $\sigma_{13} = \sigma_{31}$ and $\sigma_{23} = \sigma_{32}$ acting out of the plane of the sample surface are negligible. A strain component perpendicular to the surface, ϵ_{33} , exists as a result of the Poisson's ratio

contractions caused by the two principal stresses. The strain in the sample surface at an angle ϕ from the principal stress σ_{11} is then given by:

$$\epsilon_{\phi\psi} = \left(\frac{1+\nu}{E} \right) \sigma_{\phi} \sin^2 \psi - \left(\frac{\nu}{E} \right) (\sigma_{11} + \sigma_{22}) \quad (2.2)$$

where E is Young's modulus and ν is Poisson's ratio. Equation 2.2 relates the surface stress σ_{ϕ} , in any direction defined by the angle ϕ , to the strain, $\epsilon_{\phi\psi}$, in the direction (ϕ, ψ) and the principal stresses in the surface. As seen in Fig. 2.17, if $d_{\phi\psi}$ is the spacing between the lattice planes measured in the direction defined by ϕ and ψ , the strain can be expressed in terms of changes in the spacing of the crystal lattice (see Eq. 2.3).

$$\epsilon_{\phi\psi} = \frac{\Delta d}{d_0} = \frac{d_{\phi\psi} - d_0}{d_0} \quad (2.3)$$

Where d_0 is the stress-free lattice spacing. Substituting into Eq. 2.2 and solving for $d_{\phi\psi}$ yields (Eq. 2.4):

$$d_{\phi\psi} = \left[\left(\frac{1+\nu}{E} \right)_{(hkl)} \sigma_{\phi} d_0 \right] \sin^2 \psi - \left(\frac{\nu}{E} \right)_{(hkl)} d_0 (\sigma_{11} + \sigma_{22}) + d_0 \quad (2.4)$$

where $(\nu/E)_{(hkl)}$ or S_1 and $[(1+\nu)/E]_{(hkl)}$ or $\frac{1}{2} S_2$ are diffraction elastic constants in the crystallographic direction normal to the (hkl) lattice planes in which the strain is measured. The relationship between lattice spacing ($d_{\phi\psi}$) and $\sin^2 \psi$ in the case of compression is schematically shown in Fig. 2.18.

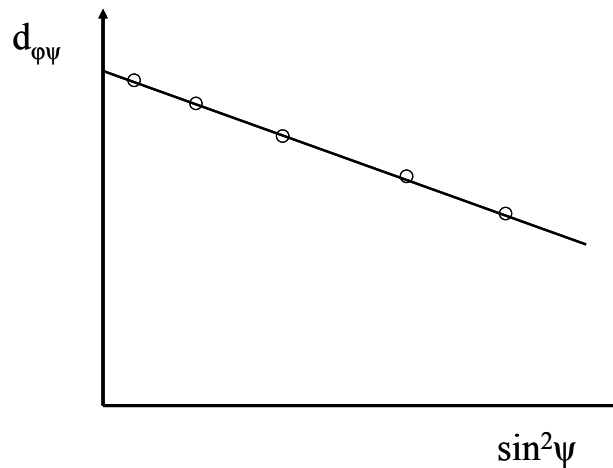


Figure 2.18: Schematic plot showing a relationship between lattice spacing ($d_{\phi\psi}$) and $\sin^2 \psi$.

The intercept of the plot ($d_{\phi 0}$) at $\sin^2\psi = 0$ equals the unstressed lattice spacing, d_0 , minus the Poisson's ratio contraction caused by the sum of the principal stresses (Eq. 2.5)

$$d_{\phi 0} = d_0 - \left(\frac{\nu}{E}\right)_{(hkl)} d_0 (\sigma_{11} + \sigma_{22}) = d_0 \left[1 - \left(\frac{\nu}{E}\right)_{(hkl)} (\sigma_{11} + \sigma_{22}) \right] \text{-----} (2.5)$$

The slope of the plot is:

$$\frac{\partial d_{\phi\psi}}{\partial \sin^2\psi} = \left(\frac{1+\nu}{E}\right)_{(hkl)} \sigma_{\phi} d_0 \text{-----} (2.6)$$

which can be solved for stress σ_{ϕ} (Eq. 2.7).

$$\sigma_{\phi} = \left(\frac{E}{1+\nu}\right)_{(hkl)} \frac{1}{d_0} \left(\frac{\partial d_{\phi\psi}}{\partial \sin^2\psi}\right) \text{-----} (2.7)$$

Since the value of the lattice spacing measured at $\psi = 0$ differs by not more than 0.1 percent from the stress-free lattice spacing, the intercept can be substituted for d_0 . The residual stress can then be calculated without reference to a stress-free standard [84].

The new European standard defines the following limitations for state of the art measurements [87] as shown in Fig. 2.19:

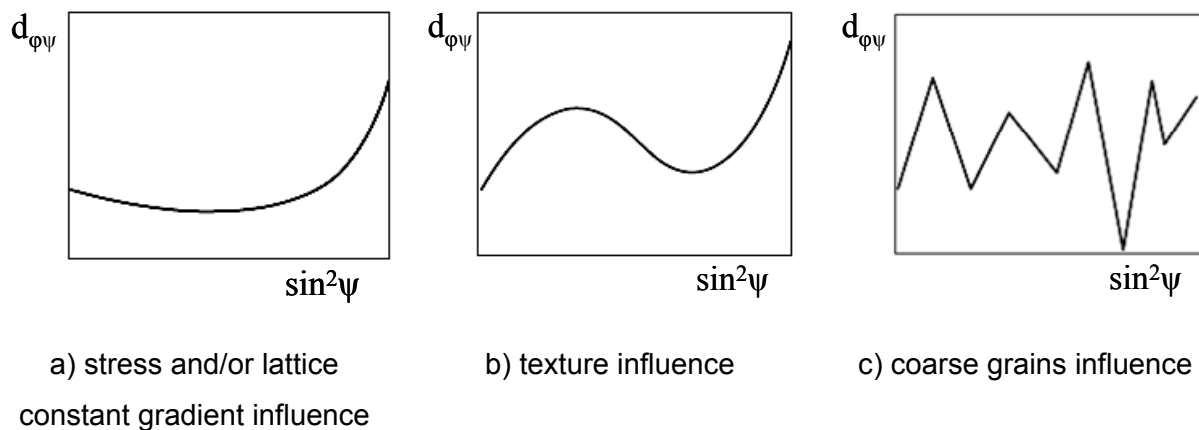


Figure 2.19: Schemes showing limited case $\sin^2\psi$ distributions: a) stress and/or lattice constant gradient, b) texture influence, c) coarse grains. Mixtures are possible [87].

- Stress gradients within the diffracting volume (Fig. 2.19a);
- Lattice constants gradients within the diffracting volume (Fig. 2.19a);
- Highly textured materials (Fig. 2.19b);

- Coarse grain materials (Fig. 2.19c);
- Multiphase materials;
- Surface roughness should be lower than the minimum average information depth;
- Non-flat surfaces: The irradiated area should be smaller than 0.4 times the radius of curvature of the analysed surface in the direction of the stress component to be determined;
- Overlapping diffraction lines;
- Broad diffraction lines.

In case of mechanical surface treatments such as SP, such limitations could be in general less important, since:

- texture is destroyed due to plastic deformation in near-surface;
- plastic deformation dramatically reduces the domain size. Otherwise, a coarse grain problem could be solved by increasing the number of diffraction crystallites through translations and/or angular oscillations of the sample, by using lattice planes with higher multiplicity factor or by using X-rays with a higher penetration depth [87].

2.5.2 Neutron Diffraction

The principle of neutron diffraction for strain measurement is shown in Fig. 2.20.

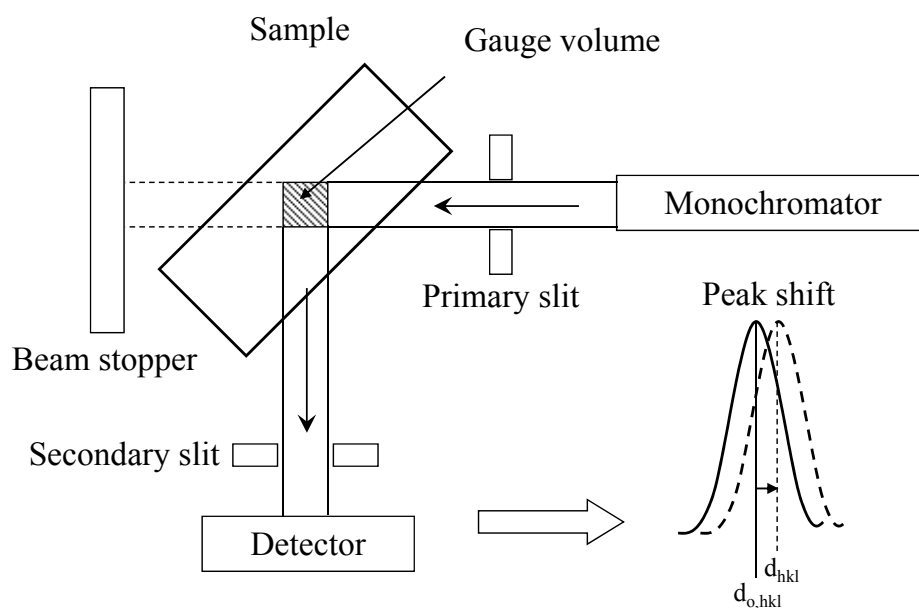


Figure 2.20: Principle of neutron diffraction for strain measurement.

Neutron diffraction has been widely used as an established technique for residual stress determination. This technique has been employed in many diverse fields such as the non-destructive investigation of large components, the determination of phase-specific residual stress in multi phase materials, the profiling of residual stress fields in welds, etc. [88–90]. Peak positions (2θ) are obtained from the diffraction data for each point and orientation of the sample and then converted into interplanar spacings d_{hkl} using the Bragg's law. They are then compared with a reference value $d_{0,hkl}$, yielding the lattice strains (see Eq. 2.3). Strains in three mutually orthogonal directions x, y, z are converted into stresses using Hooke's law (Eq. 2.8), for example:

$$\sigma_x = \frac{E_{hkl}}{(1+\nu_{hkl})(1-2\nu_{hkl})} [(1-\nu_{hkl})\epsilon_x + \nu_{hkl}(\epsilon_y + \epsilon_z)] \quad (2.8)$$

The Young's modulus E and the Poisson's ratio ν depend on the reflection hkl under investigation. The reference system x, y, z is chosen according to two criteria: (i) the principal strain/stress axes are chosen, (ii) the geometrical sample axes (with their particular symmetry) are chosen.

The main difference between the last two techniques is that Lab-XRD or ED-XRD with a limited energy range can be used only in the surface region (a depth of a few hundred micrometers), due to the strong absorption in matter, whereas neutrons can penetrate several millimetres or centimetres and hence their use constitutes the most direct technique for measuring strains inside massive materials or components [91].

As ED-XRD offers some advantages over Lab-XRD (mentioned in section 2.5.1), the time-of-flight neutron diffraction (TOF) [92] also offers a number of advantages over the conventional $\theta/2\theta$ scan. The most important is the use of the full white spectrum of neutrons delivered by the moderator of the reactor or accelerator source and, therefore, many Bragg reflections can be investigated with almost constant resolution at the same time. They represent different lattice planes within the same constant scattering volume at the same scattering angle [93].

Accordingly, one of the aims of the present work was to determine residual stress distribution in mechanically surface treated Ti-2.5Cu close to the surface (compression) and in the core region (balancing tension). This needs a combination of energy-dispersive and neutron diffraction to be able to clearly describe the influence of the full stress distribution on the HCF behavior in Ti-2.5Cu.

2.6 Thermal Relaxation of Residual Stress

Fatigue performance of engineering components can be improved by applying mechanical surface treatments which produce compressive residual stresses close to the surface. These surface treatments are performed at ambient temperature. However, many components operate at elevated temperature. Therefore, the beneficial effects of surface treatments on the mechanical properties may be reduced by the thermal relaxation of residual stresses. Thermal stress relaxation can occur, for example, in both the Ti and Ni alloys used in compressor and turbine stages. Non-uniform relaxation of the compressive layer can cause distortion of the critical aerodynamic shapes of thin blades, potentially effecting engine performance. Both magnitude and rate of thermal residual stress relaxation increase with the degree to which the material has been cold worked [94]. The higher the dislocation density and internal energy of the material, the faster a given level of residual stress will relax at a fixed temperature. Methods of surface enhancement which produce the least cold work in Ti and Ni alloys have been observed to suffer the least relaxation at engine temperatures. Laser shock peening produces minimal cold working of the surface resulting in striking resistance to thermal relaxation. No detectable relaxation of the residual stress distribution produced by LSP was observed in Ti-8-1-1 after exposure for four hours at either 230°C or 400°C [95,96]. Time and temperature influences on the residual stress relaxation during aging are controlled by a thermally activated process [97] and can be described by a Zener-Wert-Avrami function [98] (Eq. 2.9) as:

$$\frac{\sigma^{\text{RS}}(t, T)}{\sigma^{\text{RS}}(t = 0)} = \exp \left[- \left(C \cdot t \exp \left(\frac{\Delta H}{kT} \right) \right)^m \right] \text{-----} (2.9)$$

where $\sigma^{\text{RS}}(t, T)$ is the magnitude of the residual stress after isothermal annealing for time t at the absolute temperature T , $\sigma^{\text{RS}}(t = 0)$ is the initial residual stress at room temperature, ΔH is the activation enthalpy of the rate controlling process, m is an exponent, C a velocity constant and k is the Boltzmann constant (8.617×10^{-5} eV.K⁻¹). Due to the lack of literatures studying the thermal relaxation of residual stress in Ti-2.5Cu after different surface treatments, the present work aimed to achieve that study using different temperatures and times after SP, BB, USP or LPwC. The results were compared and discussed later in Section 4.5.3.

As well known, fatigue life of materials is not only influenced by induced compressive residual stresses by mechanical surface treatments but also deformation mechanism and corresponding crystallographic texture [45] as well as defects [99] such as microcracks or

voids due to manufacturing processes and/or heat treatments which were tested by using synchrotron radiation micro-computed tomography as explained later in this chapter.

2.7 Deformation Behavior of Titanium and its Alloys

The hexagonal α -phase in Ti can be deformed by slip and twinning. Slip has been observed on all three sets of slip planes commonly observed in hexagonal metals (see Fig. 2.2), i.e. basal planes $\{00.1\}$, prismatic planes $\{10.0\}$ and pyramidal planes $\{10.1\}$ [100–104]. The modes of deformation are summarized in Table 2.4.

Table 2.4: Deformation modes in α -Ti [100].

Slip systems	$\{00.1\} \langle 11.0 \rangle$	\vec{a} slip
	$\{10.1\} \langle 11.0 \rangle$	
	$\{10.2\} \langle 11.0 \rangle$	
	$\{11.2\} \langle 11.3 \rangle$	$\vec{c} + \vec{a}$ slip
	$\{10.1\} \langle 11.3 \rangle$	
Twin systems	$\{10.2\}, \{11.1\}, \{11.3\}$	c-axis extension
	$\{11.2\}, \{11.4\}, \{10.1\}$	c-axis reduction

Prism and basal planes have three slip systems. However, only two are independent of each other, resulting in only four independent slip systems. Slip on pyramidal planes does not increase the number further, since this glide is composed of a prism and a basal component and therefore cannot be considered an independent slip system [4]. According to the von-Mises criterion, it is required at least five independent slip systems for a homogenous plastic deformation of polycrystals. The operation of one of the slip systems with a so-called non-basal Burgers vector needs to be activated, either c type with slip direction $[00.1]$ or the c + a type with slip direction $\langle 11.3 \rangle$ [2] which has been observed by TEM in number of Ti-alloys [103,105]. As listed in Table 2.4, $\{10.2\}$, $\{11.1\}$ and $\{11.3\}$ twins are activated during deformation in tension resulting in an extension along the c-axis. In contrast, under compression loading parallel to the c-axis, $\{11.2\}$, $\{11.4\}$ and $\{10.1\}$ twins are activated but $\{10.1\}$ twins were observed only at relatively high deformation temperatures above 400°C [104]. Alloying elements, which have any significant solubility in α -Ti, play an important role to affect the deformation modes. For example, the role of the intermetallic phase Ti_2Cu in Ti-2.5Cu was studied. It can be concluded that twinning occurs more easily at lower temperature or under cyclic loading. Ti-2.5Cu alloy belongs to Ti–Cu binary system, where β -phase has a

limited solubility range of Cu and decomposes into α -phase and intermetallic compound rapidly with decreasing temperature [106,107]. Although twinning can be suppressed in two phase ($\alpha + \beta$) alloys by the small dimension, high solute content and the presence of precipitates, these alloys are ductile at low temperatures due to their small phase dimensions. The bcc β -phase also shows twinning in addition to slipping, but the occurrence of twinning in this phase is limited again to the single phase state and decreases with increasing solute content.

Fatigue crack growth of Ti-2.5Cu with equiaxed and lamellar microstructure has been investigated by Wang and Muller [108]. As for the deformation modes, it is well known that precipitates in the microstructure can hinder the movement of dislocation and increase the yield strength, whereas they have little effect on twinning process [109]. This change of the deformation mode due to addition of Cu causes change in crystallographic orientation [110] as explained later in the next section.

2.8 Crystallographic orientation

The crystallographic orientation refers to how the atomic planes in a volume of crystal are positioned relative to a fixed reference. In most materials there is a pattern in the orientations which are present and a propensity for the occurrence of certain orientations caused firstly during crystallization from a melt or amorphous solid state and subsequently by further thermomechanical processes [111]. This tendency is known as preferred orientation or texture. Schematic representation of random and preferred textures in polycrystalline hcp metal is illustrated in Fig. 2.21.

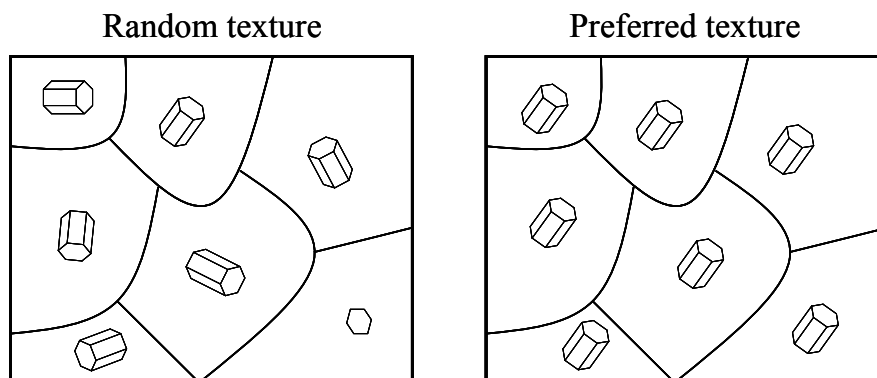


Figure 2.21: Scheme showing the difference between random and preferred textures in polycrystalline hcp metal.

The material properties, such as elastic anisotropy, plastic anisotropy, formability, yield strength, ductility, fatigue, fracture toughness and environmentally-aided fracture, are affected by texture [112]. Furthermore, the crystallographic texture can be influenced by mechanical surface treatments at the surface and in near-surface. This leads to changes in surface layer properties. Therefore, one of the aims of the present work was to study the texture gradient after various surface treatments.

2.8.1 Description of the orientation

A complete description of the polycrystalline structure requires the specification of the orientation of the crystallographic axes of each grain as well as its form and its position within the sample. This description is usually too complicated to be practicable. Therefore, polycrystalline structure is described by certain statistical distribution functions such as Orientation Distribution Function (ODF) or texture. If $\Delta V(g)$ is the volume of all crystallites having orientation (g) in the range from g to $g + \Delta g$ and V is the volume of the whole sample then the orientation distribution function (ODF) $f(g)$ [113] is defined by (Eq. 2.10):

$$\frac{\Delta V(g)}{V} = f(g)dg \text{-----} (2.10)$$

It is possible to normalize the function $f(g)$ in such a way that it is unity in the case of random orientation distribution [$f_r(g) = 1$]. On the other hand, in the case of non-random distribution, the function $f(g)$ is expressed in “Multiple of the Random Density” abbreviated as “m.r.d”. There are various descriptions of the orientation explained in [111,113]. Examples of the representation of orientation are briefly explained as follows:

a. The “Ideal Orientation” (Miller or Miller-Bravais Indices) Notation

The ideal orientation notation is used to represent an orientation (g) as conventionally written in Eq. 2.11:

$$g = (hkl) [uvw] \text{-----} (2.11)$$

where (hkl) plane is parallel to the rolled sheet plane and $[uvw]$ direction parallel to the rolling direction. If non-specific indices are quoted, the Miller indices family can be used $\{hkl\} \langle uvw \rangle$. For example, $\{110\} \langle 001 \rangle$ orientation which is called the Goss orientation is illustrated in Fig. 2.22.

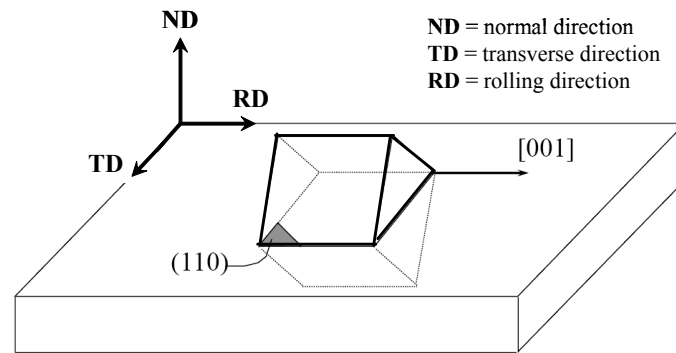


Figure 2.22: Schematic illustration of the relationship between the crystal and sample axes for $\{011\} \langle 001 \rangle$ orientation $[111]$.

As seen in Fig. 2.22, (110) lies in the plane of the sheet, i.e. the direction normal to this plane is parallel to the normal direction (ND) and $[001]$ is parallel to the rolling direction (RD).

b. Euler Angles and Euler Space

The Euler angles are three angles transforming the sample coordinate system (x, y, z) on to the crystal coordinate system (x', y', z') in order to specify the orientation as shown in Fig. 2.23.

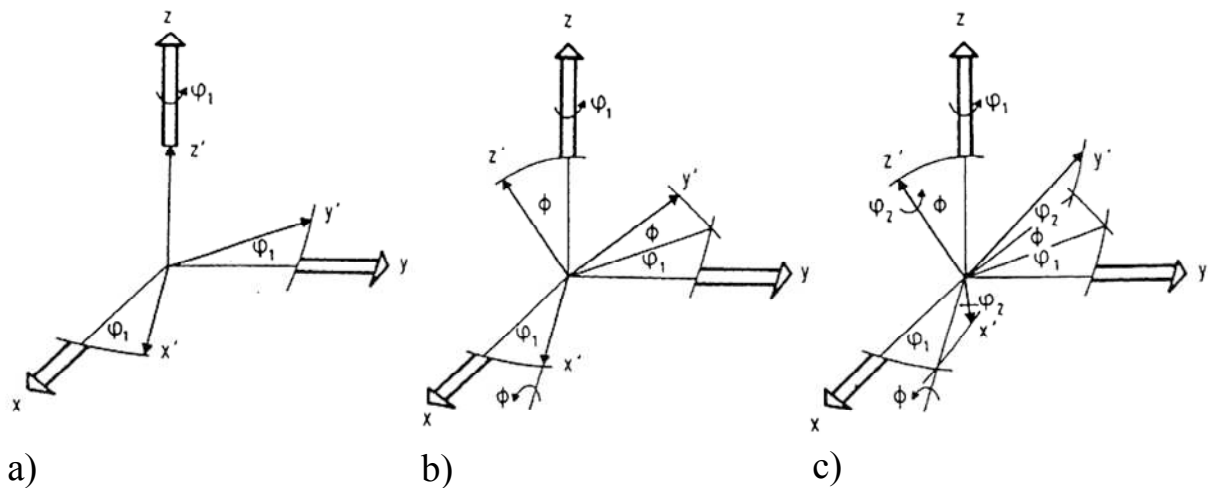


Figure 2.23: The Euler angles: $(\varphi_1, \Phi, \varphi_2)$, sample coordinate system: (x, y, z) , crystal coordinate system: (x', y', z') [113].

There are several different conventions for the Euler angle. The most commonly used are those formulated by Bunge. The orientations are:

- about the z' axis = $[001]$ through the angle φ_1 (Fig. 2.23a);
- about the x' axis = $[010]$ through the angle Φ (Fig. 2.23b);
- about the new z' axis (in its new orientation) = $[001]$ through the angle φ_2 (Fig. 2.23c).

Thus, the orientation g is defined by (Eq. 2.12).

$$g = \{\varphi_2, \Phi, \varphi_1\} = g_{\varphi_2} \cdot g_{\Phi} \cdot g_{\varphi_1} \text{-----} (2.12)$$

Whereby successive rotations are written as multiplications in the order from right to left. If the Euler angles $(\varphi_1, \Phi, \varphi_2)$ are represented as rectangular (Cartesians) coordinates, one specific orientation space can be obtained which is called the Euler space as shown in Fig. 2.24.

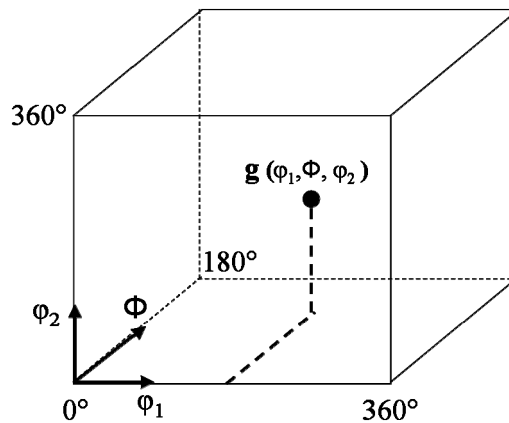


Figure 2.24: Euler space with maximum size of Euler angles (Asymmetric unit or triclinic crystal symmetry) [111].

Every point in this space represents a specific crystal orientation. Symmetries of the crystal

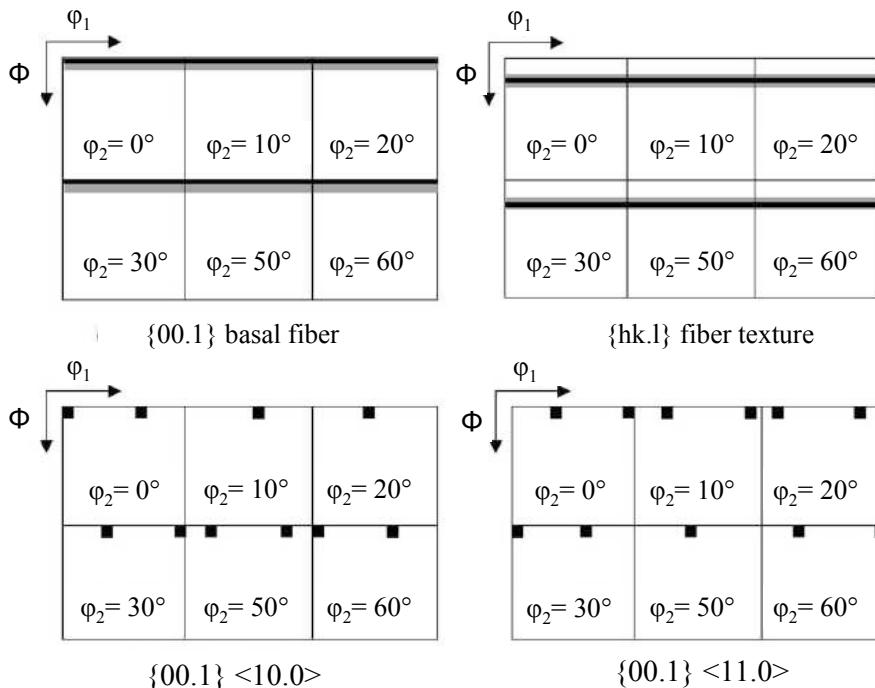


Figure 2.25: Ideal ODF positions for some low index orientation of the hcp crystalline structure [114].

and/or the sample lead to a reduction in the size of the Euler space. For example, hexagonal crystal structure and orthotropic sample symmetry, such space can be reduced to be $0^\circ \leq \varphi_1 \leq 90^\circ$, $0^\circ \leq \varphi_2 \leq 60^\circ$ and $0^\circ \leq \Phi \leq 90^\circ$. Examples of the ideal Orientation Distribution Function (ODF) positions for some low index orientation of the hcp crystalline structure are shown in Fig. 2.25 [114]. The satisfactory results can only be obtained by methods measuring a large number of crystals at the same time. This is the case with the usual pole figure measurement.

c. Pole Figure

Pole figure is a stereographic projection of polycrystalline aggregate showing the distribution of poles, or plane normals, of a specific crystalline plane using sample axes as reference axes. They are used to characterize preferred orientation in polycrystalline materials [115]. Pole figure is clearly defined by a schematic drawing of $\langle 100 \rangle$ pole on the projection plane (Fig. 2.26), in case of single crystal as a simple example. The crystal satisfies the condition for $\langle 100 \rangle$ diffraction, when the sample is positioned on the marked points.

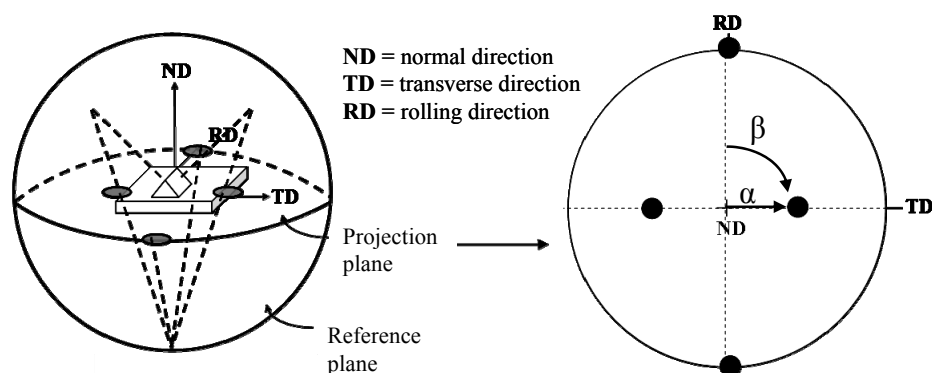


Figure 2.26: Definition of the $\langle 100 \rangle$ pole on the projection plane in case of single crystal.

As seen in Fig. 2.26, the poles are projected from the reference sphere onto a pole figure as follows. The position of a given pole on the sphere is commonly characterised in terms of angles. The angle α describes the azimuth of the pole, where $\alpha = 0^\circ$ is the north pole of the unit sphere. The angle β characterises the rotation of the poles around the polar axis, starting from a specified reference condition. Mathematically, texture can be described by ODF $[f(g)]$ with the orientation g ($\varphi_1, \Phi, \varphi_2$). Since the diffracted intensity does not depend on the rotation angle around the scattering vector, two or more pole figures have to be determined for a calculation of the ODF, where the required number of pole figures and suitable choices of hkl depend on the crystal symmetry and on the sample symmetry [116]. For the investigation of the three dimensional orientation distribution of the grains within a polycrystalline aggregate, the ODF $[f(g)]$ has to be reproduced from two-dimensional pole

figures. For this purpose two basic concepts have been developed, namely, the series expansion methods as explained in details in [113, 117–120] and the direct inversion methods [121–127].

2.8.2 Texture Measurement

a. Local Texture

X-ray diffraction is the most commonly used for local texture measurements. The essential setup of an X-ray texture diffractometer consists of an X-ray tube, a detector, and a four-circle goniometer that is called Eulerian cradle. Due to the low penetration power and small beam size in Lab-XRD, when compared to those for neutrons, local texture can be measured. However, poor grain statistics are achieved in coarse grained materials. To increase the grain statistics, sample oscillation over some millimeters or more is used during the measurement under the assumption of homogeneous texture in the oscillated area. Another way of raising the statistics is to add the pole figures measured at more than one position (or sample). Due to the strong defocusing effect and the diffraction geometry, complete pole figures cannot be measured by Lab-XRD. [116]. In order to overcome those limitations, synchrotron X-rays are used due to a high spatial resolution combined with excellent brilliance and high penetration depth for many materials [128]. The high spatial resolution results from the highly intense X-ray beam with possible sizes down to a few micrometers to be able to analyze local textures. The principle of pole figure measurement using synchrotron X-rays is similar to that of Lab-XRD. The main difference is the wavelength, which has a strong influence on the scanning routine. In addition, complete pole figures can be measured.

b. Bulk texture

Due to the high transmission of neutrons for most materials, neutron diffraction is an efficient tool for the analysis of bulk textures of polycrystalline materials. The main applications are pole figure measurements of coarse-grained materials, non-destructive measurements of identical samples at different states, investigations of unprepared natural samples, analysis of rather weak textures and the measurements of multi-phase systems [129,130]. Moreover, complete pole figures are obtained without special sample preparation, and measured pole figures can be used for ODF calculation after background intensity corrections. Although neutron diffraction allows non-destructive texture analysis, its spatial resolution is limited to the order of millimeters. On the other hand, texture analysis at localized volumes with sizes

from micrometers to centimeters is now possible by using synchrotron radiation. Advantages and disadvantages of both radiations make them complementary for measuring crystallographic textures in a wide range of materials [131].

2.9 Texture in Ti-Cu alloy compared with other in hcp metals

In the present work, it was only studied the deformation behavior of Ti-2.5Cu during in situ tensile testing. Therefore, in this section, texture in Ti-Cu alloy compared to that in hcp metals was briefly introduced. Texture development in Ti-alloys has received a lot of attention due to their applications as structural materials in aerospace. Due to the low crystal symmetry of hcp crystal structure, several families of slip systems need to be activated as described in details in Section 2.7. The critical shear stresses depend on temperature, degree of deformation including hardening characteristics and composition (particularly the c/a ratio) [132]. Metals or alloys with below-ideal c/a ratios ($c/a < 1.633$), such as Ti and Zr, tend to form textures with basal poles tilted $\pm 20^\circ$ to 40° away from ND toward TD and $[10.0]$ poles aligned with RD. For comparison with metals or alloys with c/a ratios equal to (such as Mg & Co) or above (such as Zn & Cd) the ideal c/a ratio, textures differ [133] as shown schematically in Fig. 2.27.

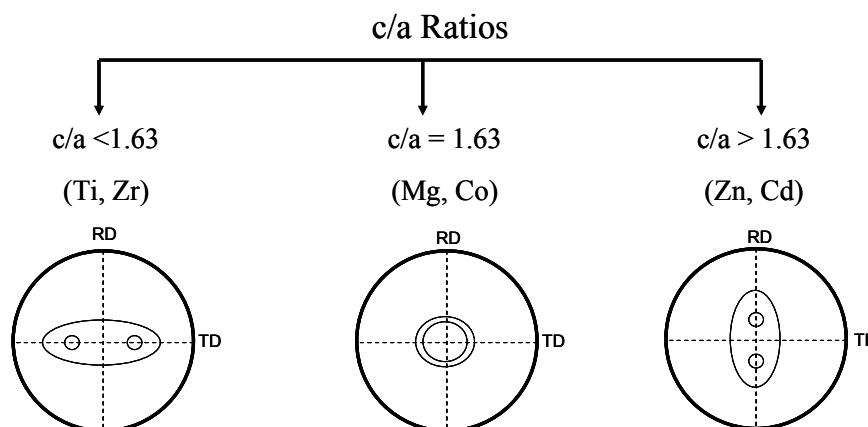


Figure 2.27: Scheme showing typical basal pole figures in rolled hcp metals with different c/a ratios.

In commercial pure Ti (CP-Ti), the c/a ratio of 1.587 allows activating the (11.2) twinning which plays an important role with (00.2) slipping for such rotation. Indeed, additions of the beta eutectoid stabilizers, the changes in texture, with the exception of Cu, formed a similar pattern of CP-Ti. With further increase in alloying addition, the β -phase becomes stable and at approximately 16 to 20% volume fraction beta abrupt transition in the texture is observed.

The new basal pole texture is similar to that of Zn or Mg sheet material. However, Ti still has the [10.0] parallel to the rolling direction [110]. An exception to the above general behavior was found in the Cu which formed nearly an ideal texture (00.1) [10.0] with addition of 0.55 wt % Cu or 1.61 wt % Cu as shown in Fig. 2.28.

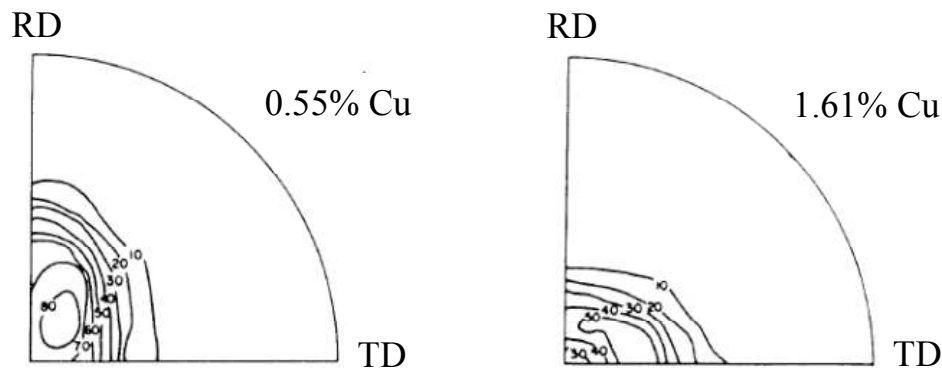


Figure 2.28: Effect of Cu-addition on the change of the basal pole figure of pure Ti [110].

Furthermore, additions of Al, an α -stabilizer, cause the same effect of Cu on the basal pole to move toward the sheet normal. In both cases of additions Cu or Al, the reason of texture changes could be explained by a very fine structure which could probably suppress {11.2} twinning. In the present study, the effect of 2.5 wt % Cu on the bulk texture of Ti-2.5Cu as well as the texture gradients after different surface treatments were studied.

2.10 Microtomography

2.10.1 X-Ray Microtomography

X-ray computed tomography (CT) is an established method for cross-sectional and fully three dimensional imaging (3D) of the internal structure of an object. At the microscopic scale CT is known as microtomography (μ CT). The performance of μ CT systems, however, is strongly limited by the properties of conventional X-ray tube sources, which always require a trade off between source size (resolution) and intensity (speed). These limitations can be circumvented by the application of synchrotron radiation as an intense X-ray source [134]. X-ray synchrotron microtomography provides higher quality data in term of signal to noise ratio and a high spatial resolution compared with classical laboratory equipments. This is due to the fact that synchrotron beams are tuneable in terms of energy and size and are characterized by a high flux of photons. [135]. The illumination of the material by the synchrotron radiation beam (in almost all cases) does not influence its microstructure significantly. Compared to

Lab-XRD microfocus sources, synchrotron X-rays provide both a significantly higher image and time resolutions and further enable the use of tomography in the phase contrast mode [136]. Therefore, synchrotron radiation micro-computed tomography (SR μ CT) has become an efficient tool for the damage evolution in materials subjected to static and dynamic mechanical loading such as fatigue cracks.

Fatigue crack initiation and growth have been studied in different materials or alloys by using X-Ray Microtomography [137–139]. For example, the study of fatigue cracks in ($\alpha + \beta$) alloy Ti-alloy Ti-6246 by X-ray microtomography revealed that during the fatigue experiment the crack grows faster in the bulk than that at the surface [140].

As mentioned previously, mechanical surface treatments produce a cold worked and a compressive layer close to the surface. It results in drastic enhancement of the HCF strength. This is mainly related to the shift in fatigue crack nucleation site from the surface to subsurface regions, i.e., from the air to a quasi-vacuum environment. Furthermore, this enhancement might be attributed to the closure of surface or near-surface defects such as microcracks or voids due to manufacturing processes and/or heat treatments. This led to one of the aims of the present study to investigate of the possibility of near-surface defects existence and closure in Ti-2.5Cu after SP or BB.

2.10.2 Neutron Microtomography

The unique ability of neutron imaging to provide information on materials and structures, sometimes inside objects opaque to X-rays, makes neutron radiography and tomography quite powerful for a number of applications— including studies of water vapour propagation and condensation in fuel cells, spatially correlated water phase transitions, water propagation in heat exchangers and concrete structures, internal structures within geological samples, water uptake by plants, oil and fuel distribution in car engines and fuel injectors, water contamination in mechanical structures, as well as many others [141]. The contrast uniqueness in neutron imaging is based on the fact that neutrons interact with the nucleus inside the atom instead of electrons (as occurs with X-rays). This leads to a widely different contrast mechanism as compared to X-rays. Many organic materials are quite opaque to neutrons, whereas many metals are relatively transparent; hence they can be easily penetrated by neutrons. Obviously the contrast and resolution of neutron imaging also depend on the quality of the neutron beam line and detection system used in the experiments. Detection

efficiency, spatial and temporal resolution, dynamic range and background noise level of the neutron detector are among the crucial parameters defining the ultimate performance of neutron radiography or microtomography setups [142].

3 Materials and Methods

3.1 Introduction

This chapter introduces the material processing, heat treating, tensile testing as well as the parameters used for the mechanical surface treatments such as shot peening, ball-burnishing, laser shock peening and ultrasonic shot peening. Furthermore, the methods used for evaluating surface roughness, residual stress, work hardening, crystallographic textures, fatigue and the possibility of cracks existence due to manufacturing processes are described.

3.2 Materials

Ti-2.5Cu was received as a 10 mm thick rolled plate. The samples were cut from this plate with an area of $20 \times 20 \text{ mm}^2$ and a thickness of 5 or 10 mm³ perpendicular to the rolling direction followed by two different heat treatments. Solution heat treatment (SHT) at 805 °C (just above the eutectoid temperature) for 1 hour was applied to the samples followed by water quenching. The other was SHT followed by double aging (SHT+A) by annealing at 400 °C for 8 hours and then annealing at 475 °C for 8 hours and followed by air cooling. Aging at 400 °C develops the maximum number of well distributed nuclei for precipitation. The other aging at 475 °C forms homogeneously the precipitation of a fine dispersion of the Ti₂Cu. On the other hand, a direct aging at 475 °C results in an inhomogeneous distribution of precipitations and therefore a limited increase of the tensile properties.

Ti-54M was received as a square (38 x 38 mm) bar stock in as-milled condition. A cut bar with a length of 50 mm was β -annealed at 1010 °C for 30 min followed by water quenching. This bar was unidirectionally rolled at 800 °C with a total deformation degree of $\varphi = 1.4$. From the rolled plates, blanks were cut with dimension of $20 \times 20 \times 5 \text{ mm}^3$ and were heat treated to obtain a fully equiaxed microstructure by annealing at 800 °C for 1 hour followed by water quenching. All blanks were given a final heat treatment at 500 °C for 24 hours to age-harden the α -phase by Ti₃Al precipitates and the β -phase by fine secondary α precipitates.

LCB was received as a swaged rod of 14.3 mm in diameter. The rod was unidirectionally rolled at 760 °C to a thickness of 5 mm corresponding to a maximum deformation degree of about $\varphi = 1$. Blanks ($20 \times 20 \times 5 \text{ mm}^3$) were cut from the plate, recrystallization annealed at

760 °C for 1 hour followed by water quenching. The blanks were final heat treated at 540 °C for 8 hours and then air cooling.

The chemical compositions of these alloys are listed in Table 3.1.

Table 3.1: Chemical composition of Ti-2.5Cu, Ti-54M and LCB (wt. %)

	Al	Cu	Fe	Mo	Sn	V	Zr	Ti
Ti-2.5Cu	0.018	2.500	0.073	<0.010	0.048	0.015	0.003	Rest
Ti-54M	5.030	-	0.506	0.570	-	3.950	0.005	Rest
LCB	1.371	-	4.500	6.770	0.343	0.013	0.008	Rest

Threaded cylindrical tensile samples of Ti-2.5Cu and Ti-54M were machined having a gauge length and a diameter of 20 and 4 mm, respectively. Tensile tests were also conducted on LCB flat samples having a gauge length of 30 mm, a width of 8 mm and a thickness of 3 mm. All tests were carried out at ambient temperature with an initial strain rate of 10^{-3} s^{-1} .

For metallographic preparation, mounted samples were ground with rotating discs of abrasive paper. The finest grade of paper used was 2400 followed by mechanical polishing using a soft cloth impregnated with abrasive Al_2O_3 particles and a water lubricant. The samples were etched using Kroll's reagent with a composition of 100 ml of distilled water, 2–6 ml of 65% Nitric acid (HNO_3) and 1–3 ml of 40% hydrofluoric (HF) acid.

3.3 Surface Treatments

The samples were mechanically surface treated on one face or on both faces of the 20 x 20 mm^2 areas for residual stress measurements and on cylindrical samples for fatigue testing by applying SP, USP, BB or LPwC.

SP was performed at TU Clausthal in Germany using automatic compressed-air SP machine (pressure-suction system) from OSK-Kiefer Company. Cast steel shots (S330) were used with an average shot diameter of 0.80 mm (0.033 inch), a hardness of 460 HV and a nominal chemical composition (wt. %) of 0.80–1.20% C, at most 0.05% S and at most 0.05% P. USP was applied at MTU Aero Engines in Germany using 100Cr6 bearing steel balls with diameter of 1.5 mm, hardness of 700 ~ 800 HV and a nominal chemical composition (wt. %) of 0.93–1.05% C, 1.35–1.60% Cr, 0.15–0.35% Si, 0.25–0.45% Mn, 0.015% S, 0.025% P and 0.10% Mo. The main reason for using 0.8 mm shots in SP and 1.5 mm balls in USP is their higher mass and therefore the greater compressive residual stresses that can be achieved.

Peening was performed to roughly 100% coverage in both SP and USP using the same Almen intensity of 0.20 mmA. It was observed no over-peening effect even at higher Almen intensity (> 0.20 mmA) on the fatigue life enhancement as reported in [135]. The influence of the different peening media parameters used in SP and USP, such as speed, diameter and hardness, with the same Almen intensity on the surface and near-surface characteristics was considered when discussing the experimental results. In addition, the samples were ball-burnished at TU Clausthal using a conventional lathe and a hydrostatic tool from Ecoroll Company. During BB, a hard metal ball ($\varnothing 6$ mm) was pressed onto the surface applying a pressure of 300 bar. BB was carried out using a rotational speed of 150 rpm and a feed rate of 0.170 mm/rev. LPwC was carried out at Toshiba Corp. in Japan using a compact Q-switched and frequency-doubled Nd:YAG laser with a pulse duration of 8 ns and a wavelength of 532 nm. The fired laser pulses adjusted to have a pulse energy of 50 mJ and impinged on the sample with a spot diameter of 0.4 mm, resulting a peak power density of $5 \text{ GW}\cdot\text{cm}^{-2}$. Water was used as a tamping material limiting the thermal expansion of plasma gas. LPwC has some characteristics mentioned in [37]. The instrument setup is shown in Fig. 3.1.

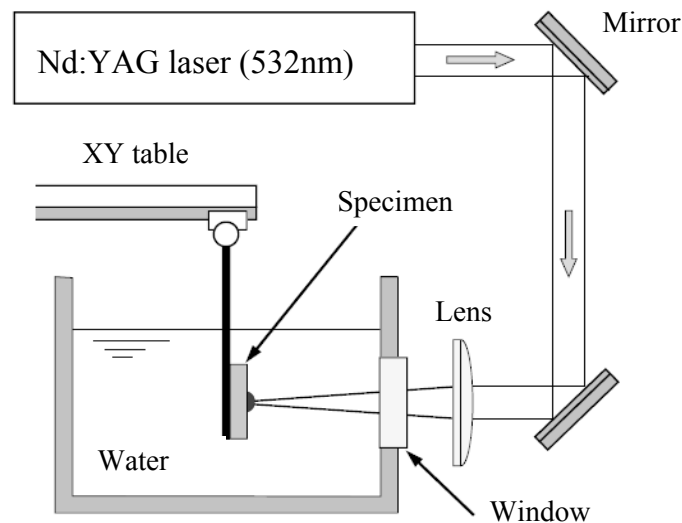


Figure 3.1: Experimental setup of LPwC process [38].
(LPwC = Laser shock peening without coating)

Some samples were electrolytically polished to serve as reference as well as to remove some layers to be able to determine residual stress profiles in deeper region by using X-ray diffraction as explained later in this chapter. The electropolishing (EP) process was carried out using electrolyte with a composition of 240 ml of Methanol, 180 ml of 1-Butanol and 30 ml of Perchloric acid at a temperature of -25 °C with a voltage of 20 V and a time of 25 minutes to remove a layer thickness of 100 μm approximately.

3.4 Surface roughness

The surface roughness of the various conditions was determined by means of an electronic contact (stylus) profilometer instrument (Perpethometer). The average absolute value of the five highest peaks and the five lowest valleys over the evaluation length (R_z) was reported (DIN 4768). The average of three roughness measurements was taken. The parameter (R_z) was used rather than the average roughness (R_a) comparing all the peaks and valleys to the mean line, since quite different surfaces could have the same R_a and consequently perform in different manner [143].

3.5 Microhardness

Microhardness was determined by means of a Struers Duramin tester using a square base pyramid shaped indenter for testing in a Vickers tester, a nominal force of 100 gf (HV0.1) and a loading time of 10 s. The hardness testers in the Duramin series conform to the standard (DIN EN ISO 6507). The average of three measurements was taken at each depth to construct the hardness-depth profiles.

3.6 Residual Stress and Full Width at Half Maximum

3.6.1 Laboratory X-ray Diffraction (Lab-XRD)

Residual stresses at the surface were determined by using Lab-XRD at TU Clausthal in Germany. The instrument is Siemens product model D5000 with automatic operation (PC-controlled). The components of X-ray diffractometer are shown schematically in Fig. 3.2. The diffractometer consists of the goniometer supporting the sample and detector as well as allowing precise movement. The goniometer has four different circles of rotation to adjust sample and detector positions (see Fig. 3.2) as follows:

- Circle 1 (θ) rotates the sample about a vertical axis;
- Circle 2 (2θ) turns the detector about a vertical axis too;
- Circle 4 (ψ) tilts the sample about a horizontal axis (called psi);
- Circle 4 (ϕ) rotates the sample about an axis normal to the sample surface through the center of the holder and called phi.

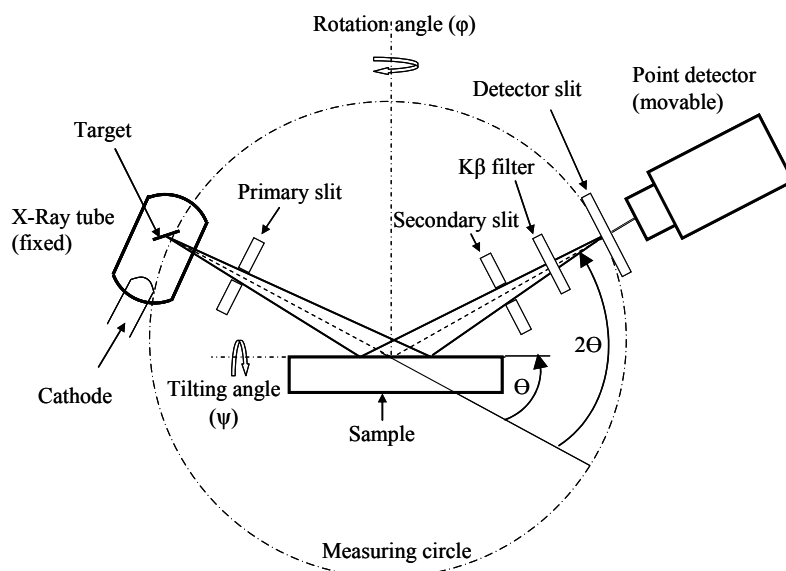


Figure 3.2: The schematic layout of X-ray Diffractometer (Lab-XRD) model Siemens D 5000 with beam path in $\theta/2\theta$ mode [75].

The residual stress measurements were carried out with the parameters listed in Table 3.2 after a calibration with Gold (Au) powder sample.

Table 3.2: Lab-XRD (D5000) parameters

X-Ray tube	Cu ($\lambda = 1.541 \text{ \AA}$)
K β filter	Ni with thickness of 12 μm
Measuring circle diameter (mm)	401
Slit size (mm)	- Primary slit: 3 x 3 - Secondary slit: 2 x 16 - Detector slit: 1 x 16
Reflection	(21.3)
Diffraction elastic constants [144] (MPa^{-1})	$S_1(21.3) = -2.88 \times 10^{-6}$ $\frac{1}{2} S_2(21.3) = 11.74 \times 10^{-6}$
Detector	Point (scintillation)
Scan type	Continuous
2-Theta 2θ ($^\circ$)	136 – 144
Step size ($^\circ$) / Time (s/step)	0.08 / 30
Rotation angle ϕ ($^\circ$)	0
Tilting angle ψ ($^\circ$)	-52.5 to +52.5 (13 steps) with $\Delta \sin^2 \psi = 0.105$
Maximum penetration depth (μm)	11.7 approximately

The data were evaluated based on $\sin^2\psi$ method as explained in details in Chapter 2. In addition, the diffraction elastic constants were calculated using the elastic stiffness (C-constants) reported elsewhere [144]

3.6.2 Energy-Dispersive X-ray Diffraction using Synchrotron Radiation

a. Residual Stress

The residual stress measurements close to the surface were performed by energy-dispersive X-ray diffraction (ED-XRD) using synchrotron radiation at BESSY-II in Berlin (Beamline EDDI). The characteristic of the used beamline EDDI offers a white X-ray beam with an energy range of 10–120 keV.

The components of X-ray diffractometer are shown schematically in Fig. 3.3. Since any diffraction line $E_{(hkl)}$ possesses another photon energy, the signal of any reflection belongs to a different depth in the sample.

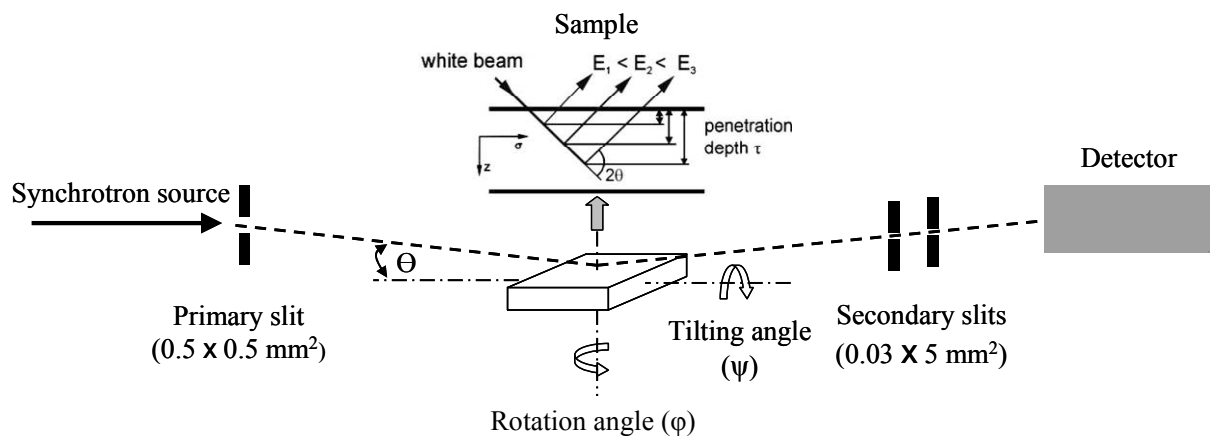


Figure 3.3: Schematic layout of energy-dispersive X-ray diffractometer (Beamline EDDI at BESSY in Berlin).

Energy spectrum of the 7T multipole wiggler (photon flux through a pinhole of $1 \times 1 \text{ mm}^2$, 30 m behind the source), scaled up to a ring current of 250 mA is shown in Fig. 3.4 [145].

The flux may be sufficient for many experiments even beyond 80 keV up to 120 keV. However, in the present investigation on Ti-2.5Cu, for example, it was found that the flux is insufficient to get adequate intensities beyond 80 keV. An example of the energy spectrum of Ti-2.5Cu is illustrated in Fig. 3.5 using 2θ of 8° .

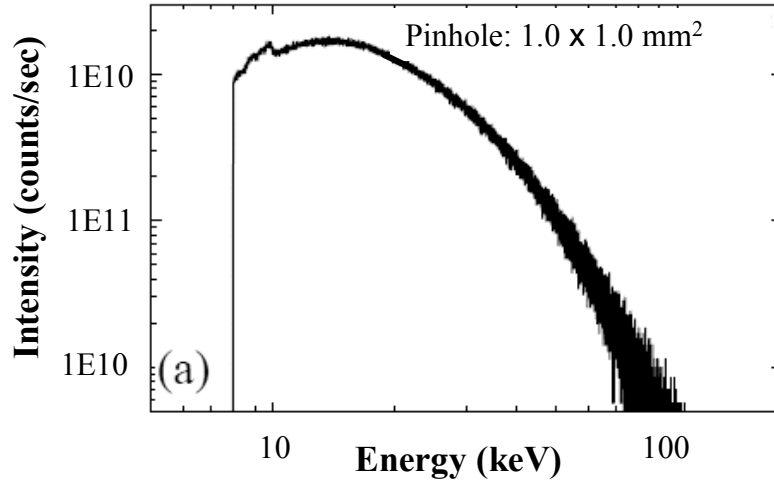


Figure 3.4: Energy spectrum provided by the wiggler and the beam characteristics [145].

The residual stresses were determined with the parameters listed in Table 3.3 and evaluated by means of the $\sin^2\psi$ method. The calibration of the instrument was carried out by using Tungsten (W) powder.

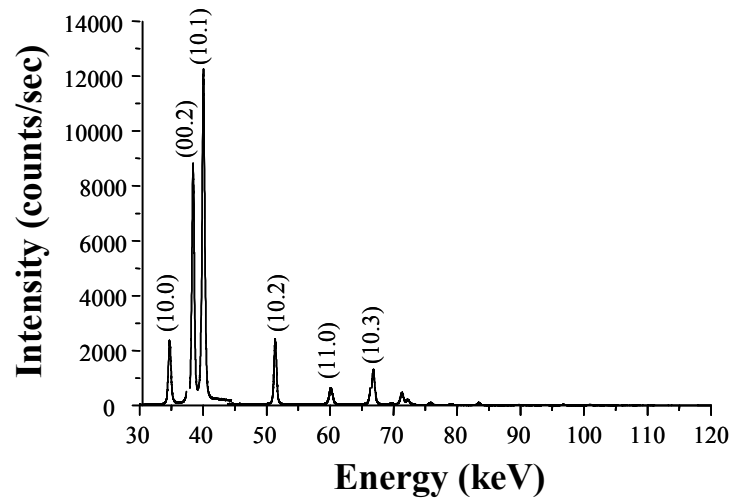


Figure 3.5: Energy spectrum of Ti-2.5Cu ($2\theta = 8^\circ$).

To achieve a high information depth which depends on the absorption of the material, to get adequate intensities and to avoid peak-overlapping, a scattering angles $2\theta = 8^\circ$ for Ti-2.5Cu and Ti-54M and $2\theta = 6^\circ$ for LCB were chosen. ED-XRD gives a complete diffraction spectrum for a fixed detector position. A modified multi-wavelength approach [146] for any energy line $E_{(hkl)}$ gives an average penetration depth $\tau_{(hkl)}$ (Eq. 3.1):

$$\tau_{(hkl)} = \frac{\tau_{(hkl)\min} + \tau_{(hkl)\max}}{2} \quad (3.1)$$

Table 3.3: Measurement parameters of residual stress measurement by ED at BESSY (Beamline EDDI)

X-Ray source	Synchrotron radiation
Energy range (keV)	10 – 120
Wavelength range (Å)	1.240 – 0.103
Slit size (mm)	- Primary slit: 0.5 x 0.5 - Secondary slits: 0.03 x 5
Detector	Energy-dispersive Germanium detector
2-Theta angle 2θ (°)	8 for Ti-2.5Cu and Ti-54M 6 for LCB
Rotation angle φ (°)	0 and/or 90
Tilting angle ψ (°)	0 to 80 (21 steps)
Inclination mode	Side inclination
Peak position method	Gauss or Pseudo-Voigt depending on the peak profile

where $\tau_{(hkl)\min}$ and $\tau_{(hkl)\max}$ are the minimum and the maximum penetration depths corresponding to the maximum and minimum tilting angles, respectively. The diffraction elastic constants (DEC) of alpha and beta reflections were calculated by the Kröner–Model [147]. The reflections, diffraction elastic constants and penetration depths are listed in Table 3.4. Due to the influence of the crystallographic textures on the intensities, some reflections such as (00.2) and (00.4) could be ignored when evaluating the residual stresses. The gauge volume due to the slit system is schematically shown in Fig. 3.6.

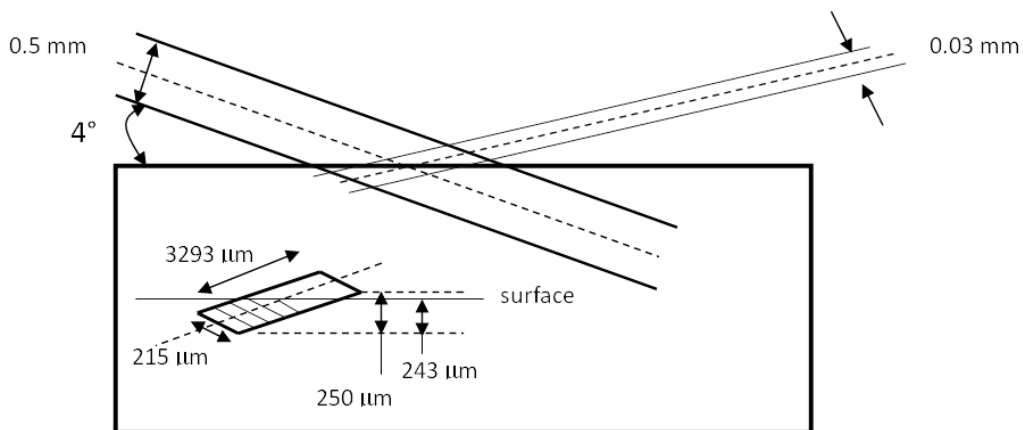


Figure 3.6: Scheme showing the gauge volume due to slit system.

Table 3.4: Reflections, diffraction elastic constants and penetration depths.

		2 θ	α -phase reflections							β -phase reflections			
			10.0	00.2	10.1	10.2	11.0	10.3	11.2	20.1	110	200	211
Defraction elastic constant (10^{-6} Mpa $^{-1}$)	S ₁		-2.98	-2.32	-2.90	-2.72	-2.98	-2.58	-2.87	-2.96	-2.98	-2.98	-2.97
	$\frac{1}{2}$ S ₂		12.03	10.11	11.80	11.28	12.03	10.87	11.73	11.97	12.03	12.03	11.99
Maximum penetration depth [$\tau_{(hkl)_{max}}$] (μ m)	6°		39.38	50.59	57.12	120.53	188.43	252.46	303.00 **		50.70	133.44	258.95
Average penetration depth [$\tau_{(hkl)}$] (μ m)	6°		23.46	29.36	33.05	61.59	105.83	127.09	129.65		27.81	74.78	145.12
Maximum penetration depth* [$\tau_{(hkl)_{max}}$] (μ m)	8°		23.15	29.74	33.58	70.84	110.77	148.34	178.41	184.93			
Average penetration depth [$\tau_{(hkl)}$] (μ m)	8°		14.20	18.11	20.46	41.31	60.79	77.37	89.04	91.20			

* The depth at which the beam intensity is reduced to 1/e of the primary intensity (I_0) $\tau_{(hkl)} = (\sin\theta \cdot \cos\psi) / 2\mu$, where μ is the linear absorption coefficient.

** This penetration depth is greater than that due to the slit system. Therefore, they were ignored.

As seen in Fig. 3.6, the maximum penetration depth due to the slit system is about 243 μm . Therefore, the higher order reflections, such as (21.1) and (11.4), which exceeds the gauge volume due to the slit system (see Table 3.4) have been ignored.

b. Full Width at Half Maximum (FWHM)

Work hardening or dislocation density distribution can be evaluated by means of X-ray diffraction peak broadening using characteristic parameters of individual peak profiles, such as the full width at half maximum (FWHM) or the area/height XRD-peak ratio (integral breadth). It is well known that besides the instrumental contribution, there are two main types of broadening: the size and the strain components. The former one depends on the finite size of the coherent diffraction domains and the latter is caused by any lattice imperfection (point, line or plane defects). The strain field of linear defects, such as dislocations, is of long-range character, therefore their diffraction effects cluster around the fundamental Bragg reflections [148,149]. In the present work, FWHM was also determined by using ED-XRD. The (10.3) reflection was used due to its high multiplicity factor ($n = 12$) and corresponding reliability of the results as well as good statistics. The FWHM of (10.3) reflection was calculated by using the Pseudo-Voigt function [150] as shown in Fig. 3.7. It should be pointed out that the microstructures of Ti-54M and LCB, as shown later, consist of both fine α and β grains ($< 3 \mu\text{m}$) which could markedly decrease due to the effect of local plastic deformation produced in the surface layers after applying surface treatments. This could result in a pronounced peak broadening due to not only dislocation density but also fine grain size. Therefore, FWHM was calculated only for Ti-2.5Cu having a grain size of 20 μm .

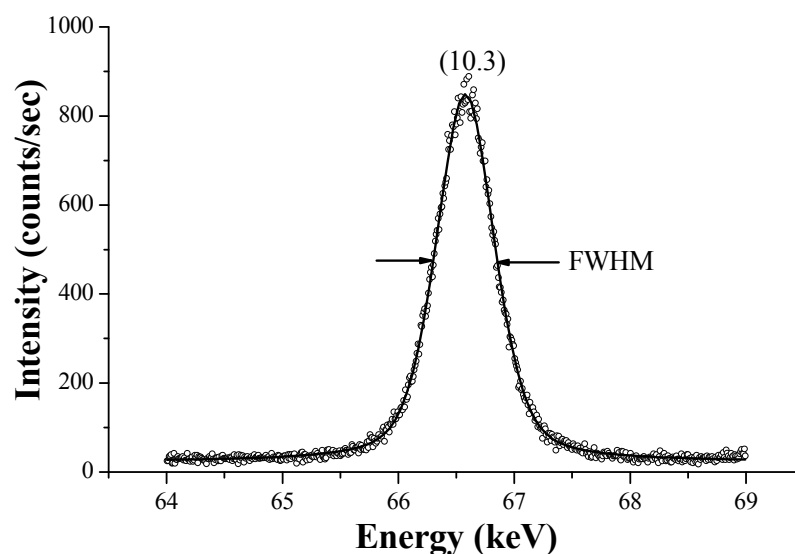


Figure 3.7: (10.3) peak fitted by Pseudo-Voigt function to define FWHM in Ti-2.5Cu.

3.6.3 Neutron Diffraction

Residual strains in the near-surface layer and in the core region of Ti-2.5Cu were determined using the neutron diffractometer (Beamline STRESS–SPEC) at FRM II in Munich [151]. The measurement layout is shown schematically in Fig. 3.8.

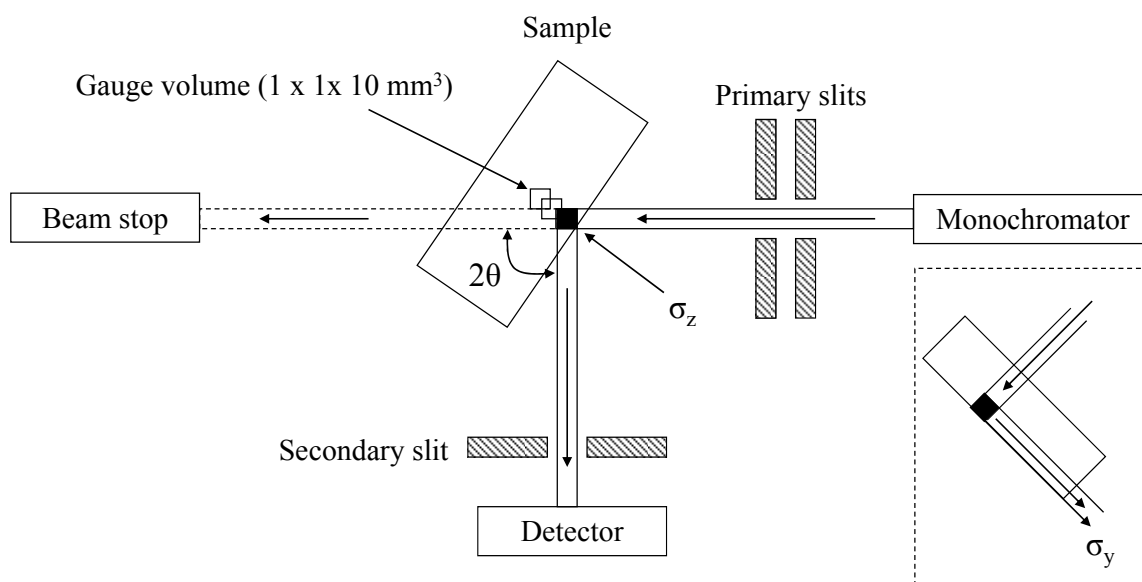


Figure 3.8: Schematic layout of the neutron scattering experiment (Beamline Stress-Spec) at FRM II in Munich.

The parameters of the neutron diffractometer are listed in Table 3.5. The size of the primary slit is $1 \times 10 \text{ mm}^2$ and the secondary slit was set with a size of 1 mm in width.

Table 3.5: Neutron diffractometer parameters

Wavelength (Å)	1.42 (Beamtime No. 1) 1.36 (Beamtime No. 2)
Monochromator	Si (400)
Detector	Position Sensitive Detector (PSD), $20 \times 20 \text{ cm}^2$
Slit size (mm)	- Primary Slit: 1×10 - Secondary slit: 1
Detector distance (mm)	1035 (Beamtime No. 1) 1050 (Beamtime No. 2)
2-Theta angle 2θ (°) (hk.l)	97.1 (21.1) & 101.4 (11.4) (Beamtime No. 1) 92.2 (21.1) (Beamtime No. 2)
Diffraction elastic constants (MPa ⁻¹)	S_1 (21.1) = -2.97×10^{-6} , $\frac{1}{2} S_2$ (21.1) = 11.99×10^{-6} S_1 (11.4) = -2.66×10^{-6} , $\frac{1}{2} S_2$ (11.4) = 11.13×10^{-6}

As seen in Fig. 3.8, the gauge volume is defined by the dimension of both primary slit in the incident beam and secondary slit in the diffracted beam. Therefore, the sampling gauge volume is a nearly square base of $1 \times 1 \text{ mm}^2$ and a length of 10 mm. Two stress components were determined, in-plane stress component parallel to the rolling direction (σ_y) and normal component to the mechanically surface treated surface (σ_z). The measurements were carried out by using two beamtimes with different wavelengths. When the gauge volume is only partially immersed in the sample, the center-of-mass of the diffracting volume does not coincide with the geometrical centre of the gauge volume as illustrated in Fig. 3.9 [152].

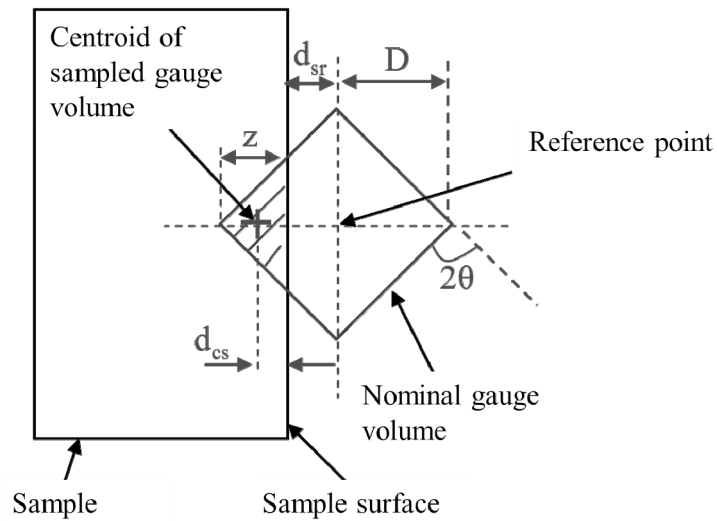


Figure 3.9: Schematic illustration showing the partially immersed nominal gauge volume in the sample and the sampled gauge volume.

Consequently, the depth of sampled gauge volume from the surface (d_{cs}) was calculated using the following correlations [152,153]:

- If the sample is less than half inside the nominal gauge volume ($-D \leq d_{sr} \leq 0$, or equivalently $0 \leq Z \leq 2D$), Eq. 3.2 can be used. Where D is the half-diagonal of the nominal gauge volume normal to the surface, d_{sr} is the distance between the surface and the instrument reference point (see Fig. 3.9) and $Z = D + d_{sr}$.

$$|d_{cs}| = \frac{[(2+aZ) \cdot e^{-aZ} - (2-aZ)]}{a[e^{-aZ} + aZ - 1]} \text{-----} (3.2)$$

Where $a = 2\mu_a / \sin\theta$ and μ_a is the linear attenuation coefficient.

- If the sample is more than half inside the nominal gauge volume ($0 \leq d_{sr} \leq D$, or equivalently $D \leq Z \leq 2D$), Eq. 3.3 can be used.

$$|d_{cs}| = \frac{[(2 + aZ) \cdot e^{-aZ} + (2 - aZ + 2aD) + (2aD - 2aZ - 4) \cdot e^{-ad_{sr}}]}{a[(e^{-aZ} - aZ + 1) + 2(aD - e^{-ad_{sr}})]} \quad (3.3)$$

Due to the texture influences, the reflection (21.1) was used to determine the strain component within the surface plane (Y-direction which is parallel to the rolling direction RD), while the (11.4) reflection was used to determine the strain component normal to the surface (Z-direction). The unstrained interplanar spacing ($d_{0,(hkl)}$) was obtained by cutting a thin sample with a thickness of 2 mm from the core region of the virgin sample with thickness of 10 mm to relieve any residual stresses. The $d_{0,(21.1)}$, $d_{0,(11.4)}$ values of Ti-2.5Cu (SHT) and Ti-2.5Cu (SHT +A) are listed in Table 3.6.

Table 3.6: Unstrained interplanar spacing ($d_{0,(hkl)}$)

Material	$d_{0,(21.1)}$ (Å)	$d_{0,(11.4)}$ (Å)
Ti-2.5Cu (SHT)	0.94395	0.91697
Ti-2.5Cu (SHT+A)	0.94471	Not measured*

* It was found from the first measurement which was conducted on Ti-2.5Cu (SHT) that the stress component in the z-direction (σ_z) can be ignored but the strain component was calculated using Hooke's law (Eq. 2.7)

It is clearly shown that the increase of $d_{0,(21.1)}$ after aging is due to the precipitation influence on the lattice spacing. In order to reduce the surface influence on the peak positions, a θ scan was carried out through the thickness (5 mm) at two positions. Firstly, the sample was located at 2θ -angle of 92.2° and at ω -angle of 46.1° (hereafter called original position), where ω is the rotation angle around the goniometer axis as shown in Fig. 3.10a. Secondly, the sample at the original position was turned 180° by changing the ω -angle to be 226.1° (hereafter called turned 180° position) as shown in Fig. 3.10b.

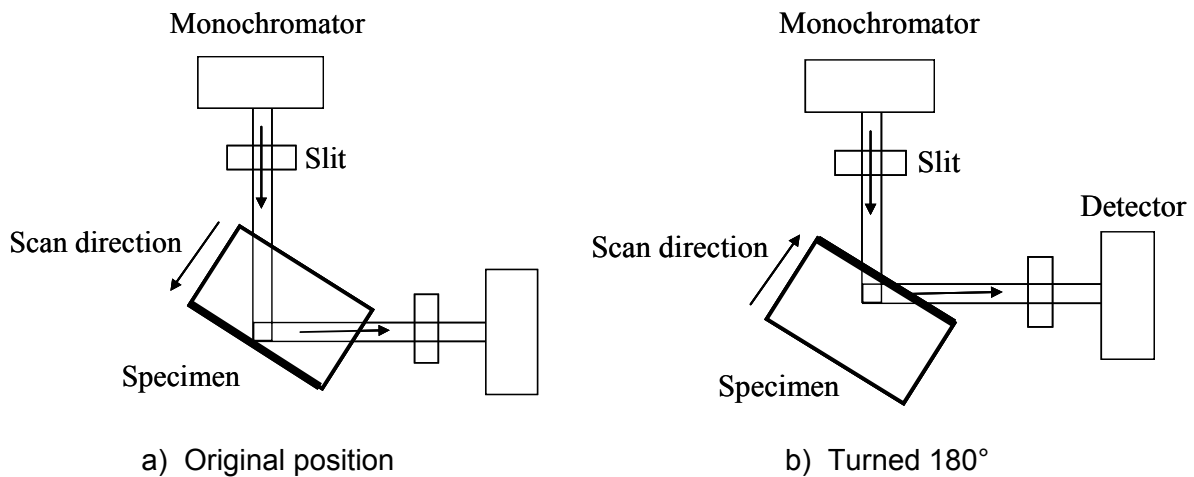


Fig. 3.10: Sample positions to reduce surface effect.

An example of peak position-depth distributions after BB is illustrated in Fig. 3.11.

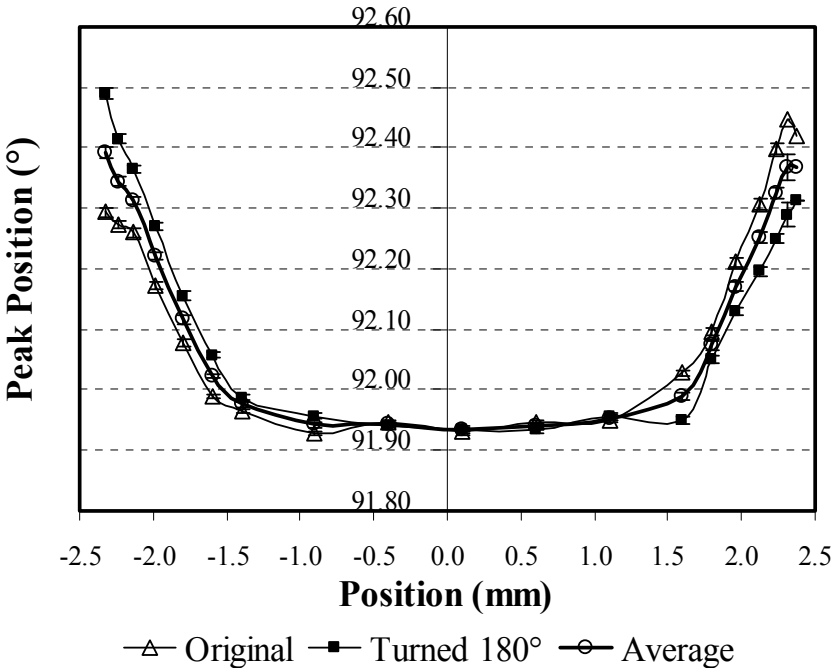


Figure 3.11: Peak position distribution after ball-burnishing (BB).

3.6.4 Incremental Hole Drilling Method (IHD)

The residual stresses were calculated from residual strains using the incremental hole-drilling method (IHD) according to ASTM E 837–01. This method involves attaching strain gauge rosettes to the surface, drilling a hole in the vicinity of the gauges and measuring the relieved strains using an oscillating drill with 1.9 mm diameter driven by an air-turbine with a rotational speed of 200,000 rpm. The induced strains in the surface layers were measured at drilled depths of about every 20 μm. The measured strains are then related to relieved principal stresses through a series of equations using the macroscopic Young’s modulus and Poisson’s ratio. A strain gauge rosette with three elements of the general type schematically illustrated in Fig.3.12 is placed in the area under consideration. The numbering scheme for the strain gauges follows a clockwise convention. A hole is drilled at the geometric centre of the strain gauge rosette to a depth of about 0.4 of the mean diameter of the strain gauge circle, D. The residual stresses in the area surrounding the drilled hole relax. The entire measurement process is PC-controlled. This ensures a high degree of measurement reliability as well as optimum reproducibility [154].



Figure 3.12: Hole drilling rosette.

3.7 Crystallographic Texture

3.7.1 Local Crystallographic Texture Using Lab-XRD

Local crystallographic texture close to the surface was obtained by using Lab-XRD. The instrument and the diffractometer parameters have been described in Section 3.6.1 with some differences corresponding to texture measurements. The texture measurements were conducted on the surface treated Ti-2.5Cu with rotation angle (φ) from 0° to 360° and tilting angle (ψ) from 0° to 70° with a step size of 5° . Two slits were used in that measurement, primary slit with a size of $3 \times 3 \text{ mm}^2$ and secondary slit with a size of $6 \times 16 \text{ mm}^2$.

3.7.2 Bulk Texture

a. Bulk Crystallographic Texture Using Neutron Diffraction

Bulk crystallographic texture was measured by using neutron diffraction at the Helmholtz-Zentrum Geesthacht Centre (Beamline TEX-2) as shown in Fig. 3.13 [155].

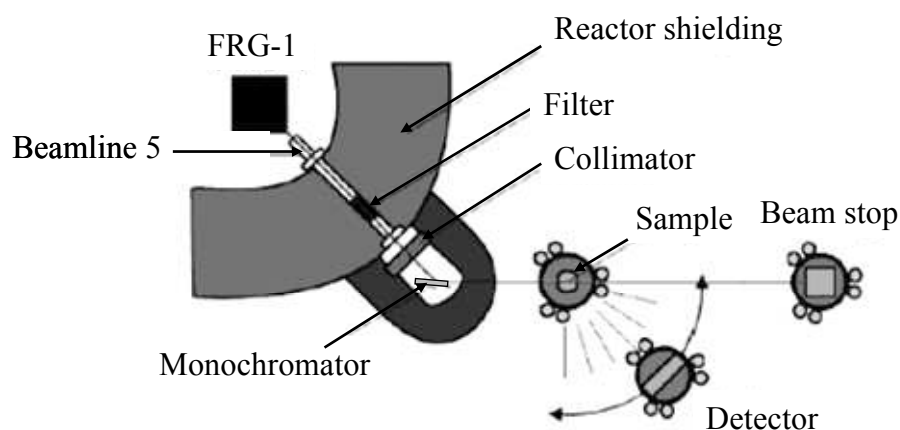


Figure 3.13: Instrument layout of TEX-2 installed at Helmholtz-Zentrum Geesthacht [147].

TEX-2 is a conventional neutron four-circle-diffractometer which has been optimized for texture investigations. The experimental details are listed in Table 3.7. It should be pointed out that the detector rotates according to 2θ of the measured reflection. Due to a limited beamtime, only 3 pole figures (10.0), (00.2) and (10.1) were measured in Ti-2.5Cu (SHT). To calculate the orientation distribution function (ODF), at least five pole figures should be measured. Therefore, monochromatic synchrotron radiation was applied as described in the next section.

Table 3.7: TEX-2 diffractometer parameters

Wavelength (Å)	1.332
Monochromator	Cu (111)
Detector	He-detector
Slit size (mm)	Primary slit: 22 x 22 Detector slit: 22 x 22
Rotation angle φ (°)	From 0 to 360
Tilting angle ψ (°)	From 0 to 90
Sample environment	Eulerian cradle

b. Bulk Texture Variation during Plastic Deformation using Monochromatic Synchrotron Radiation

The present study aimed at investigating of the texture variation during plastic deformation at ambient temperature by using synchrotron radiation. This led to understanding the deformation behavior at the surface after applying different mechanical surface treatments. To achieve that aim, a round tensile sample was machined with diameter of 5 mm and gauge length of 25 mm. The in situ tensile test was carried out at room temperature with strain rate of $6 \times 10^{-4} \text{ S}^{-1}$. The loading axis was parallel to the rolling direction. A universal testing machine (UTM), by which sample can be loaded up to 20 kN, was installed at Hasylab at DESY (Beamline W2) in Hamburg. The beamline with the UTM setup is schematically shown in Fig. 3.14.

Monochromatic incident beam has a size of $1 \times 1 \text{ mm}^2$ and a wavelength of 0.1262 Å . The diffracted beam, Debye–Scherrer cone, was registered on the area detector that was located perpendicular to the beam. The distance between the sample and the area detector was 1166 mm.

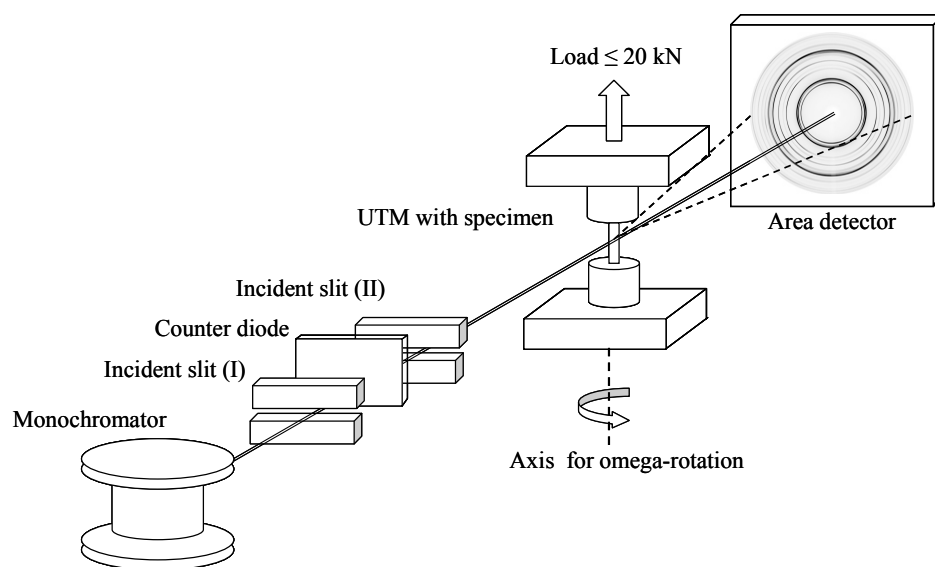


Figure 3.14: Schematic view of the beam line setup installed at Hasylab at DESY.

3.8 Phase Analysis by Using Monochromatic Synchrotron Radiation

The phase analysis of Ti-54M and LCB was performed using synchrotron radiation at DESY in Hamburg (Beamline W2) with a fitted wavelength of 0.1262 \AA (98.25 keV) using the diffraction pattern of Zn powder. The distance between the sample and the area detector was 1166 mm. The results were obtained after fitting by MAUD (Material Analysis Using Diffraction) software [156]. It is a general diffraction/reflectivity analysis program mainly based on the Rietveld method to refine the diffraction spectra as explained in details elsewhere [157].

3.9 Synchrotron Radiation Micro-Computed Tomography (SR μ CT)

To investigate of the possibility of near-surface defects in Ti-2.5Cu after SP or BB, Synchrotron radiation micro-computed tomography (SR μ CT) was used. A comprehensive description of the SR μ CT instrument is given by [158]. The schematic layout of this instrument is shown in Fig. 3.15.

This technique not only generates spatial images as a basis for micro-structural analysis but they also allow a free selection of virtual cuts through the sample in any direction. The SR μ CT instrument was a μ CT-instrument of the Helmholtz-Zentrum Geesthacht at beamline W2 of HASYLAB at DESY in Hamburg.

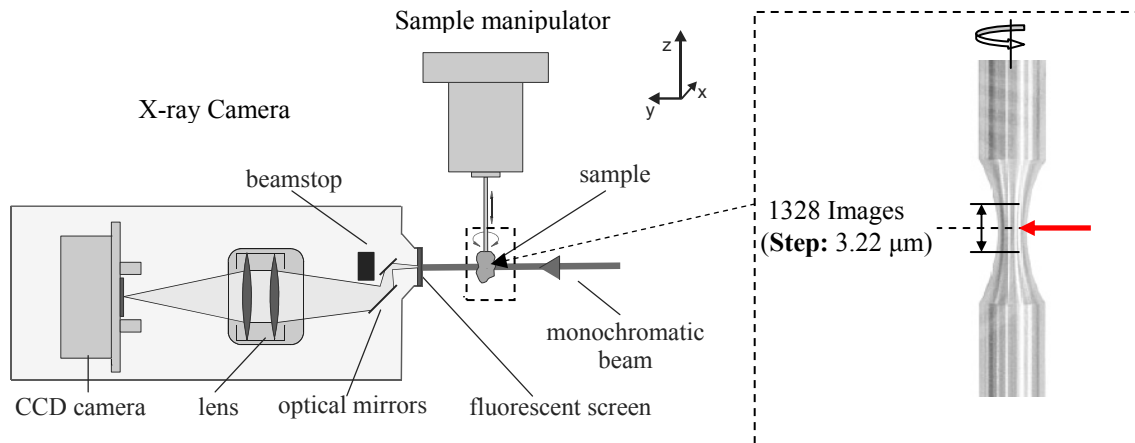


Figure 3.15: Schematic layout of the SR μ CT instrument installed at Hasylab at DESY.

This instrument consists of a 2D X-ray detector and a sample manipulator stage. The sample manipulator provides both the rotation and the lateral positioning of the sample. The incident X-rays are converted into visible light which then is projected onto a charge coupled device (CCD) camera by an optical lens system. The experimental parameters for the SR μ CT measurements are listed in Table 3.8.

Table 3.8: Experimental parameters for the SR μ CT - measurements

X-ray source	Synchrotron radiation
X-ray energy (keV)	50
Wavelength (Å)	0.248
Filter	Monochromator
Resolution (μm)	5.63
Rotation angle ($^\circ$)	0 - 180 with step size of 0.25°
Magnification	2.79
Radiographs	1328

3.10 Fatigue Testing

Fatigue testing was conducted on the electropolished references and mechanically surface treated samples using SincoTech[®] rotating-beam fatigue machine. All tests were performed in cantilever rotating beam loading ($R = -1$) in air with frequency of 50 Hz at room temperature. The ASTM fatigue samples were machined to an hour-glass shape with minimum gauge diameter of 3 mm as shown schematically in Fig. 3.16.

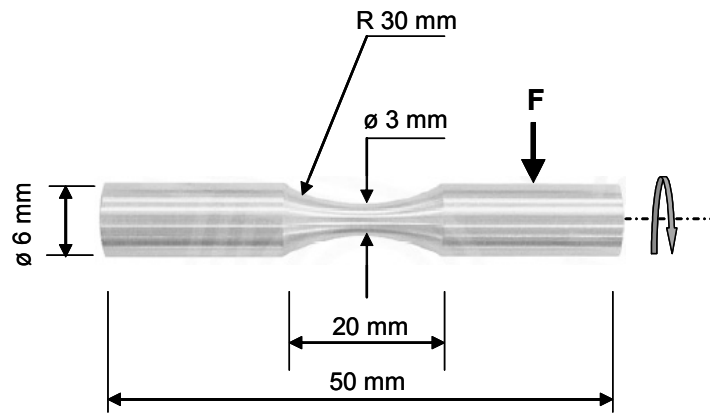


Figure 3.16: fatigue testing sample.

4 Results and Discussions

4.1 Introduction

The influence of surface layer properties such as work hardening, surface morphology and residual stress on the fatigue performance of Ti-2.5Cu, Ti-54M and LCB after various mechanical surface treatments are introduced and discussed in this chapter. Furthermore, the changes in the crystallographic textures in the surface treated Ti-2.5Cu is described.

4.2 Microstructures and Phase Analysis

The microstructures of Ti-2.5Cu after solid solution heat treatment (SHT), SHT followed by aging (SHT+A), Ti-54M and LCB are shown in Fig. 4.1a, b, c and d, respectively.

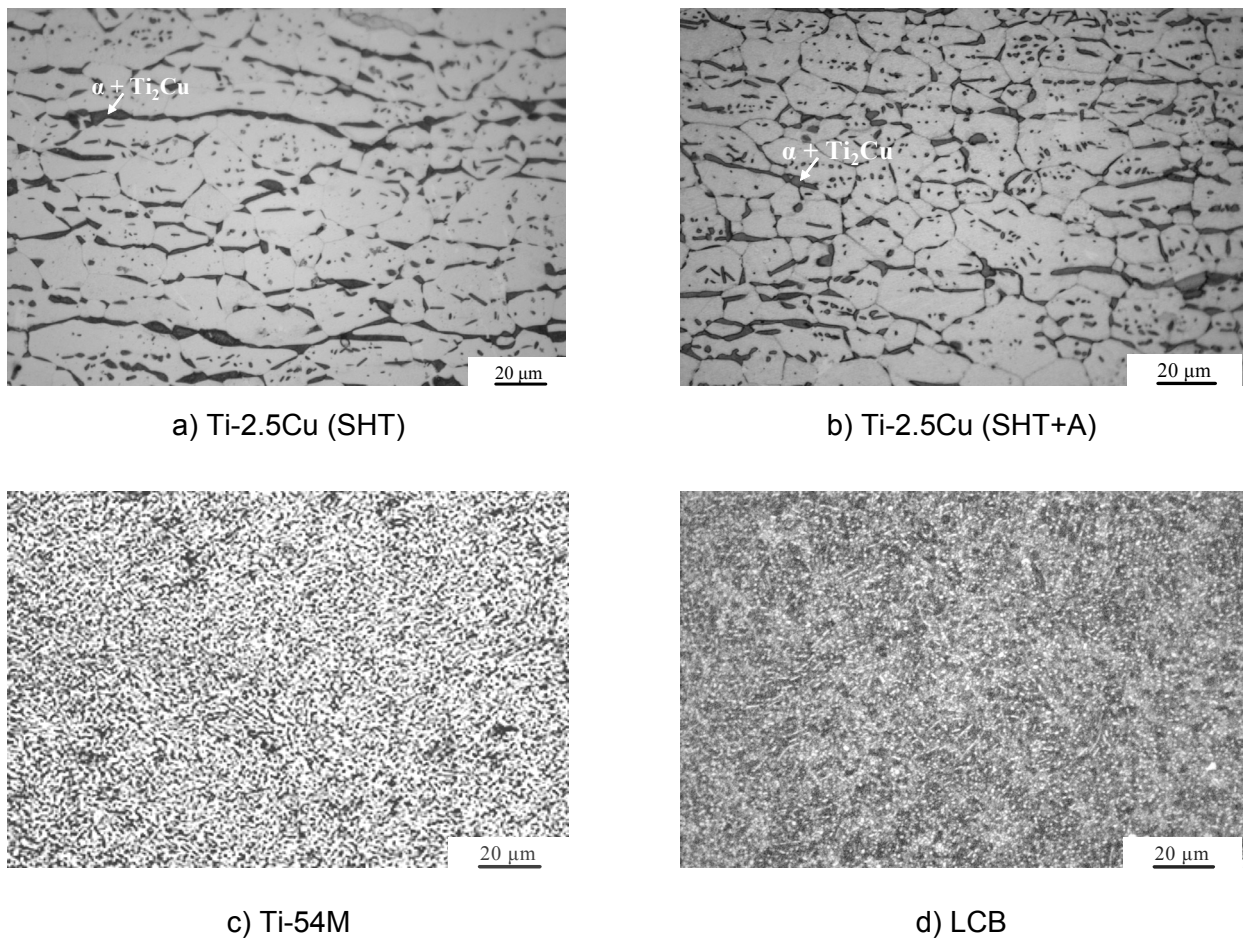


Figure 4.1: Microstructure of Ti-2.5Cu (SHT) (a), Ti-2.5Cu (SHT+A) (b), Ti-54M (c) and LCB (d) (SHT = solid solution heat treatment, A = aging).

It was observed that both microstructures of Ti-2.5Cu consist of α grains and stringers of the eutectoid component $\alpha + \text{Ti}_2\text{Cu}$ (dark phase). The microstructure of Ti-54M is fully equiaxed (EQ) with the equilibrium volume fraction of β -phase (dark phase) located at the triple-points of the α -grain boundaries. The equiaxed α -grain sizes in Ti-54M amount to about 3 μm (Fig. 4.1c). The thermo-mechanical treatment of LCB resulted in equiaxed primary α -phase (light phase) with a size of 2 μm located at the grain boundary triple points (indicated by the arrows in Fig. 4.2) of the β -grains (dark phase). During final heat treatment, fine secondary α -particles were precipitated out from the β -matrix leading to marked age-hardening. These secondary α -particles can only be seen by transmission electron microscopy (TEM) due to the small size as shown in Fig. 4.2 [159].

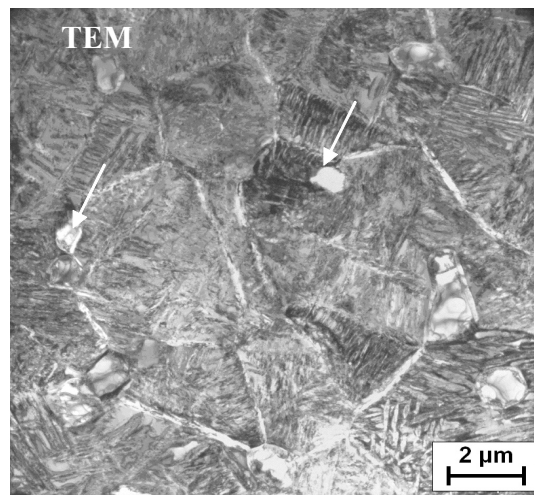


Figure 4.2: TEM image of LCB [159].

By using synchrotron radiation, the volume and weight fractions as well as the lattice constants of α - and β -phases in Ti-54M and LCB were evaluated and listed in Table 4.1..

Table 4.1: Fitting parameters of Ti-54M and LCB using pole figure data.

Phase	Model Parameter	Ti-54M	LCB
α -Phase	Volume Fraction %	84.2	15.7
	Weight Fraction %	83.4	15.0
	Lattice Constant \AA	a = 2.93467 c = 4.68544	a = 2.94980 c = 4.68915
β -Phase	Volume Fraction %	15.8	84.3
	Weight Fraction %	16.6	85.0
	Lattice Constant \AA	a = 3.20586	a = 3.22406

The Debye-Scherrer rings of Ti-54M (Fig. 4.3a) and LCB (Fig. 4.3c) clearly show the presence of crystallographic texture. Therefore, sum diffraction spectra of Ti-54M (Fig. 4.3b) and LCB (Fig. 4.3d) using pole figure data (with sample rotation) were calculated and fitted to overcome the texture influence.

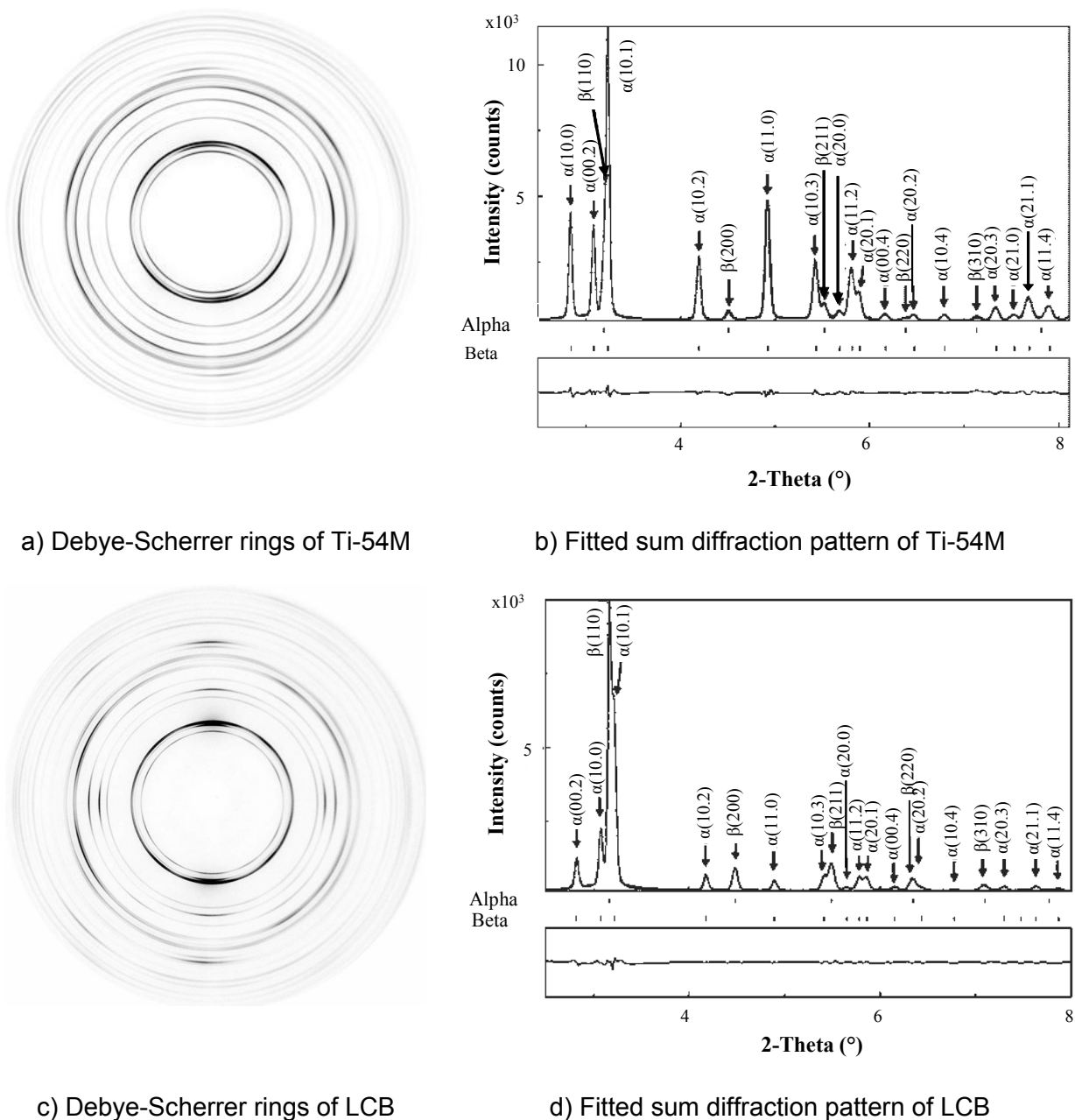


Figure 4.3: Debye-Scherrer rings of Ti-54M (a) and LCB (c) obtained by monochromatic synchrotron radiation (98.25 keV) as well as sum diffraction pattern of Ti-54M (b) and LCB (d) fitted by MAUD software.

Due to different grain sizes, volume fractions of different phases and precipitations in these alloys, the tensile properties markedly differ as listed in Table 4.2. As seen, Ti-2.5Cu (SHT+A) shows more pronounced increase in modulus of elasticity (E), yield strength ($\sigma_{0.2}$),

Table 4.2: Tensile properties of Ti-2.5Cu, Ti-54M and LCB.

Alloy	E (GPa)	$\sigma_{0.2}$ (MPa)	UTS (MPa)	El (%)
Ti-2.5Cu (SHT)	105	510	615	28
Ti-2.5Cu (SHT+A)	110	685	770	16.4
Ti-54M	116	1145	1145	12.6
LCB	113	1258	1295	14.7

ultimate tensile stress (UTS) compared to Ti-2.5Cu (SHT) due to the precipitation hardening influence of Ti_2Cu . In contrast, the ductility decreased after aging. Due to the retained β -phase and fine grains in Ti-54M after aging, $\sigma_{0.2}$ and UTS are greater than those of Ti-2.5Cu. While the fine secondary α -particles in LCB cause the higher values of $\sigma_{0.2}$ and UTS compared to Ti-54M. The tensile elongation is also high due to the fine β -phase dimensions.

4.3 Surface Morphology

The surface roughness (Rz) after performing various surface treatments on Ti-2.5Cu was determined and compared with the electropolished (EP) reference sample (Fig. 4.4).

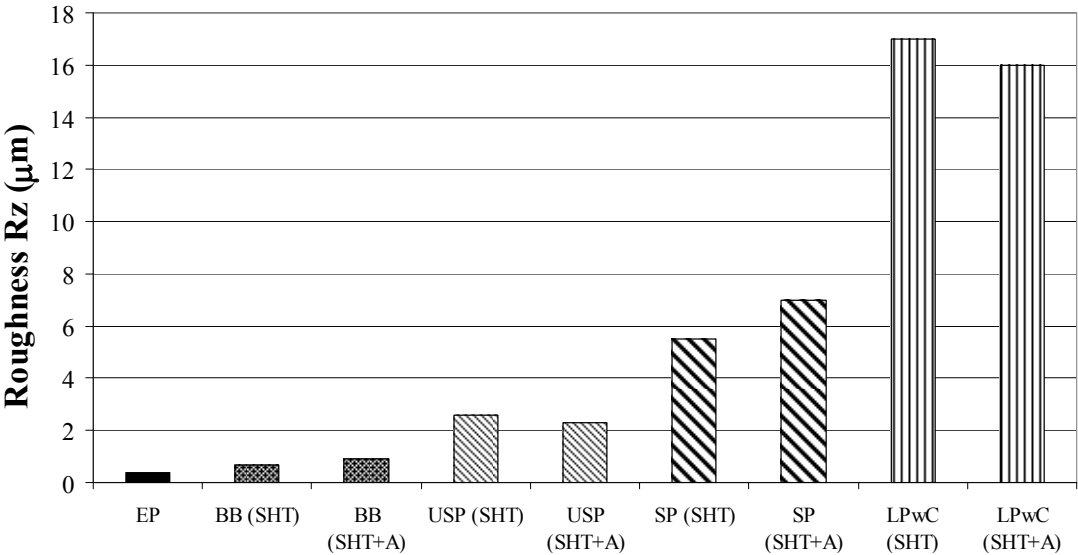


Figure 4.4: Surface roughness after various surface treatments in Ti-2.5Cu.

As seen in Fig. 4.4, the surface roughness of shot peened Ti-2.5Cu is much higher than that of the EP reference, while a remarkable improvement on the surface roughness was observed after BB compared to that after SP. Figure 4.5 illustrates an example of SEM images of the Ti-2.5Cu (SHT) surface showing its different responses to BB (Fig. 4.5a), SP (Fig. 4.5b), USP

(Fig. 4.5c) and LPwC (Fig. 4.5d). Obviously, the surface roughness after USP became smoother than that after SP. The reason of this result was considered that the balls in the case of USP are set into a random motion inside a component-specific peening chamber to act on the component, while the shots stream is nearly perpendicular to the surface in the case of SP. Therefore, the influence of the shot velocity on the indent depth or roughness is more significant in SP compared to that in USP. Furthermore, the bearing balls used for USP have higher spherical accuracy and smoother surface than the shots used in SP process.

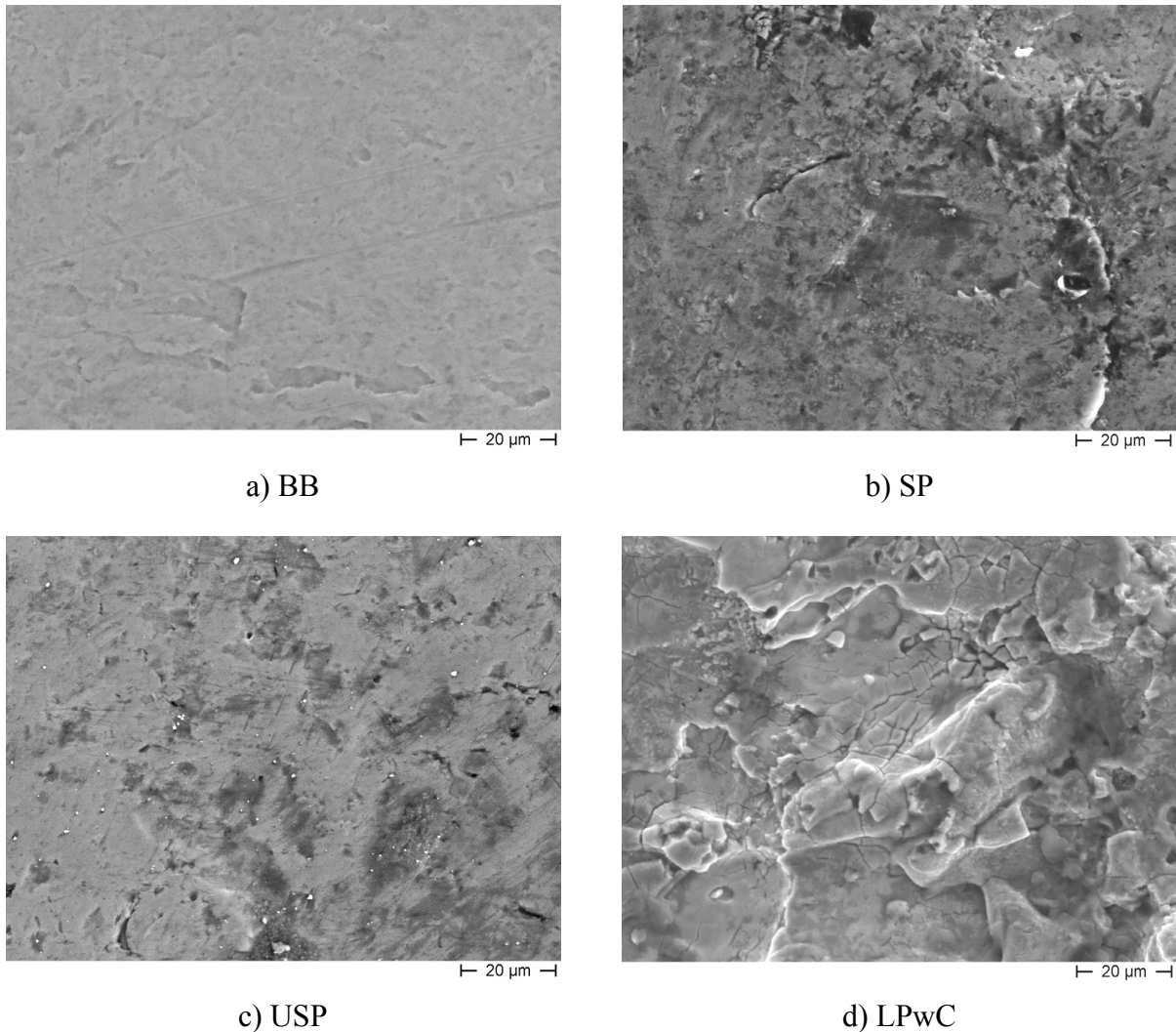


Figure 4.5: SEM images of Ti-2.5Cu (SHT) surface after BB (a), SP (b), USP (c) and LPwC (d).

As mentioned previously, due to an increased interest in the past two decades in laser peening technology for aeronautic and automotive applications, a comparison among the surface layer properties of Ti-2.5Cu (SHT+A), Ti-54M and LCB after LPwC has been investigated. Surface vaporization was still induced by LPwC with much smaller power and short pulse duration compared to LSP [160]. This can result in resolidified droplets and craters leading to

very rough surfaces [161] (Fig. 4.5d). This is also the reason why no significant difference among the roughness values (R_z) in the different Ti-alloys was observed, as shown in Fig. 4.6, in spite of different tensile properties

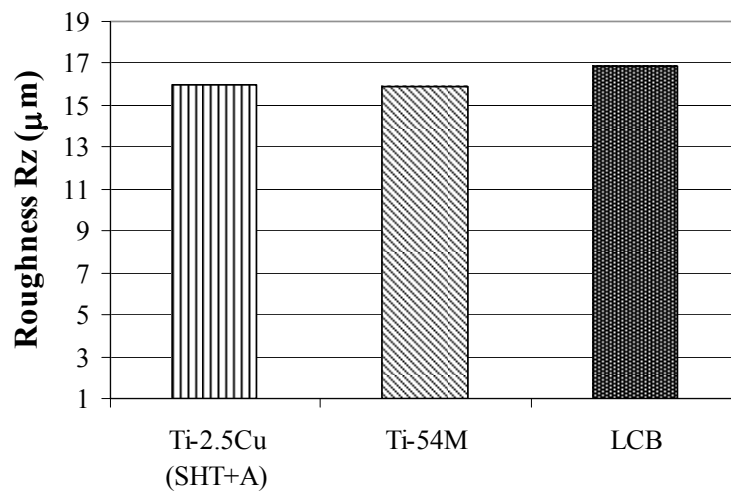


Figure 4.6: Surface roughness (R_z) of various Ti-alloys after LPwC.

Results revealed that microcracks were developed at the surface during LPwC. The top surface of the samples slightly melts or evaporates (less than $1\ \mu\text{m}$ from the surface) through ablative interaction between the intense laser pulses and the surface. Therefore, the ablative product is ejected away from the surface; however some part of the product remains on the surface or a part of the product resolidifies through water cooling and piles on the surface. The resolidified material may be oxide and brittle. During cooling down, it shrinks and some microcracks develop to relax the stress due to shrinkage as shown in Fig. 4.7. LPwC produced not only microcracks but also relatively more craters in Ti-54M surface (Fig. 4.7b) compared to those in Ti-2.5Cu and LCB surfaces. This could be explained by large coefficient of thermal expansion (CTE) of Al [162], whose composition is higher in Ti-54M (wt. 5%) than in LCB (wt. 1.5%).

This rougher surface associated with LPwC may lead to more significant deterioration in resistance to fatigue crack initiation and corresponding fatigue life than that with the other treatments. Nevertheless, this feature of LPwC could achieve more favourable interaction between the implant and biological tissues compared to, for example, BB or USP.

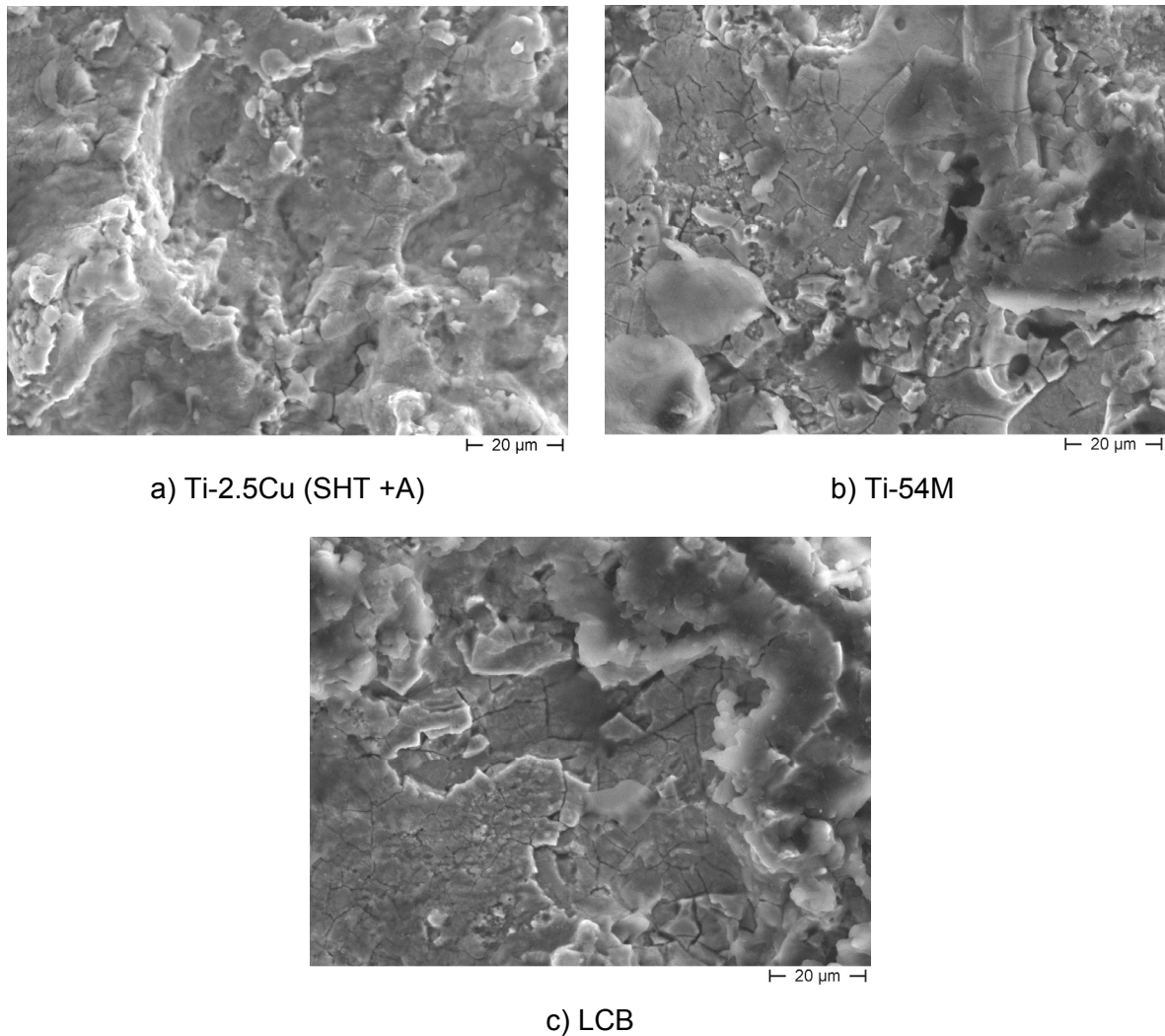


Figure 4.7: SEM surface images of (a) Ti-2.5Cu (SHT+A), (b) Ti-54M and (c) LCB after LPwC.

4.4 Microhardness-Depth Profiles

The microhardness-depth distributions of Ti-2.5Cu after various mechanical surface treatments are shown in Fig. 4.8. It was found that the bulk hardness in Ti-2.5Cu (SHT) is 250 HV0.1 approximately (Fig. 4.8a), while the bulk hardness in Ti-2.5Cu (SHT+A) is about 320 HV0.1 (Fig. 4.8b). This increase of the hardness is explained by the precipitation hardening influence. The maximum microhardness induced by SP, BB, LPwC and USP was observed at the surface which gradually decreased in the near-surface regions as shown in Fig. 4.8a and Fig. 4.8b. In both conditions of the heat treatments, it was found that the repeated dimpling at the surface by SP to achieve uniform surface coverage resulted in the highest cold worked layer or dislocation density at the surface.

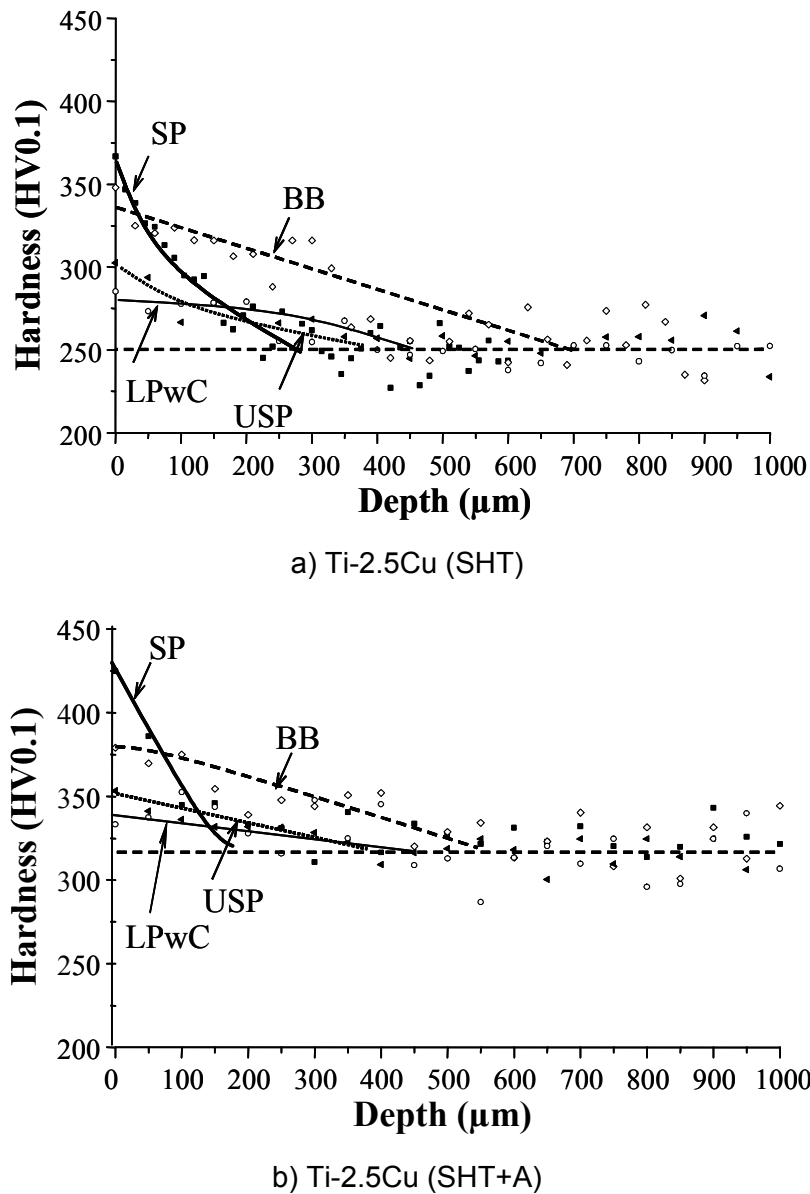


Figure 4.8: Microhardness-depth distribution in Ti-2.5Cu (SHT) (a) and Ti-2.5Cu (SHT+A) (b) after various surface treatments.

In contrast, LPwC produced the lowest microhardness at the surface, although each point on the surface was hit 16 times (laser spot area \times irradiation density) by the laser pulse. This is a result of the stress created by shock wave propagation rather than cold work as in SP. This lower magnitude of microhardness after LPwC supports the hardness results of LSP on hypoeutectoid steel [22]. In this study, laser beam with a small footprint (\varnothing 0.4 mm) and a lower power density ($5 \text{ GW}\cdot\text{cm}^{-2}$) generated a less planar pressure wave to propagate shallower into the sample producing plastic deformation with a depth of 0.45 and 0.6 mm from the treated surface in the case of SHT and SHT+A, respectively. In contrast, it was found in [25] that greater penetration depth of the plastically deformed layer (2 mm from the treated surface) was produced after LSP with larger footprint (3 x 3 mm) and higher power

density ($10 \text{ GW}\cdot\text{cm}^{-2}$) resulting in a higher pressure in 304 austenitic stainless steel. It should be also taken into account that the tensile properties of Ti-2.5Cu and 304 austenitic stainless steel are different when comparing the influence of LSP or LPwC parameters. This feature of LSP or LPwC leads to a thermal stability of residual stress close to the surface as explained later. It was observed that the microhardness induced by BB slightly decreased close to the surface (up to $100 \mu\text{m}$ in depth) compared to SP, while it increased in deeper region. This is due to less shearing between the ball and the sample surface while using lubricant as well as lower strain rate by BB.

The work hardening behavior close to the surface after these surface treatments was supported by determining FWHM. In the present study, the contribution of nanocrystalline grains to FWHM was ignored, since no significant changes of the grain size ($20 \mu\text{m}$) were observed close to the surface after the surface treatments. Figures 4.9a and 4.9b show the near-surface microstructures after SP and BB.

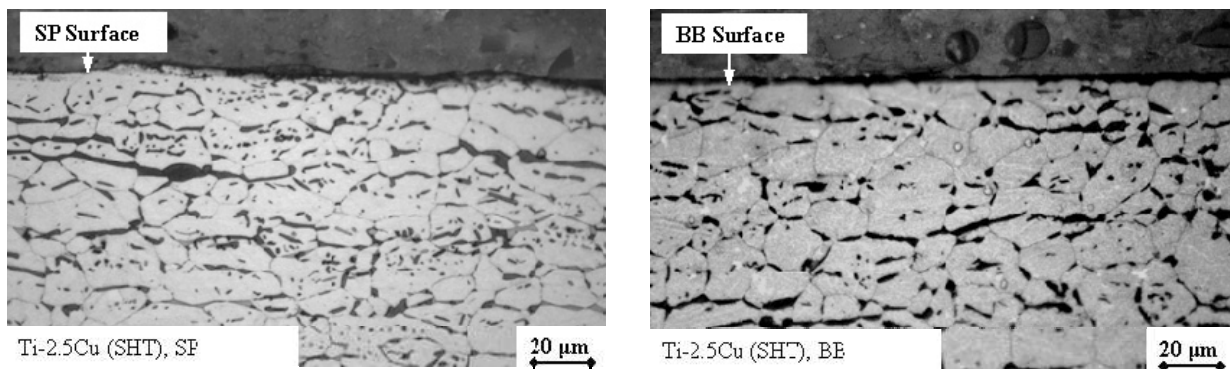
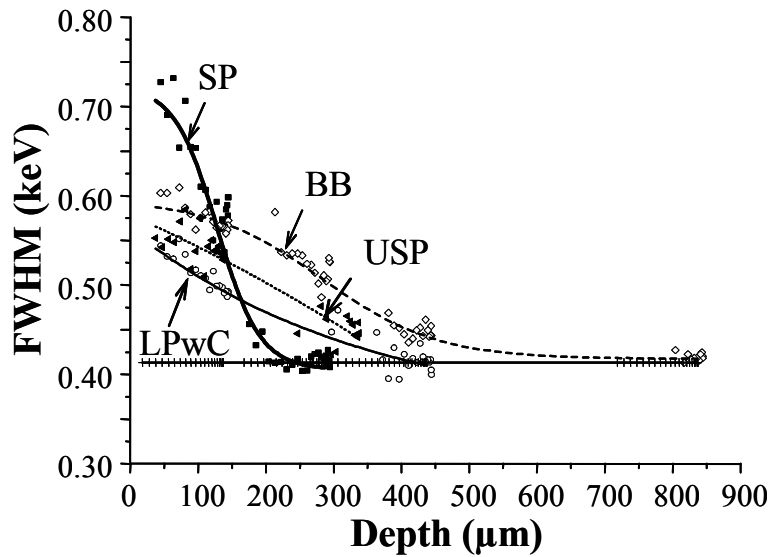


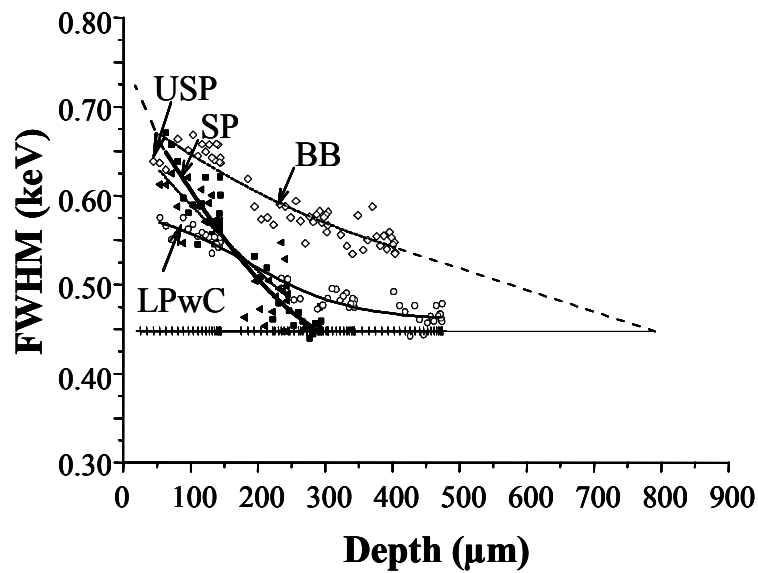
Figure 4.9: An example of near-surface microstructures after (a) SP or (b) BB in Ti-2.5Cu (SHT).

As seen in Fig. 4.10, the FWHM in the virgin region in Ti-2.5Cu (SHT+A) (Fig. 4.10b) is relatively larger than that in Ti-2.5Cu (SHT) (Fig. 4.10a). This increase of FWHM can be explained by the increase of Ti_2Cu precipitation as a structural defect. Furthermore, it was observed that the FWHM distributions close to the surface agree with the microhardness distribution. The reason of some slight differences in the penetration depth between the microhardness and FWHM could be explained by the data scattering of microhardness due to the existence of eutectoid components ($\alpha + \text{Ti}_2\text{Cu}$) in the grain boundaries.

The microhardness-depth profiles in Ti-2.5Cu (SHT+A), Ti-54M and LCB samples after LPwC are illustrated in Fig. 4.11. The variation of the hardness value and the plastic deformation depth in each alloy is explained by different tensile properties (Table 4.2).



a) Ti-2.5Cu (SHT)



b) Ti-2.5Cu (SHT+A)

Figure 4.10: FWHM-depth distribution in Ti-2.5Cu (SHT) (a) and Ti-2.5Cu (SHT+A) (b) after various surface treatments.

The highest bulk hardness and the smallest deformation depth in LCB (455 HV0.1) are attributed to relatively higher yield and tensile strengths compared to those in Ti-2.5Cu (SHT+A) and Ti-54M.

By normalizing the hardness values at the surface to the bulk values, it was found that the increases of work hardening by LPwC in the investigated alloys are similar.

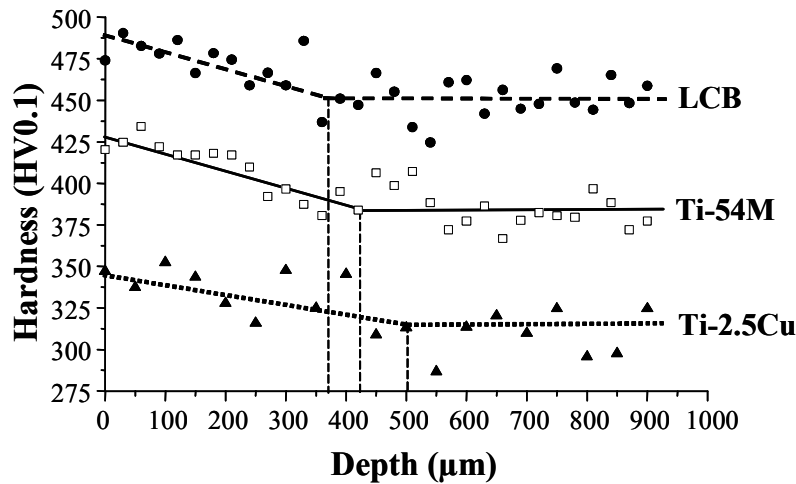


Figure 4.11: Microhardness-depth profiles in Ti-2.5Cu (SHT+A), Ti-54M and LCB after LPwC.

4.5 Residual Stress-Depth Profiles

4.5.1 Surface and Near-Surface Residual Stress by X-Ray Diffraction

The effect of LPwC on residual stress in Ti-2.5Cu was examined in the scanning direction of the laser beam (in the following X-direction) and perpendicular to the scanning direction (in the following Y-direction). Since LPwC was performed sequentially on both sample sides of 20 x 20 mm² areas, residual stress was determined on the first side treated by LPwC (in the following side-1) and on the second side (in the following side-2). The residual stress- depth profiles in different directions and sides are illustrated in Fig. 4.12.

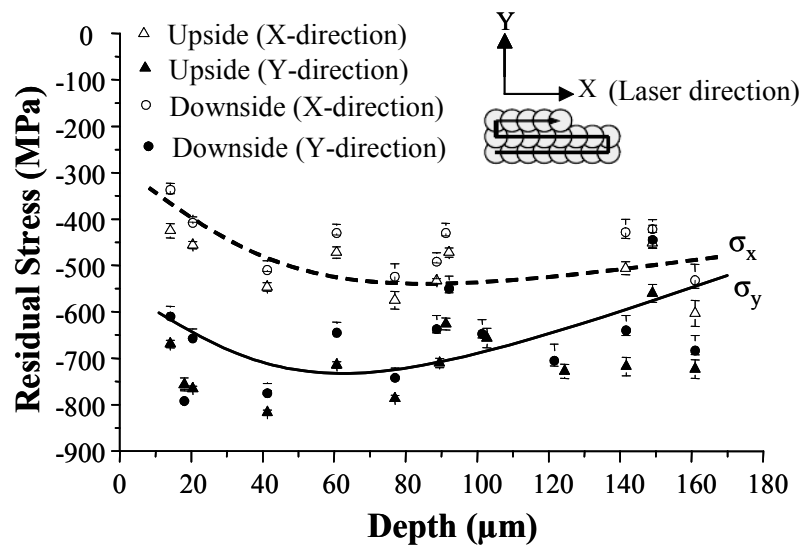


Figure 4.12: Residual stress distribution on both sides of Ti-2.5Cu (SHT+A) after LPwC.

The treatment being different in the X- and Y-directions resulted in that the magnitude of the residual stress in Y-direction (σ_y) after LPwC is larger than that in X-direction (σ_x) in the surface region which could be explained by a change of a local crystallographic texture. However, further investigation is needed to study the influence of some processing and/or material factors on the residual stress components. Furthermore, it was observed a slight difference between residual stress components on the side-1 and side-2. The residual stress generated on the side-1 is more compressive than that on the side-2. This might be a result of the influence of sample bending after LPwC on the side-1. Different residual stress components were also observed in Ti-2.5Cu (SHT) after applying BB (Fig. 4.13).

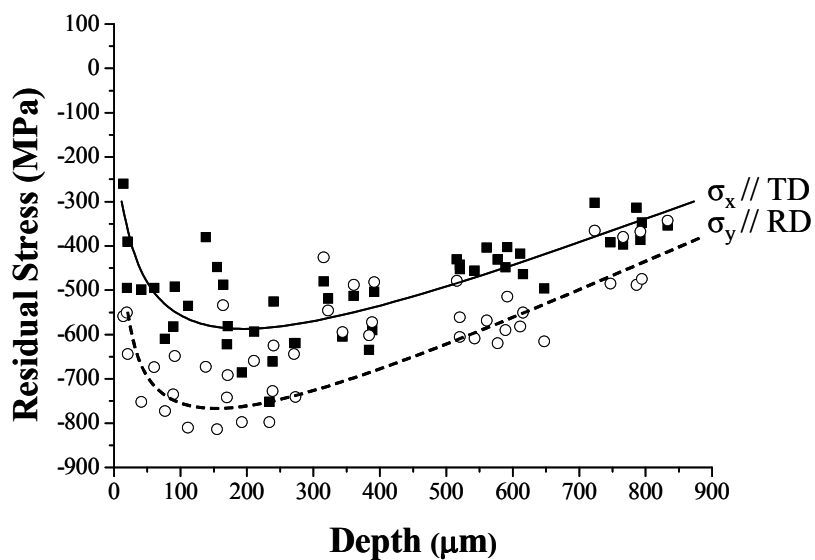


Figure 4.13: Anisotropy in the residual stress distribution in both faces of 20 x 20 mm² areas of Ti-2.5Cu (SHT) after BB. RD = Rolling direction and TD = Transverse direction

In contrast, it was observed no difference between the stress components σ_x and σ_y in Ti-2.5Cu after SP. In this chapter, the greater residual stress components (σ_y) generated in the surface layers of Ti-2.5Cu were compared and discussed.

Table 4.3: Residual stress component at surface (parallel to the rolling direction) after various surface treatments.

	Ti-2.5Cu (SHT)	Ti-2.5Cu (SHT+A)
	Residual stress (MPa)	Residual stress (MPa)
SP	-460	-465
USP	-415	-435
LPwC	-330	-390
BB	-665	-730

The residual stress values at the surface (determined by Lab-XRD) are listed in Table 4.3. On the other hand, the residual stress-depth distributions in the surface layers were determined by means of ED-XRD (see Section 3.6.2) as illustrated in Fig. 4.14. Obviously, both surface and maximum residual stresses in Ti-2.5Cu (SHT) is relatively lower than that in Ti-2.5Cu (SHT+A). This is explained by higher modulus of elasticity and yield strength of Ti-2.5Cu (SHT+A). This resulted in relatively larger potential maxima of the induced residual stress by plastic deformation.

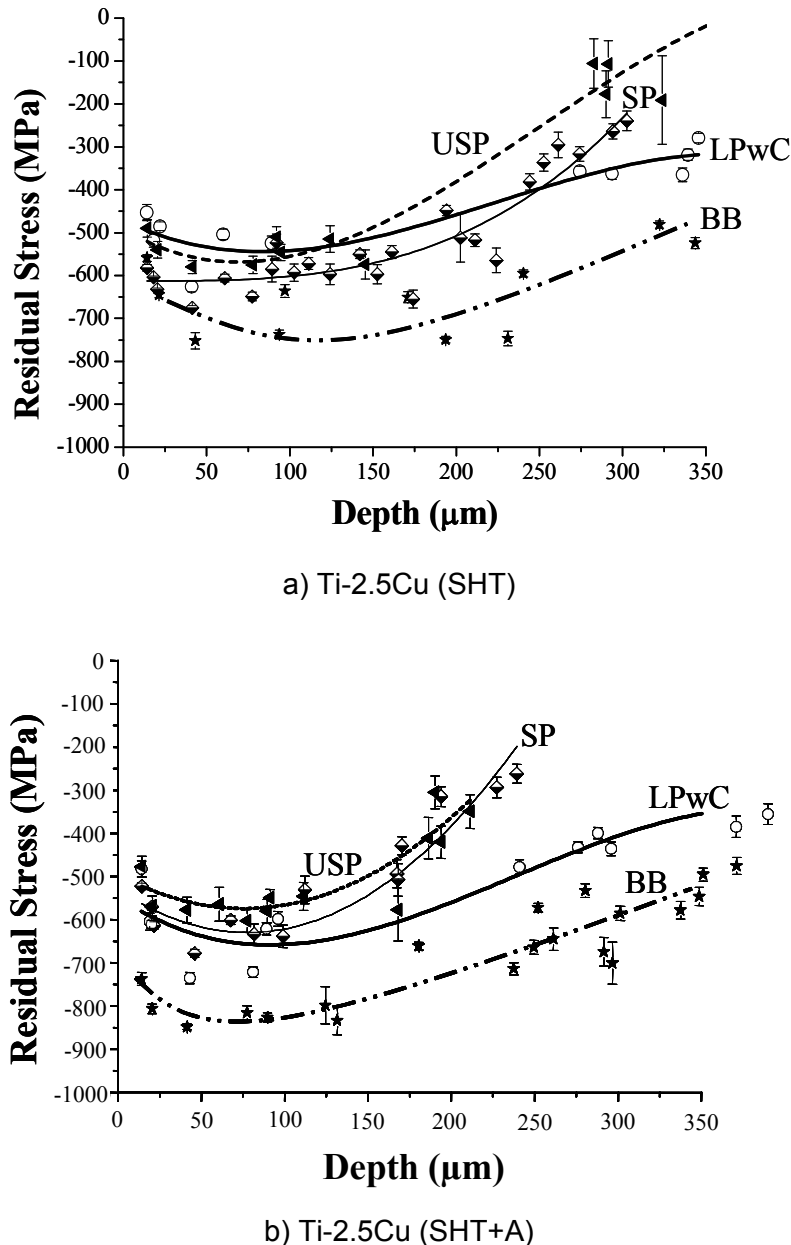


Figure 4.14: Residual Stress-depth distributions in Ti-2.5Cu (SHT) (a) and Ti-2.5Cu (SHT+A) (b) after various surface treatments.

It was observed that LPwC induced the lowest residual stress at the surface, while USP induced lower residual stress than SP and BB and higher than LPwC. This is attributed to the

magnitude of the cold work induced at the surface as shown in Fig. 4.8 and Fig. 4.10. Lower cold work resulted in lower flow stress and thus lower residual stress. However, it was found that BB produced higher residual stress at the surface compared to SP in both Ti-2.5Cu (SHT) and Ti-2.5Cu (SHT+A) despite the fact that BB produced lower work hardening than SP up to 100 μm approximately. This is opposed to the results shown later in this chapter, where SP or BB was applied only on one surface of a 10 mm thick sample. In contrast, both surfaces of the 5 mm thick sample were surface treated by SP or BB. Therefore, the higher compressive residual stress distribution (as induced by BB) in one side could influence on the residual stress state in the other side by generating relatively higher balancing tensile residual stress and severe elastic bending [28]. Consequently, neutron diffraction was used to determine the balancing residual stress as described later. In addition, changes of the crystallographic texture close to the surface after different surface treatments may also influence on the elastic anisotropy and elastic lattice strain [163–166].

In the present work, the residual stress component σ_y induced in the α -phase on the side-1 of Ti-2.5Cu, Ti-54M and LCB are compared as shown in Fig. 4.15.

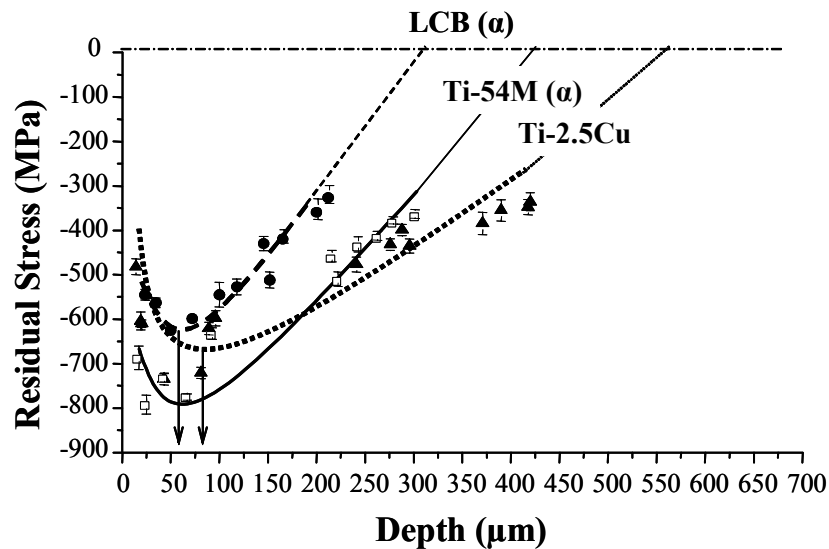


Figure 4.15: Residual stress-depth profiles in α -phase of Ti-2.5Cu, Ti-54M and LCB after LPwC in Y-direction.

The difference of the residual stresses among these alloys is explained by the difference in the yield strength. Ti-54M has larger yield strength than Ti-2.5Cu, while lower hardness and higher ductility in Ti-2.5Cu resulted in relatively deeper compressive layer compared to Ti-54M and LCB. Although the yield strength of LCB is higher than that of Ti-2.5Cu or Ti-54M, the residual stress is lower. This might be explained by smaller volume fraction of the α -phase

(about 15%) in LCB compared to that in Ti-54M (about 85%) as listed in Table 4.1. Therefore, the residual stress induced in the β -phase of LCB was also evaluated (Fig. 4.16)

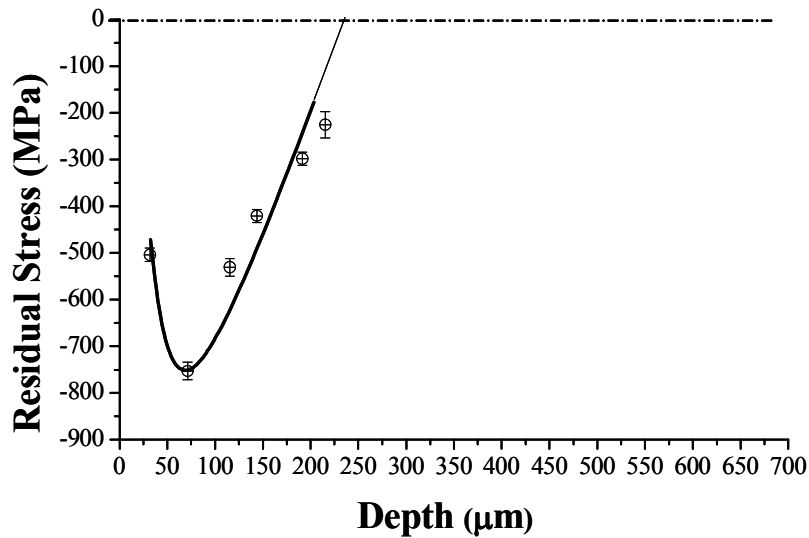


Figure 4.16: Residual stress-depth profile in β -phase LCB after LPwC in Y-direction.

and compared to that in the α -phase, while it was difficult to determine that in Ti-54M due to a small volume fraction and inadequate diffraction intensities to fit the β -phase reflections. Obviously, compressive residual stresses in the β -phase are markedly higher than in the α -phase. This can be explained by the presence of fine secondary α -particles in the β -matrix which are precipitated out during the final aging treatment. These hcp precipitates being incoherent to the bcc β -matrix not only lead to a homogenization of the slip distribution during plastic deformation but also stabilize the work hardening states of the β -microstructure. However, an intensive investigation is needed to emphasize the different responses of both phase under deformation and residual stresses.

Laser shock peening without any ablative layer or LPwC could lead to tensile stresses at the surface probably due to local melting. Therefore, the residual stress at the surface was determined by using Lab-XRD. The results revealed that the surface residual stresses are also compressive as listed in Table 4.4. This compressive stresses were generated due to a large number of laser hits (16 hits). The difference among these surface residual stresses is also explained by different local yield stresses at the surface.

Table 4.4: Residual stress (σ_y) at the surface of Ti-2.5Cu (SHT+A), Ti-54M and LCB

	Ti-2.5Cu (SHT+A)	Ti-54M	LCB
Surface residual stress (MPa)	-390	-650	-450

4.5.2 Residual Stress Distribution by Combining X-Ray and Neutron Diffraction

The residual stress-depth distributions in the Ti-2.5Cu (SHT) sample with a thickness of 10 mm after performing SP (Fig. 4.17a) and BB (Fig. 4.17b) only on one face were determined by combining ED-XRD and neutron diffraction.

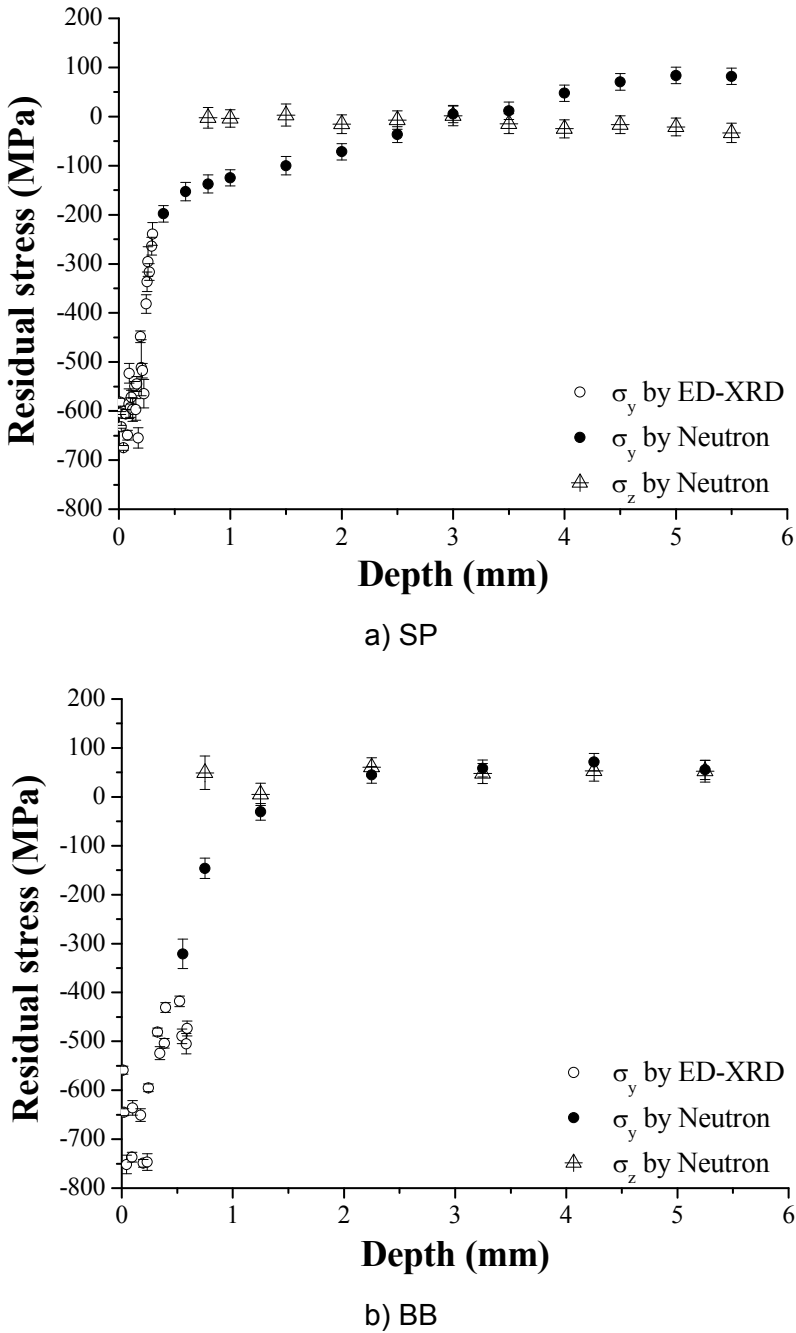


Figure 4.17: Residual Stress-depth distributions in Ti-2.5Cu (SHT) after SP (a) or BB (b).

Obviously, the in-plane residual stress distributions ($\sigma_y // RD$) after SP or BB are different. While the residual stress normal to the surface (σ_z) is constant within the depth and their

values are 0 MPa and 50 MPa in shot peened and ball-burnished samples, respectively. This is explained by means of a radial material flow after SP or BB inducing only σ_x and/or σ_y . However, it was found a small value of σ_z after BB. This could be explained by a relatively higher hydrostatic pressure of 300 bar normal to the surface. Apparently, the maximum residual stress in Ti-2.5Cu (SHT) after SP (-690 MPa) is lower than that after BB (-750 MPa). On the other hand, BB produced residual stress very close to the surface lower than SP. This is explained by different effects of SP or BB on the work hardening or dislocation density induced in different regions as illustrated in Fig. 4.8a and Fig. 4.10a. The most interesting residual stress (σ_y) values and their depths (τ) as well as corresponding improvements of the high cycle fatigue strength (HCF) [69,70] are summarized in Table 4.5.

Table 4.5: Summarization of residual stress values after SP and BB in Ti-2.5Cu (SHT).

	RS close to surface		Maximum RS		Zero-crossing		Tensile RS		Improvement of HCF % [69,70]
	σ_y [MPa]	τ [μm]	σ_y [MPa]	τ [μm]	σ_y [MPa]	τ [μm]	σ_y [MPa]	τ [μm]	
SP	-580	14	-690	90	0	3000	100	Const.	45
BB	-560	14	-750	190	0	1500	50	Const.	60

σ_y = RS= in-plane residual stress, τ = depth, Const. = constant, HCF = high cycle fatigue strength

Contrary to what is expected, the zero-crossing depth is about 3 mm after SP and 1.5 mm after BB. This is due to the influence of pre-stress with a zero-crossing depth of 3 mm (Fig. 4.18).

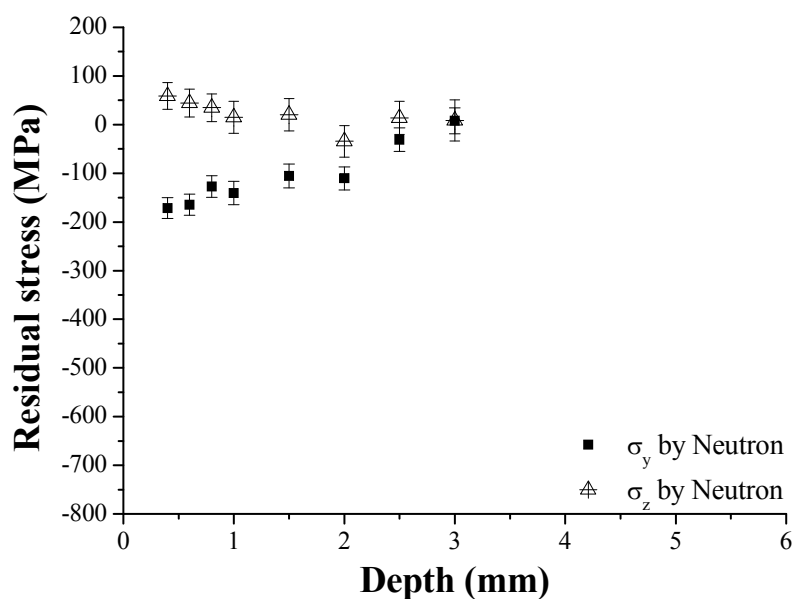


Figure 4.18: Pre-stress-depth distributions in Ti-2.5Cu (SHT).

The much higher compressive residual stress after BB close to the surface overcomes the existing pre-stress and the zero-crossing depth shifts from 3 mm to 1.5 mm to get the balancing tensile stress. It can be temporarily concluded that the maximum compressive residual stress and its depth could play more significant role to improve HCF performance than that the magnitude of zero-crossing depth. Furthermore, the balancing tensile residual stresses are about 100 MPa and 50 MPa after SP and BB, respectively. It may be argued that the observed transition in fatigue crack nucleation site from surface to subsurface in mechanically surface treated conditions is a result of the presence of a high tensile residual stress at a location below the sample surface [47].

In the previous results, three main limitations should be addressed. Firstly, SP or BB was performed only on one face of the quadrangular samples, whereas these processes are usually applied on round or on both sides of fatigue test samples to avoid asymmetric residual stress distribution and accordingly bending influence as occurred in a thin sample. Secondly, the residual stress in the surface layer was determined by removing some layers by electro-polishing process resulting in a release of macro-residual stresses. Thirdly, pre-residual stress state has a pronounced influence on the residual stress distributions. This could lead to an insufficient interpretation of the role of residual stress distribution in the fatigue performance, particularly in the core region with the balancing tensile residual stress. Therefore, one of the aims of the present study was at accurately determining both compressive and balancing tensile residual stresses through the sample thickness of 5 mm.

Due to a non-stable microstructure of Ti-2.5Cu (SHT) at elevated temperature, a stress relief treatment could change the microstructure and therefore could induce additional residual stresses. Thus, the residual stress depth-profiles were also examined in Ti-2.5Cu (SHT+A) after SP and BB. It should be pointed out that the microstructure of Ti-2.5Cu (SHT+A) are thermally stable after carrying out double aging. Consequently, it was essential to compare the previous residual stress distributions with the residual stress distributions in Ti-2.5Cu (SHT) and Ti-2.5Cu (SHT+A) after applying SP and BB in both faces with an area of 20 x 20 mm² and a thickness of 5 mm as shown in Fig. 4.19. These stress distributions through the thickness were non-destructively determined by combining ED-XRD and neutron diffraction.

This result leads to understanding the fatigue behavior in both high- and low-cycle regimes under different loading conditions. It is well known that rotating beam loading results in a stress gradient in radial direction of a round sample. Therefore, the stress amplitude has a maximum on the sample surface and diminishes towards the sample axes, where the stress

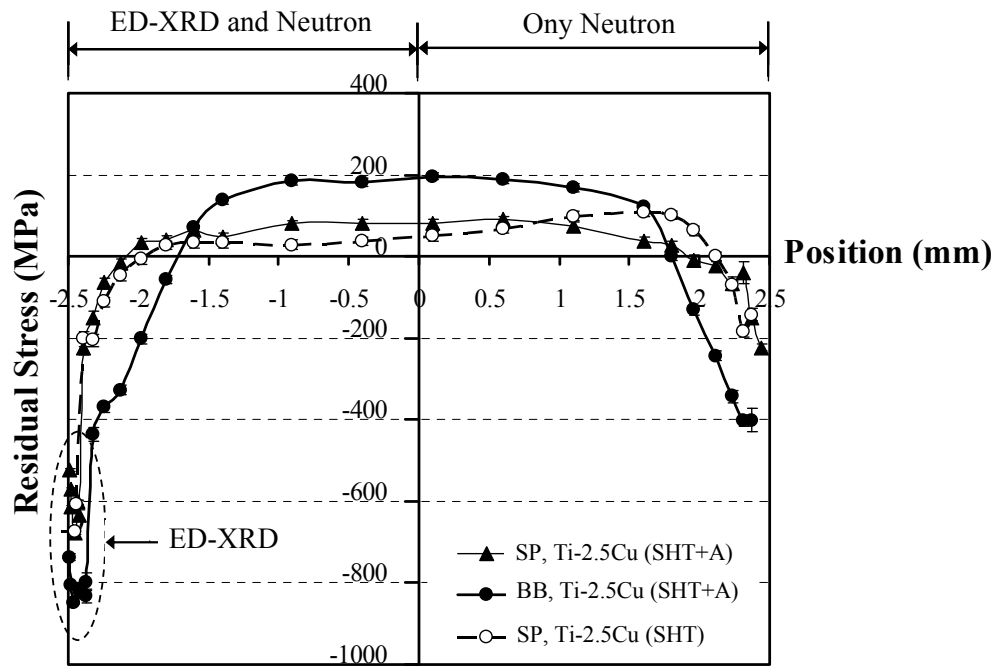


Figure 4.19: Residual stress-depth distributions through the thickness of Ti-2.5Cu (SHT) after SP and Ti-2.5Cu (SHT+A) after SP or BB.

amplitude becomes zero for stress ratio $R = -1$. Under these loading conditions, the tensile residual stresses (far below the surface) might not be detrimental for the fatigue properties. On the other hand, an axial loading with a homogeneous stress distribution might lead to different results regarding to different balancing residual stress distributions.

The residual stress distribution was only determined in shot peened Ti-2.5Cu (SHT) due to a short beamtime. Obviously, the residual stress distribution in Ti-2.5Cu (SHT) after SP is asymmetric compared to that in Ti-2.5Cu (SHT+A) after SP or BB. This could be explained by the induced pre-residual stress due to inhomogeneous and fast cooling rate by water quenching. On the other hand, this pre-residual stress was relieved after aging.

It should pay attention that the stress balance was achieved for the samples by integrating the areas under the distributions for both ED-XRD and neutron values. On the other hand, no stress balance was observed by using only neutron values. This can give an indication that this measurement needs a combination of ED-XRD (up to 130 μm in depth from the surface) and neutron diffraction which works accurately in relatively deeper region ($> 100 \mu\text{m}$ in depth).

Some stress values and their depths that could have a role in enhancing the HCF performance of Ti-2.5Cu (SHT+A) are listed in Table 4.6.

Table 4.6: Summarization of residual stress values after SP and BB in Ti-2.5Cu (SHT+A).

	RS close to surface		Maximum compressive RS		Zero-crossing		Maximum tensile RS		Improvement of HCF % [70]
	σ_y [MPa]	τ [μm]	σ_y [MPa]	τ [μm]	σ_y [MPa]	τ [μm]	σ_y [MPa]	τ [μm]	
SP	-520	14	-680	45	0	400	90	2500	24
BB	-735	14	-850	85	0	750	200	2500	47

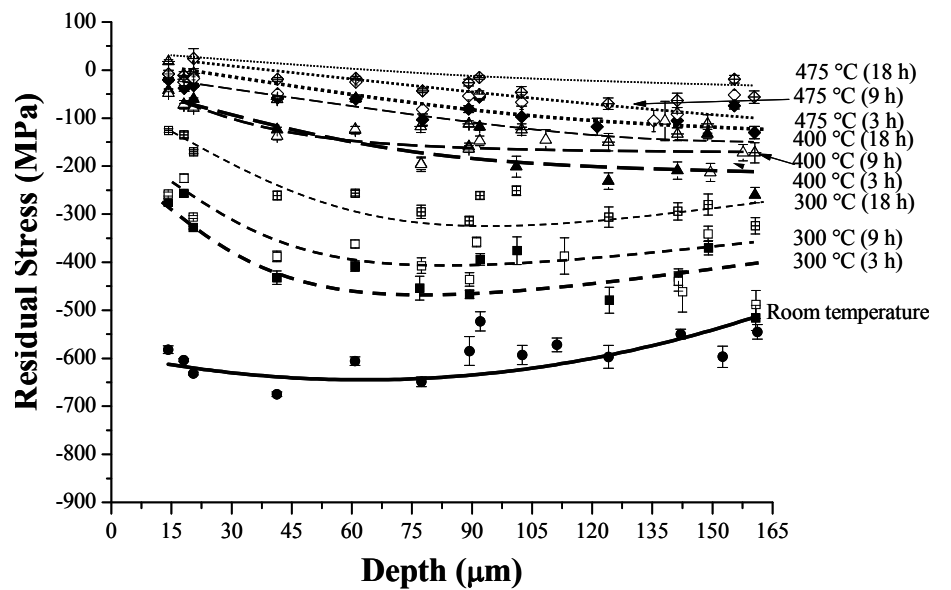
σ_y = RS = residual stress, τ = depth from surface, HCF = high cycle fatigue strength

Obviously, the compressive and balancing tensile residual stresses in Ti-2.5Cu (SHT+A) after BB are relatively higher than that after SP. The maximum compressive residual stress of -680 MPa after SP is significantly lower than that after BB (-850 MPa). Furthermore, the depths of compressive layers are about 400 μm and 750 μm after SP and BB, respectively. The greater amount and penetration depths of compressive residual stresses after BB as opposed to SP are thought to be the reason for the more pronounced improvement of the HCF strength after BB as mentioned in Table 4.6. The much greater penetration depth after BB can be seen in Fig. 4.8 where the microhardness profiles are plotted for both SP and BB. Furthermore, it was observed that the residual stress in Ti-2.5Cu (SHT+A) close to the surface after BB is higher than that after SP. This is opposed to the previous results, where SP or BB was applied only on one face of a 10 mm thick sample. Therefore, it can be concluded that the higher compressive residual stress distribution induced by BB on one side influenced on the residual stress state on the other side by generating relatively greater amount of balancing tensile residual stress (200 MPa) compared to the that (50 MPa) induced in Ti-2.5Cu (SHT) after performing BB on one side only.

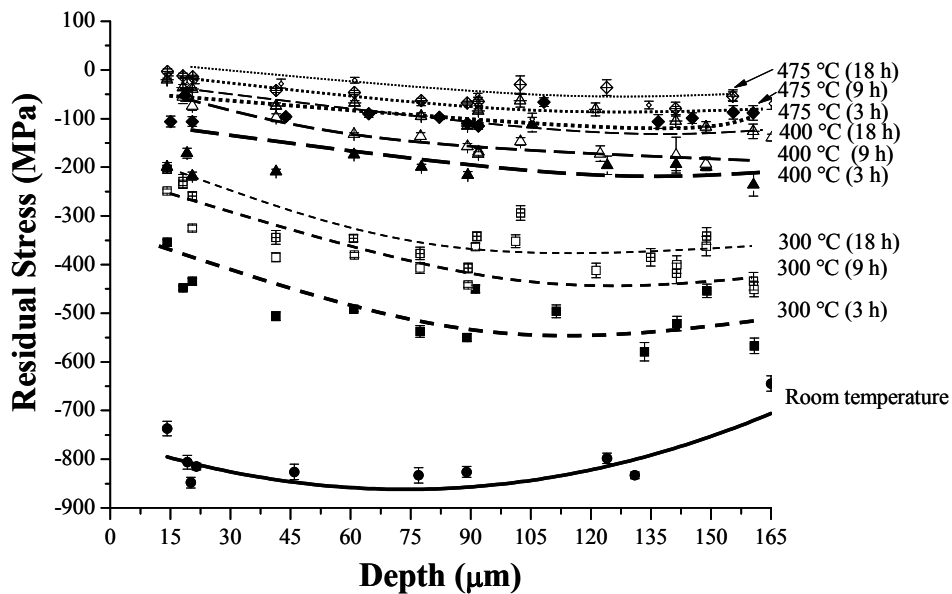
4.5.3 Thermal Stability of Residual Stress after Mechanical Surface Treatments

In the present work, it was essential to study the thermal stability of residual stresses as well as work hardening in, as an example, Ti-2.5Cu (SHT+A), since many engineering components are subjected to a high operating temperature. For example, the operating temperature of Ti-2.5Cu could reach to 300 – 350 °C. Therefore, the residual stress induced after surface treatments could be relieved reducing their beneficial influences on the fatigue performance. Ti-2.5Cu (SHT+A) was chosen rather than Ti-2.5Cu (SHT) in this investigation due to the microstructure stability after aging.

It was only focused on the study of the maximum compressive residual stress relaxation, as an example, after isothermal annealing at different temperatures (T) (300, 400 and 475 °C) for different times (t) (3, 9, and 18 hour). The residual stress-depth and FWHM-depth profiles in aged Ti-2.5Cu were only determined by ED-XRD as shown in Figs. 4.20 and 4.21, respectively, after SP or BB. While the incremental hole drilling method (IHD) was used to evaluate the residual stresses for all conditions.



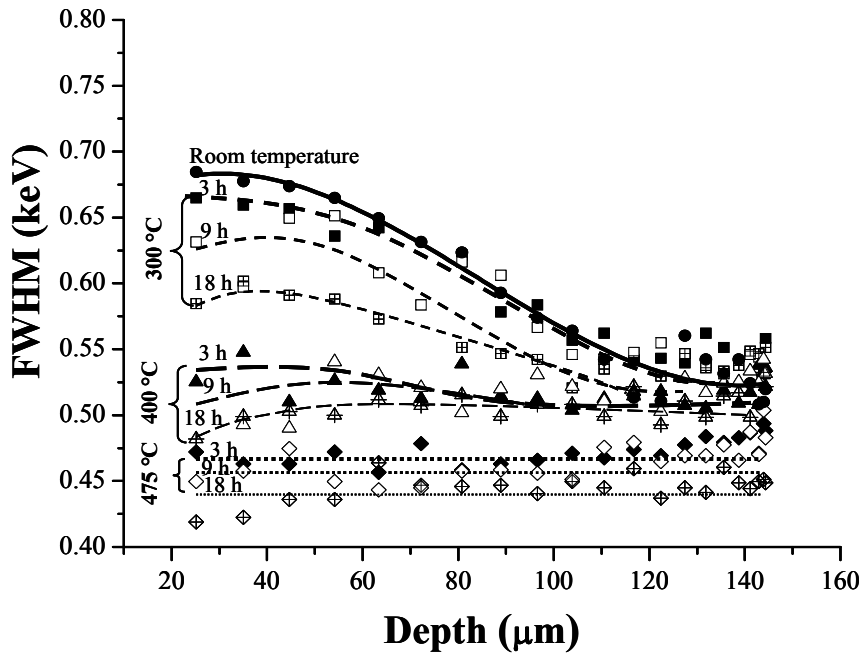
a) SP



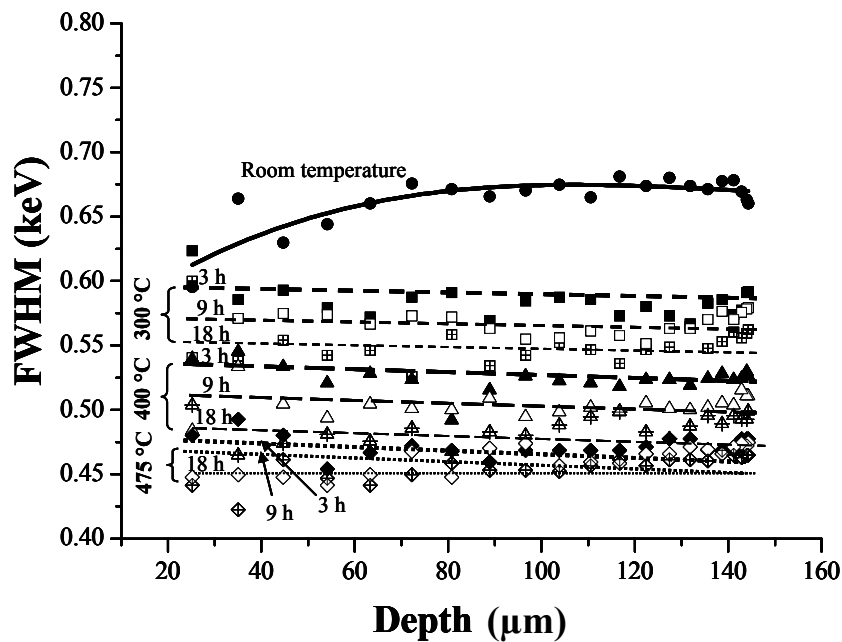
b) BB

Figure 4.20: Residual stress-depth distributions Ti-2.5Cu (SHT+A) after SP (a) and BB (b) after annealing at different temperatures and times (h=hours).

Obviously, in both cases of SP and BB the residual stresses decreased with increasing time and temperature. The residual stresses were completely relaxed at temperatures of 475 °C. This might result in a decrease of the fatigue strength at these temperatures even after mechanical surface treatments.



a) SP



b) BB

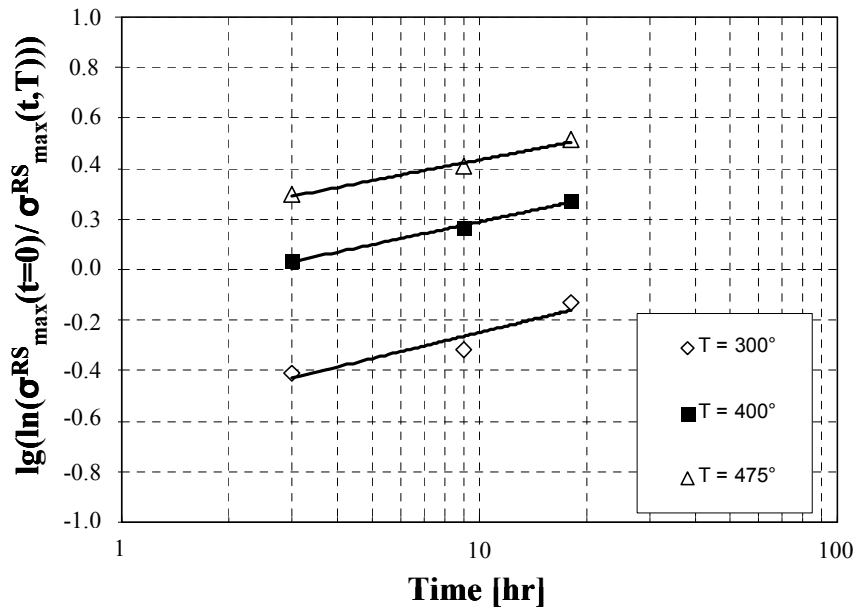
Figure 4.21: FWHM-depth distributions in Ti-2.5Cu (SHT+A) after SP (a) and BB (b) after annealing at different temperatures and times (h=hours).

The changes of work hardening or dislocation density in SP (Fig. 4.21a) and BB (Fig. 4.21b) Ti-2.5Cu (SHT+A) were also observed in the surface layers after annealing. This was qualitatively determined by means of the FWHM. In the case of BB, FWHM in RD was only presented, since it was found no a significant difference between FWHM in RD and TD. It is clearly seen in Fig. 4.21, the FWHM decreased with increasing time and temperature where recovery reduced the dislocation density. This is result of a reduction of stored energy by the removal or rearrangement of defects such as dislocations. It should be pointed out that IHD was used to determine residual stresses for all conditions in order to compare the results obtained by means of a Zener-Wert-Avrami function. Based on Eq. 2.9, to obtain the values of ΔH (activation enthalpy), m (exponent), C (velocity constant), the diagram of $\lg [\ln (\sigma^{\text{RS}}(t = 0) / \sigma^{\text{RS}}(t, T))]$ as the function of $\lg (t)$ was presented in Fig. 4.22. The calculated parameters are listed in Table 4.7.

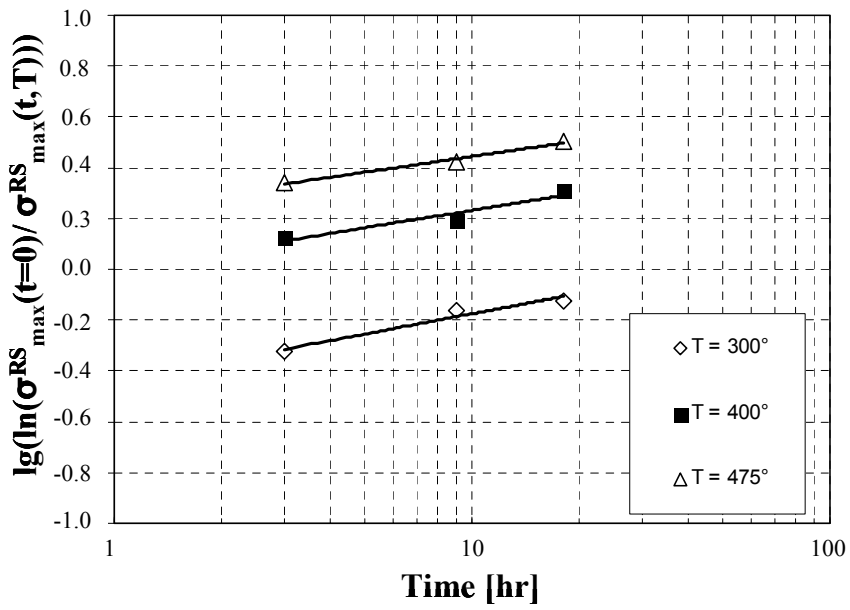
Table 4.7: Calculated parameters of Zener-Wert-Avrami function.

	m	ΔH (eV)	C (1/hr)	Microhardness at the surface (HV0.1)	Relaxation rate
SP	0.13	2.8	1.3×10^{20}	425	Fastest
BB	0,10	3.3	5.5×10^{24}	380	Faster
USP	0.08	3.9	1.3×10^{26}	355	Slower
LPwC	0.02	5.6	3.2×10^{26}	335	Slowest

Obviously, the fastest rate of maximum residual stress relaxation was observed in SP surface layer (Fig. 4.22a) up to 100 μm in depth, while the slowest rate was found in the surface layer after LPwC (Fig. 4.22d). Both magnitude and rate of relaxation of the compressive layer developed by the surface treatments were found to be highly dependent upon the degree of cold work induced during formation of the compressive layer (see Figs. 4.8 and 4.10). The more increase of the dislocation density, the more decrease of the creep stress in the surface layers. This feature LPwC may lead to relatively stable fatigue properties at elevated temperature. However, the amount of dislocation density and microstructure stability in the surface layer play more significant role for fatigue performance at elevated temperature than residual stress stability as reported in [29-30,167]. The results in the previous researches revealed that, at elevated test temperatures, the fatigue lifetime of the BB condition is higher than of the LSP condition due to more stable near-surface microstructures, e.g. nanocrystalline layers and higher dislocation densities.

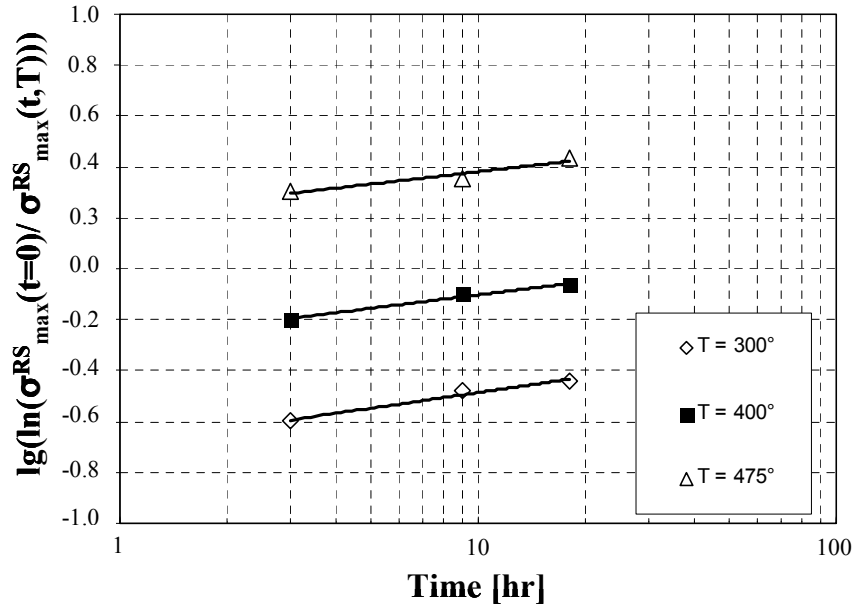


a) SP

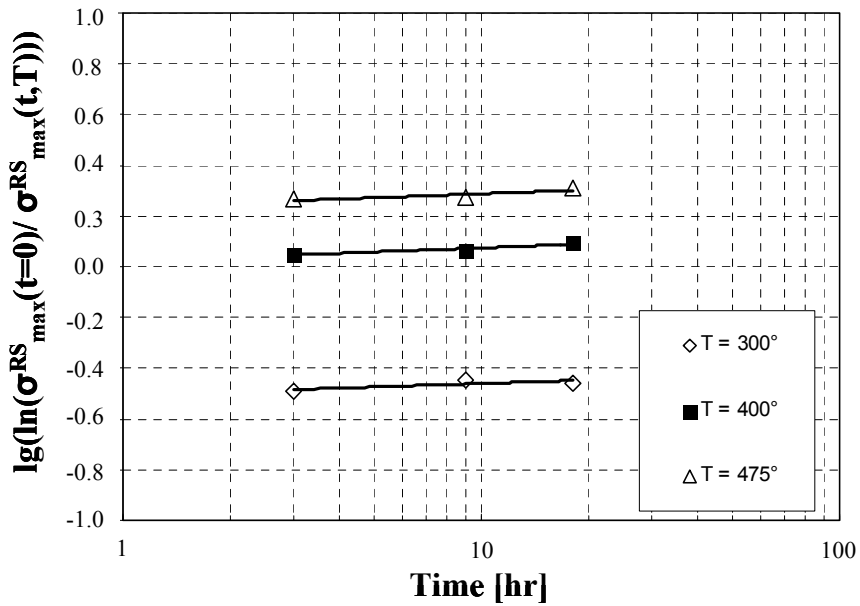


b) BB

Figure 4.22 (Part I): Plot $\lg [\ln (\sigma^{\text{RS}}(t=0) / \sigma^{\text{RS}}(T, t))]$ versus $\lg (t)$ of Ti-2.5Cu (SHT+A) after SP (a), BB (b).



c) USP

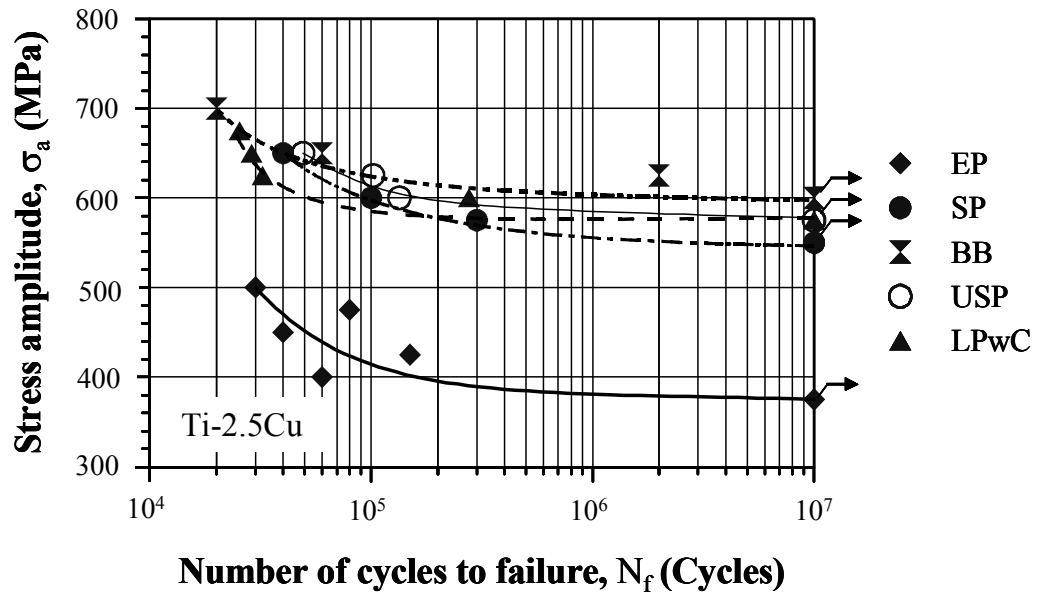


d) LPwC

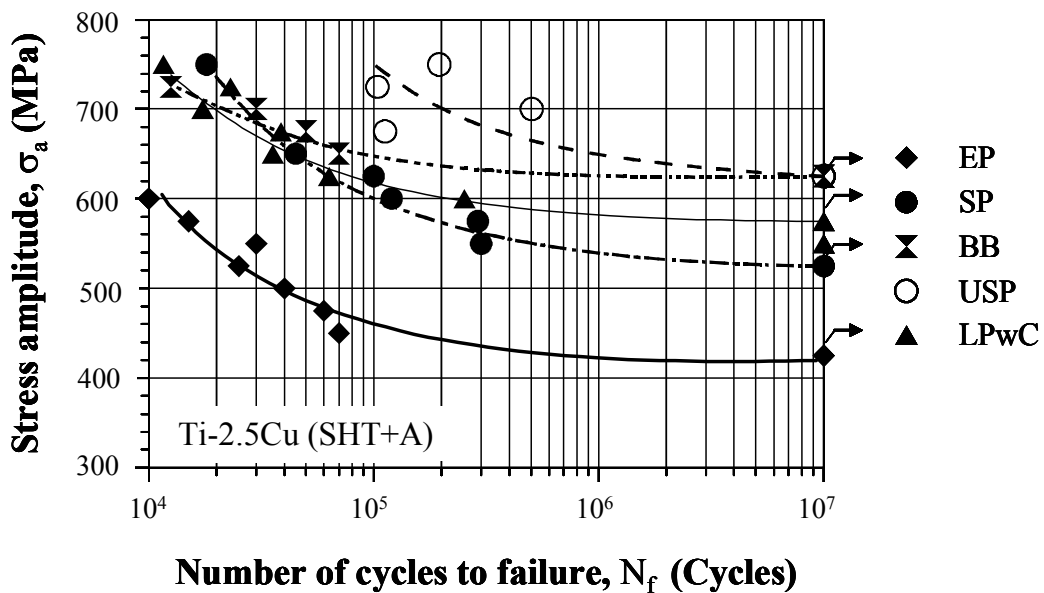
Figure 4.22 (Part II): Plot $\lg[\ln(\sigma^{\text{RS}}(t=0)/\sigma^{\text{RS}}(T,t))]$ versus $\lg(t)$ of Ti-2.5Cu (SHT+A) after USP (c) and LPwC (d).

4.6 High Cycle Fatigue Performance

The S-N curves in rotating beam loading in air of Ti-2.5Cu (SHT) and Ti-2.5Cu (SHT+A) are shown in Fig. 4.23a and Fig. 4.23b, respectively, comparing SP, BB, USP and LPwC conditions with the electropolished references (EP).



a) Ti-2.5Cu (SHT)



b) Ti-2.5Cu (SHT+A)

Figure 4.23: S-N curves ($R = -1$) of Ti-2.5Cu (SHT) (a) and Ti-2.5Cu (SHT+A) after various surface treatments.

It was observed that the high cycle fatigue (HCF) strength of EP Ti-2.5Cu (SHT+A) (425 MPa) is greater than that of EP Ti-2.5Cu (SHT) (375 MPa). This can be explained by higher

yield and tensile strength of Ti-2.5Cu (SHT+A). It is known that the resistance of fatigue crack initiation increases by increasing the yield stress that prevents macroscopic plastic deformation at the beginning of load controlled cycling [161-164].

The normalized stress amplitudes by the yield strength (σ_a/σ_y) of Ti-2.5Cu (SHT) are greater than those of Ti-2.5Cu (SHT+A) as plotted in Fig. 4.24. This behavior of Ti-2.5Cu (SHT+A) could be a result of stress concentrations in the α -grain boundaries due to a fine dispersion of the phase Ti_2Cu and loss of ductility after the double aging treatment. This can also provide locations for microcracks to nucleate under cyclic loading [168].

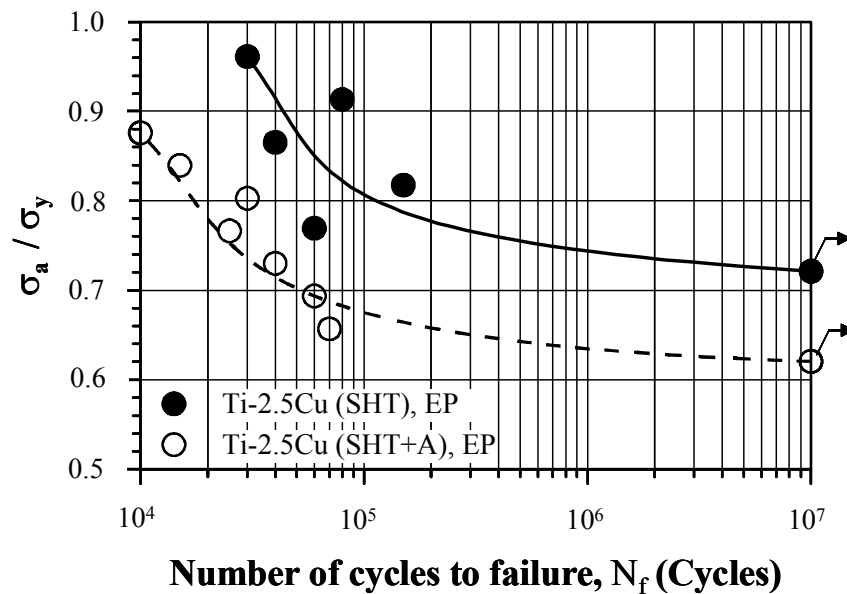


Figure 4.24: Normalized S-N curves ($R = -1$) of EP Ti-2.5Cu (SHT) and EP Ti-2.5Cu (SHT+A).

The HCF performance of EP references was improved by SP, BB, USP and LPwC as illustrated in Fig. 4.23. Apparently, the 10^7 cycles fatigue strength of Ti-2.5Cu (SHT) significantly increased from 375 MPa (EP) to 550 MPa after SP, 575 MPa after USP or LPwC and 600 MPa after BB (Fig. 4.23a). In addition, it increased from 425 MPa (EP) to 525 MPa after SP, 575 MPa after LPwC and 625 MPa after BB or USP (Fig. 4.23b). This beneficial effect of the surface treatments on the HCF performance was interpreted by surface morphology, work hardening, compressive residual stress in the surface layers and crack nucleation site (Fig. 4.25). The smaller surface roughness (Fig. 4.4), greater amount and penetration depth of compressive residual stress (Fig. 4.14) as well as the greater penetration depth of plastic deformation (Fig. 4.8 and Fig. 4.10) after BB as opposed to SP, USP and LPwC are thought to be the reason for the more pronounced improvement of the HCF strength.

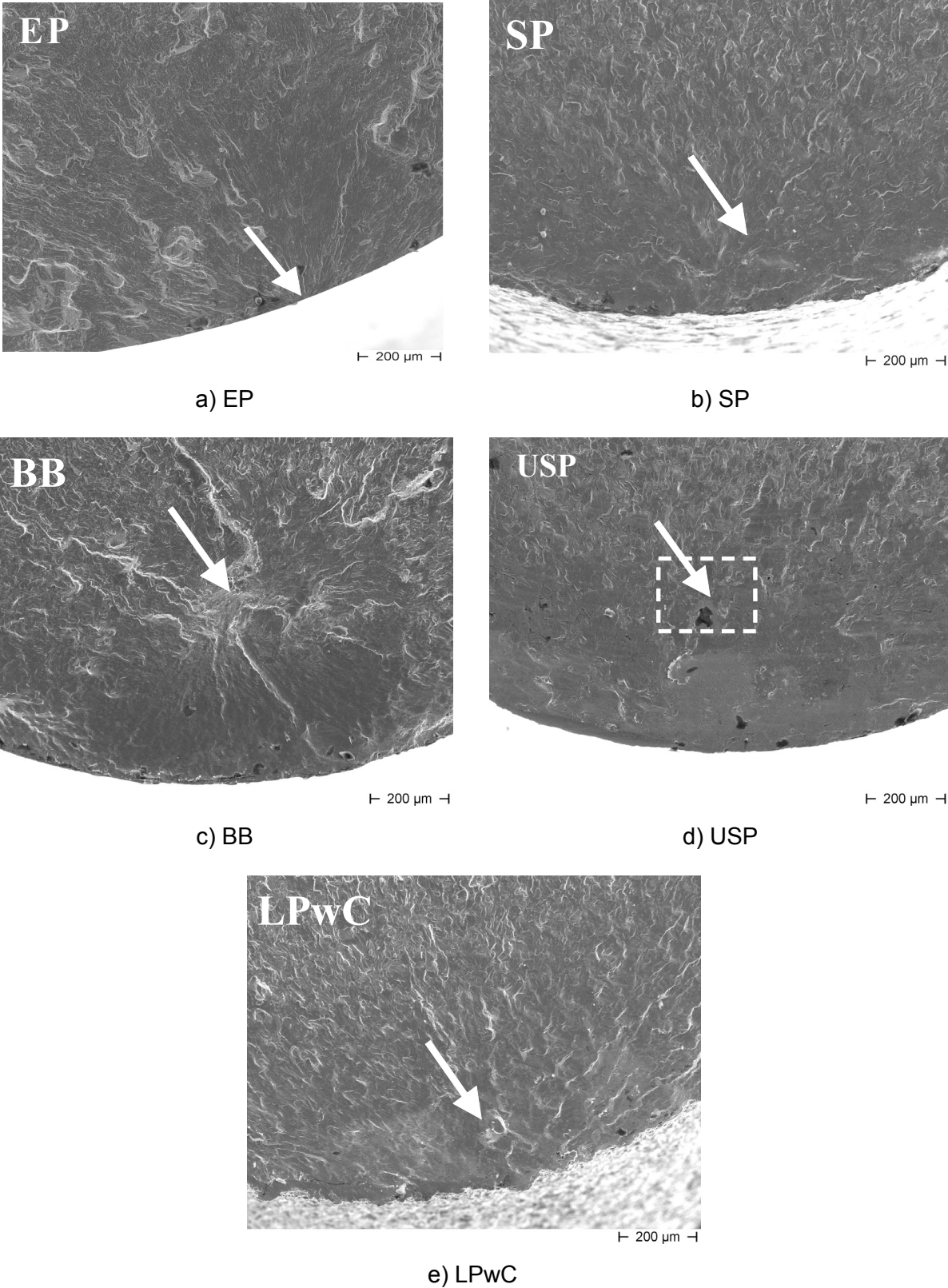


Figure 4.25: HCF crack nucleation sites in Ti-2.5Cu (SHT) after EP (a), SP (b), BB (c), USP (d) and LPwC (e).

Furthermore, this is related to the greater depth of the fatigue crack nucleation site of about 500 µm compared to 200 µm (SP and LPwC) underneath the surface of Ti-2.5Cu (SHT), as an

example, under quasi-vacuum condition (Fig. 4.25b,c and e), while the cracks nucleated at the surface of the reference sample (EP) (Fig. 4.25a). The crack nucleation site in Ti-2.5Cu (SHT) after USP is unclear. However, it could be located within the range of 300-500 μm in depth (dashed rectangular in Fig. 4.25d). This feature of USP beside a small surface roughness led to a pronounced fatigue performance compared to SP, although the compressive residual stress profiles are similar. Moreover, results revealed that better fatigue performance of Ti-2.5Cu (SHT) was obtained after USP (up to 10^5 cycles) compared to that after LPwC in spite of the greater amount and penetration depth of the compressive residual stress, while the 10^7 fatigue strengths are the same. This is due to greater depth of the fatigue nucleation site and relatively smoother surface in Ti-2.5Cu (SHT) after USP (Fig. 4.25d).

In contrast, it was observed no pronounced difference between fatigue behaviors after SP or BB in low cycle fatigue (LCF) regime of Ti-2.5Cu (SHT+A). This could be attributed to the influence of a combination of greater balancing tensile residual stresses (about 200 MPa, see Fig. 4.19) produced in the core region after BB and higher stress amplitudes on the fatigue crack behavior. In conclusion, balancing tensile residual stress could play more significant role in LCF behavior during rotating beam loading compared to that in high cycle fatigue performance. Further investigations are needed to emphasize the role of balancing tensile residual stresses during both axial and rotating beam loading.

Beside residual stresses, work hardening and surface morphology, the enhancement of fatigue performance might be attributed to the closure of surface or near-surface defects such as microcracks or voids due to manufacturing processes and/or heat treatments. Therefore, synchrotron radiation micro-computed tomography (SR μ CT) was used, as mentioned in section 3.9, in order to examine non-destructively whether there are any defects in the surface layer of EP Ti-2.5Cu (SHT) as a fatigue reference sample (Fig. 4.26). Due to the resolution of that instrument (5.63 μm), defects with size of $\sim 6 \mu\text{m}$ or larger can be detected. Result revealed that no manufacturing defects were observed with a size greater than 6 μm in the surface layer or in the bulk.

The compressive layer close to the surface induced by SP or BB must necessarily be balanced by the tensile layer in the near-surface. Microcracks might be nucleated in the transition region between compressive and tensile layer depending upon the value of tensile residual stress. If the balancing tensile stress exceeds the tensile strength of the material, microcracks might be occurred. An example of the 3-D tomography image of BB fatigue sample of Ti-2.5Cu (SHT) is shown in Fig. 4.27. Obviously, no microcracks were observed in the transition

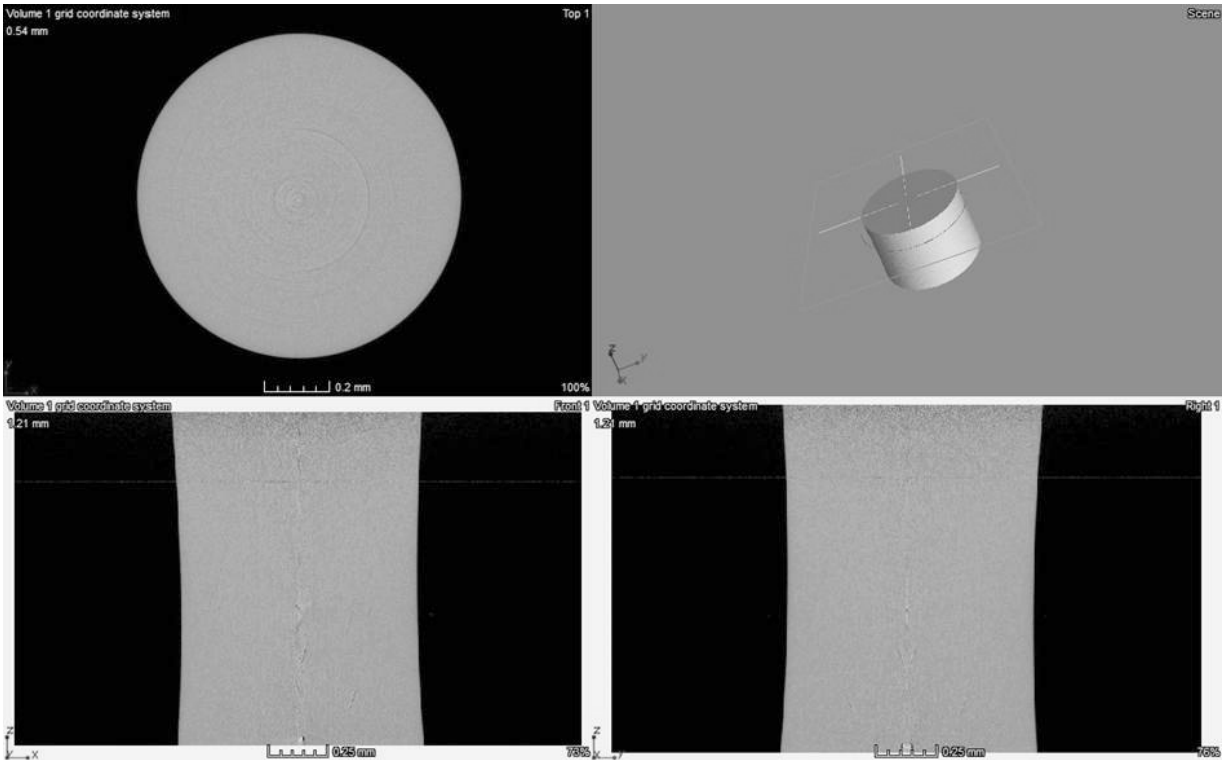


Figure 4.26: Section of 3-D tomography image of fatigue reference sample EP Ti-2.5Cu (SHT).

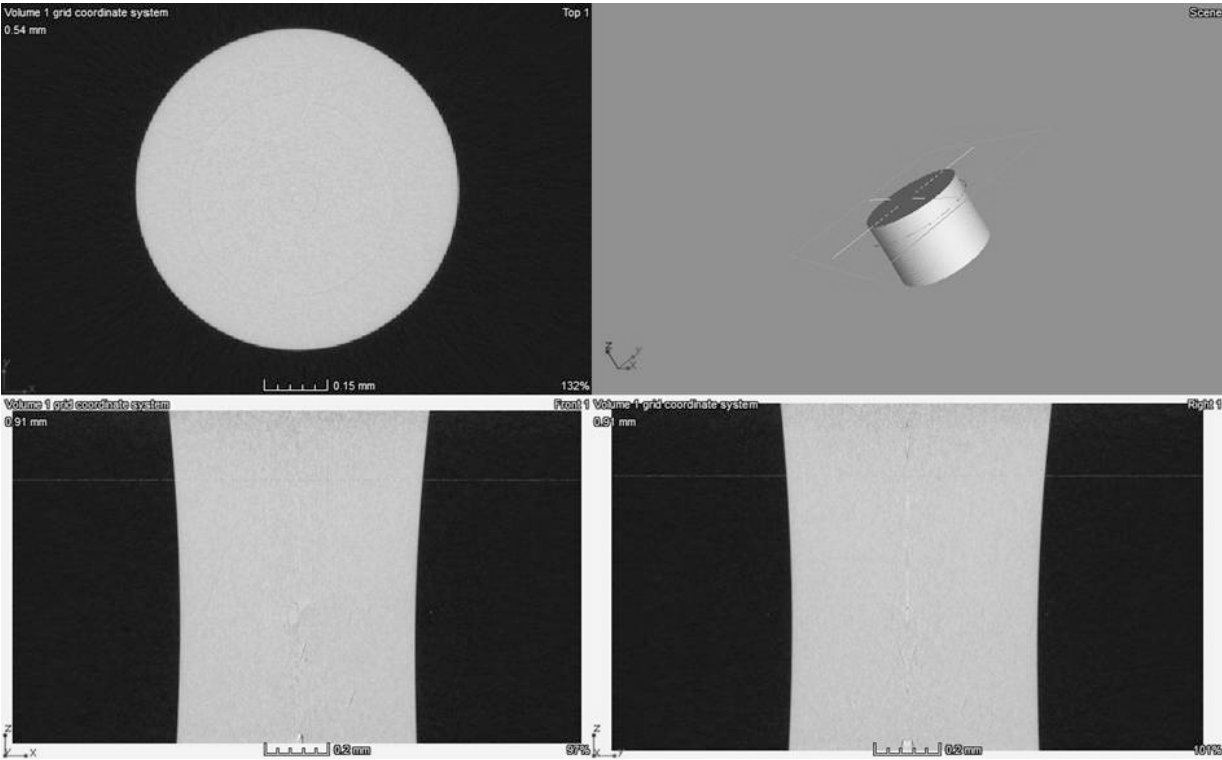
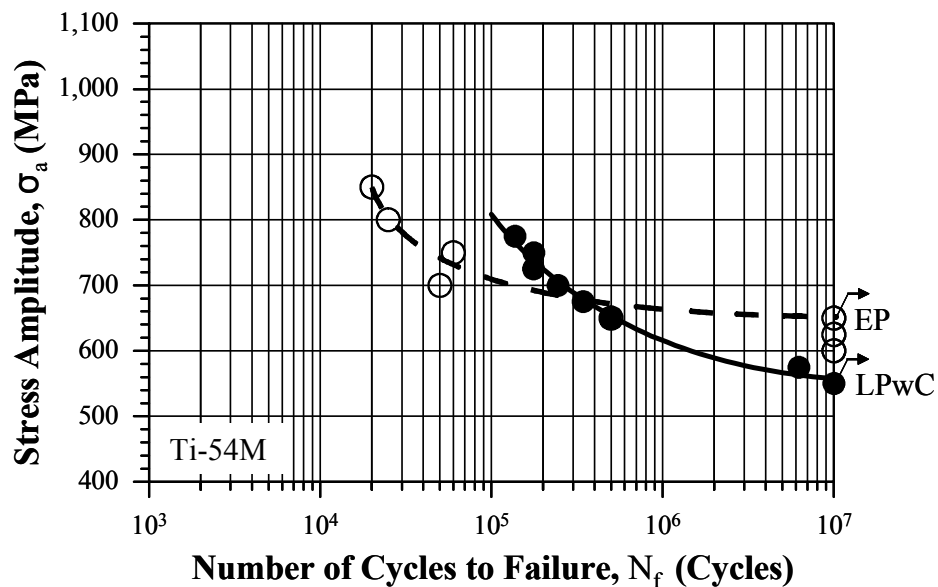


Figure 4.27: Section of 3-D tomography image of BB fatigue sample of Ti-2.5Cu (SHT).

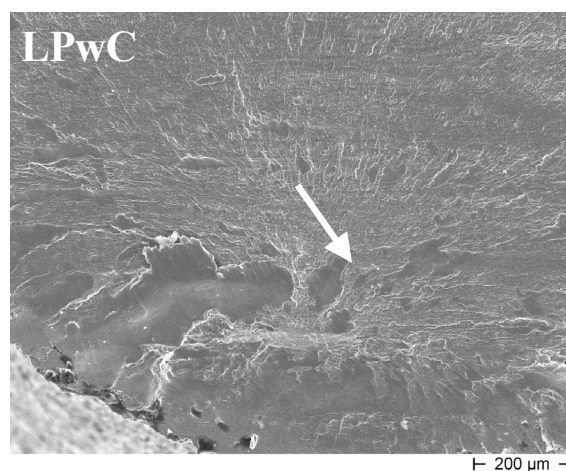
region between compressive and tensile layers. This is attributed to the smaller tensile residual stress of +200 MPa in BB fatigue sample (see Fig. 4.15) compared to the yield strength (UTS) of 610 MPa as listed in Table 3.2. Consequently, it is recommended to carry

out intensive studies using a higher resolution SR μ CT beamline such as IBL or HEMS at PETRA III at DESY to be able to detect defects with size smaller than 6 μm . Furthermore, in situ three-dimensional measurements of fatigue crack nucleation and propagation in mechanically surface treated Ti-2.5Cu during fatigue testing are recommended.

Further investigations on the fatigue behaviors of Ti-54M and LCB after LPwC were carried out. It was observed that the HCF strength of Ti-54M after LPwC decreased from 650 MPa (EP) to 550 MPa (LPwC) as illustrated in Fig. 4.28a. The reason could be the high sensitivity of ($\alpha+\beta$) alloys to tensile mean stress (see Section 2.4.1). K. Zay et al. [48] reported that the HCF performance of Ti-54M was slightly improved after SP and markedly improved after BB



a) S-N curves ($R = -1$) of Ti-54M.

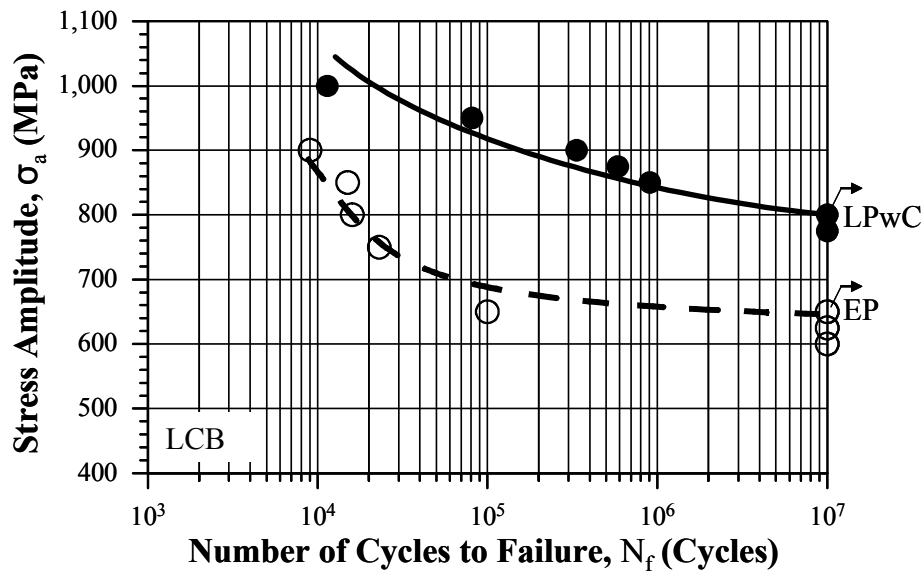


b) HCF crack nucleation sites in Ti-54M.

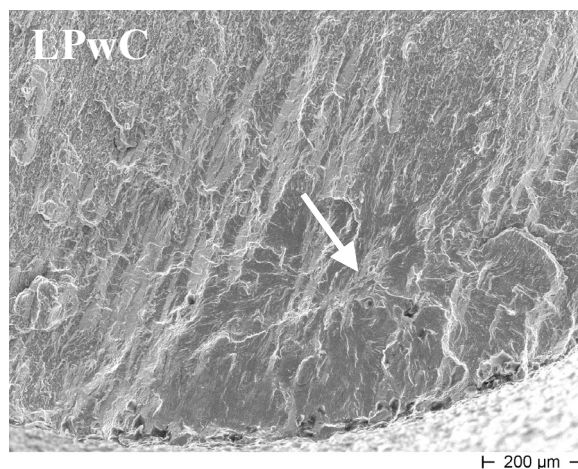
Figure 4.28: S-N curves ($R = -1$) (a) and HCF crack nucleation site (b) in Ti-54M after LPwC.

due to a normal mean stress sensitivity of that alloy. It should pay attention that the shot media used in the present study and in Ref. [48] were S330 and SCWW14, respectively. Further investigations should be carried out on Ti-54M by either removing a shallow layer (about 30-50 μm) from the surface after LPwC by electropolishing as reported elsewhere [169] for increasing the fatigue life of Ti-6Al-4V or by optimizing LPwC parameters to obtain reasonable surface quality without coating and enhancement of fatigue performance.

The S-N curves in rotating beam loading ($R = -1$) in air of LCB after LPwC and EP are shown in Figure 4.29a. Obviously, the HCF fatigue strength markedly increased from 650 MPa (EP) to 800 MPa after LPwC. This is also explained by the compressive residual stress induced in the surface layer and subsurface crack nucleation under quasi-vacuum condition (Fig. 4.29b).



a) S-N curves ($R = -1$) of LCB.



b) HCF crack nucleation sites in LCB.

Figure 4.29: S-N curves ($R = -1$) (a) and HCF crack nucleation site (b) in LCB after LPwC.

Moreover, the higher HCF strength of LCB (EP) compared to that of Ti-2.5Cu (EP) is attributed to higher yield and tensile strengths of LCB, while the HCF strengths of LCB (EP) and Ti-54M (EP) are the same.

4.7 Change of Local Crystallographic Texture after Various Surface Treatments

In the present study, the global crystallographic texture in, as an example, Ti-2.5Cu (SHT) was examined as a first step before describing the change of the local texture at the surface by performing various mechanical surface treatments.

4.7.1 Global Crystallographic Texture

a. Global Texture by Neutron Diffraction

The global crystallographic texture of the hot-rolled Ti-2.5Cu (SHT) has been evaluated by using neutron diffraction in terms of the measured pole figures as shown in Fig. 4.30. Strongest texture component is the split (00.2) basal plane orientation in the normal direction with an angle of $\pm 15^\circ$ ($c/a = 1.587$). A second texture component is at ND, which is slightly weaker, with a degree of freedom towards RD. A third texture component is the $\langle 10.0 \rangle$ fibre with the girdle in (00.2), visible in both pole figures (dash lines in Fig. 4.30).

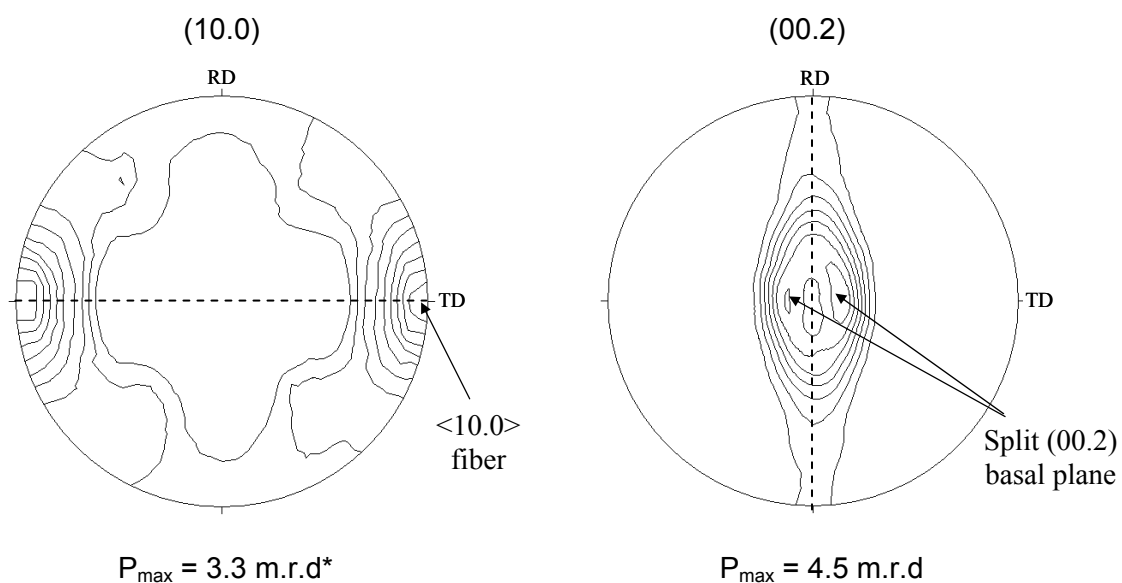


Figure 4.30: Pole figures of the hot rolled Ti-2.5Cu measured by neutron diffraction

* m.r.d = multiples of random distribution

The deviation from the perfect basal pole figure usually observed on cold-rolled CP-Ti is caused by a solid solution beta-eutectoid element (Cu). This is due to the finely dispersed second phase (Ti_2Cu). The presence of a finely dispersed second phase within the grains has the effect of reducing the grain size and probably would be influential in the suppression of (11.2) twinning which plays an important role with (00.2) slipping to rotate the basal poles towards the TD in CP-Ti. Moreover, a decrease in the critical resolved shear stress for basal slip could also be effective in producing this texture. Furthermore, it was investigated the effect of alloying elements on the lattice parameters and it is found that there was too little changes in lattice parameters to cause a pronounced effect on texture. Mechanical surface treatments produce plastic deformation in the surface layer. This could locally change the initial texture. However, the role of the Ti_2Cu to change the activation mode in Ti-2.5Cu during plastic deformation is still less understood. Therefore, the texture variation during uniaxial tension at ambient temperature by using synchrotron radiation was studied.

b. Texture Variation during In Situ Plastic Deformation by Synchrotron Radiation

The investigation of texture variations during uniaxial tension at ambient temperature was carried out at Hasylab at DESY as explained in details in section 3.7.2.b. The stress–strain curve of Ti-2.5Cu (SHT) from the in situ measurement is illustrated in Fig. 4.31.

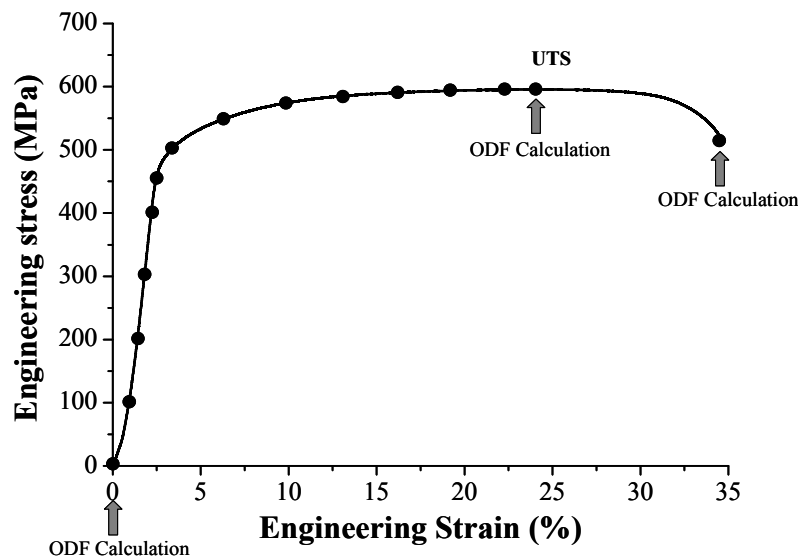


Figure 4.31: Engineering stress-strain curve of Ti-2.5Cu (SHT)

ODF = Orientation Distribution Function

The Orientation Distribution Function (ODF) was calculated at the initial (Fig. 4.32a), UTS (Fig. 4.32b) and fracture (Fig. 4.32c) strains as indicated by arrows in Fig. 4.31.

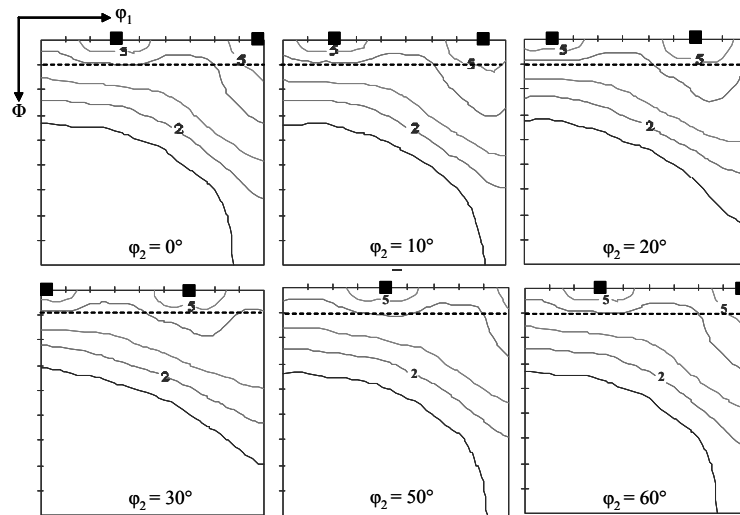
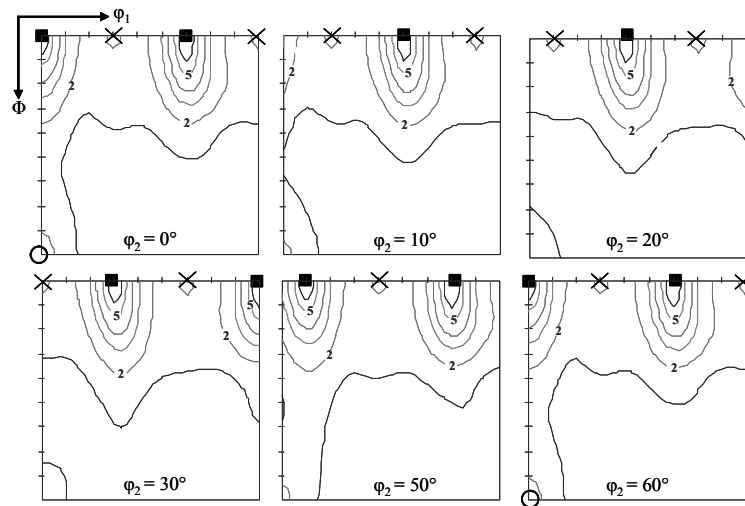
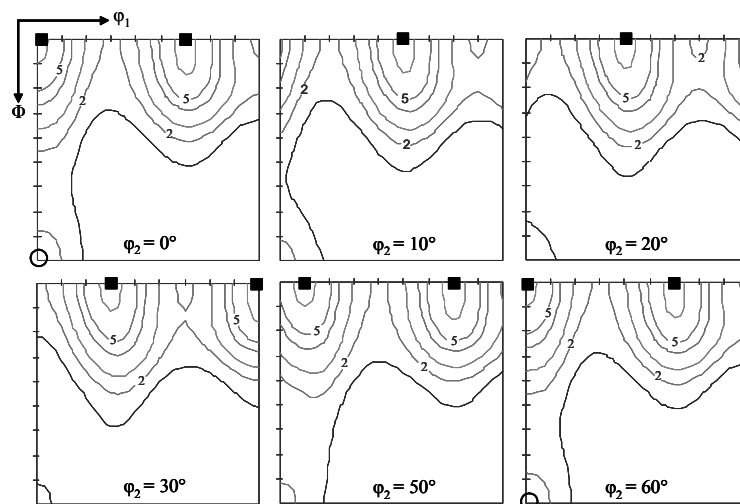
a) Initial texture ($F_{\max} = 4.75$)b) Texture at UTS ($F_{\max} = 6.84$)c) Texture at fracture ($F_{\max} = 7.38$)

Figure 4.32: ODF sections showing texture variation during tensile loading at initial (a), UTS (b) and fracture (c) strains.

It is clearly shown that the initial texture is mainly composed of 2 strong components, $\{00.1\} \langle 11.0 \rangle$ (indicated by shaded squares in Fig. 4.32a) and $\{00.1\}$ basal fiber (dashed line). At fracture strain, result revealed that the initial texture was changed from $\{00.1\} \langle 11.0 \rangle$ component to stronger $\{00.1\} \langle 10.0 \rangle$ component (indicated by shaded squares). Furthermore, it was observed that relatively weaker $\{11.0\} \langle 10.0 \rangle$ component was activated (indicated by opened circles Fig. 4.32c). The activation of $\{11.0\} \langle 10.0 \rangle$ component is caused by little increase of $\{11.2\}$ twins due to a greater reduction along the c-axis. Therefore, suppression of $\{11.2\}$ twins by the second phase Ti_2Cu was overcome by higher reduction (43%). The ODF at ultimate tensile stress (UTS = 600 MPa at uniform strain of 23.5%) shows a combination of weaker initial texture (indicated by crosses in Fig. 4.32b) and relatively stronger texture of broken sample.

4.7.2 Texture Variation in the Mechanically Surface Treated Layers

The influence of SP, BB, USP and LPwC on the local texture in the surface layer of Ti-2.5Cu has been investigated using the Lab-XRD. Figures 4.33b-e show an example of the changes of the (00.2) and (10.2) pole figures in Ti-2.5Cu (SHT) within the penetration depth from 0 to 10 μm . Due to a greater surface roughness (17 μm) produced by LPwC, a surface layer with a thickness of 20 μm was removed by electropolishing process. These pole figures were compared with the pole figure of the virgin material as illustrated in Fig. 4.33a. It is observed that the (00.2) pole figures measured by both neutron (Fig. 4.30) and Lab-XRD (Fig. 4.33a) are slightly different due to different resolutions of both methods. Furthermore, it could be explained by different textures developed at the surface and the core after rolling due to different flow rates and corresponding strains. This different flow rates are a result of the friction influence between the roll and the surface.

As seen in Fig. 4.33b, the texture of the starting material at the surface was locally destroyed and a weak texture was produced during SP. This is attributed to radial material flow caused by the shot impact normal to the surface as shown schematically in Fig. 4.34. Indeed, this weaker texture after SP led to isotropic behavior of the generated residual stresses in the surface layers. In contrast, as previously mentioned in this chapter, the residual stresses induced after BB (Fig. 4.13) and LPwC (Fig. 4.12) are anisotropic. This could be explained by relatively stronger texture developed by BB (Fig. 4.33b) and LPwC (Fig. 4.33e) compared to that by SP.

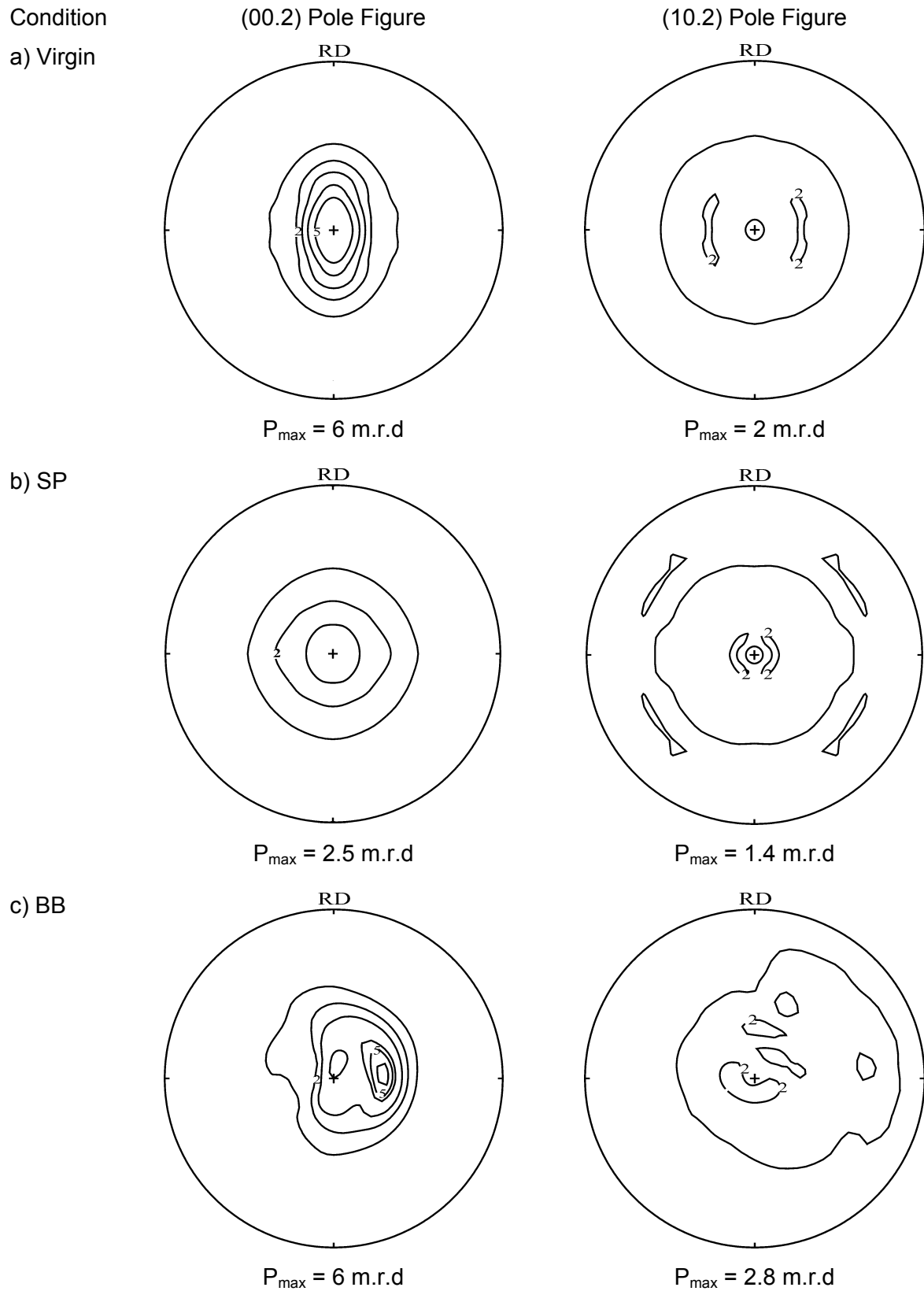


Figure 4.33 (Part I): (00.2) and (10.2) pole figures developed in the surface layer ($0 \rightarrow 10 \mu\text{m}$) of the rolled virgin Ti-2.5Cu (SHT) after SP (b) and BB (c).

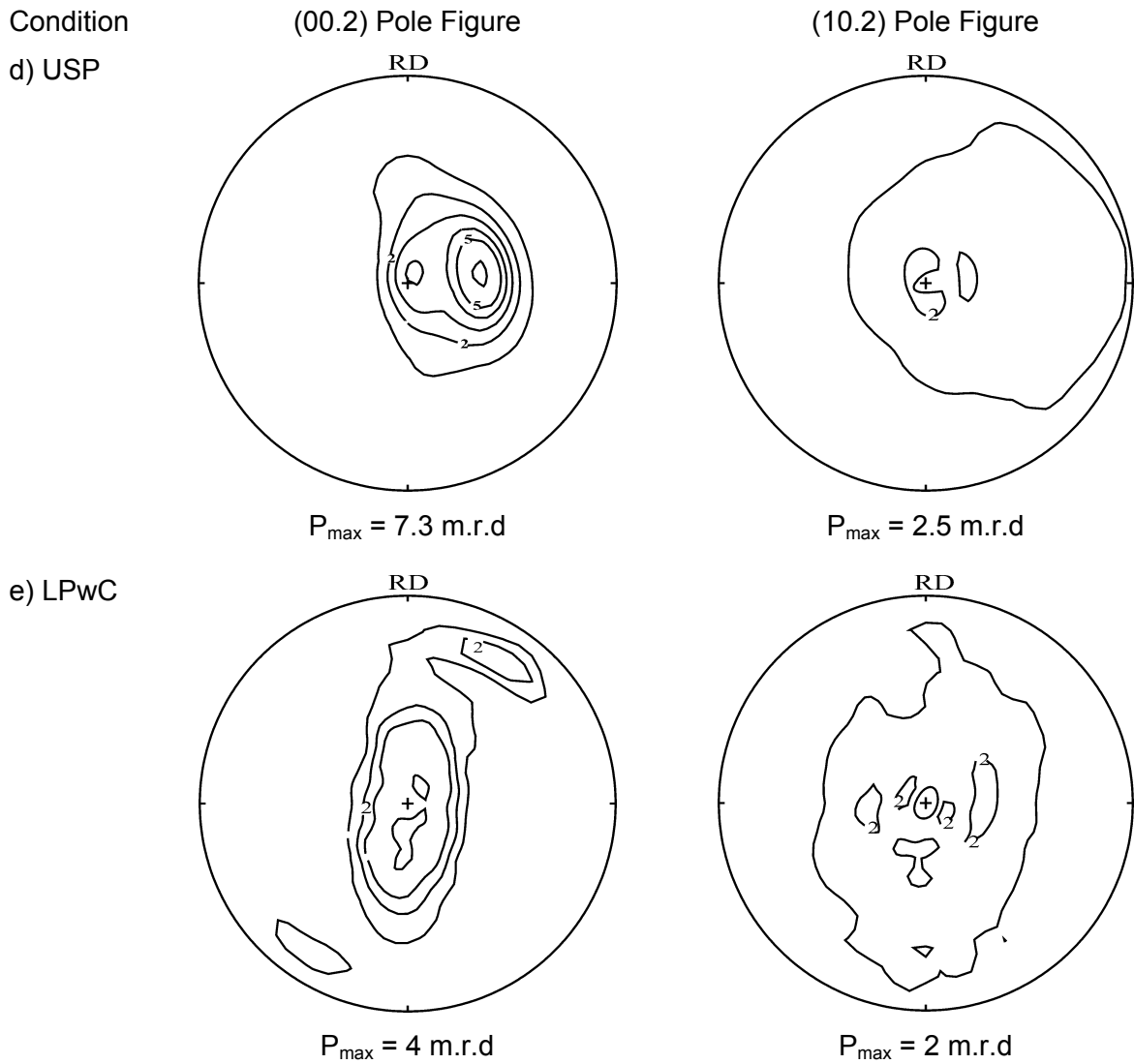


Figure 4.33 (Part II): (00.2) and (10.2) pole figures developed in the surface layer (0 → 10 μm) of the rolled virgin Ti-2.5Cu (SHT) after USP (d) and LPwC (e).

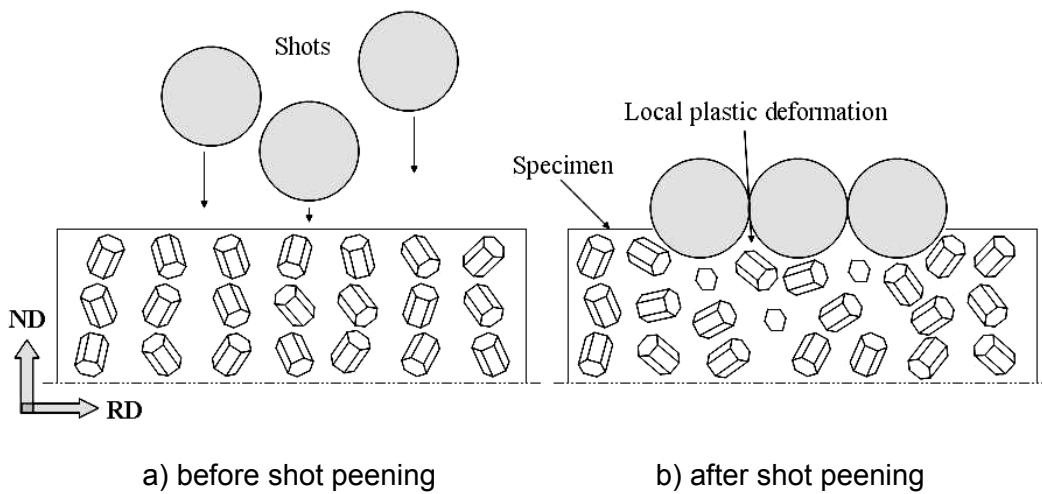


Figure 4.34: Scheme illustrating the destroyed texture due to shot peening. (ND = normal direction, RD = rolling direction)

Obviously, asymmetric grain orientations were produced after BB, USP and LPwC, while SP produced a symmetric texture. The Hertzian contact between surface and relatively large ball size of 6 mm and 1.5 mm in diameter used in BB and USP processes, respectively, compared to shot size of about 0.8 mm in diameter used in SP process. This resulted in increases of surface waviness after BB or USP affecting on the pole figures symmetry due to lower penetration depth of Lab-XRD beam. During LPwC process, as previously mentioned, the top surface of the samples slightly melts or evaporates through ablative interaction between the intense laser pulses and the surface. Therefore, asymmetric texture was developed depending on the plasma temperature, cooling rate and laser scanning direction.

Texture gradient in the surface layers of Ti-2.5Cu (SHT), as an example, has been investigated by using Lab-XRD as illustrated in Fig. 4.35. Obviously, the sharpness of the basal pole figures at different distances from the shot peened surface differs. The maximum basal pole density increased from $P_{\max} = 4.5$ m.r.d (Fig. 4.35a) to 5.7 m.r.d (Fig. 4.35b) at the depths of 120→130 μm and 220→230 μm , respectively, compared to the maximum basal pole density ($P_{\max} = 2.5$ m.r.d) at the surface (0→10 μm) as shown in Fig. 4.33b. This is explained by greater plastic deformation at the surface which gradually decreased in the near-surface layer (see Figs. 4.8a and 4.10a).

Furthermore, the basal poles are oriented towards the RD, when the distance increases from the surface to become similar to the basal poles measured by neutron as a bulk texture (Fig. 4.30). This confirms that there was a texture gradient in the as-received rolled plate before performing shot peening process. For comparison, texture was measured in the region having no influence of the plastic deformation (greater than 250 μm in depth) according to the hardness-depth profile shown in Fig. 4.8a. It is observed that the basal pole density ($P_{\max} = 6.1$ m.r.d) at depth of 340→350 μm (Fig. 4.35c) is nearly similar to that at the surface ($P_{\max} = 6.4$ m.r.d), shown in Fig. 4.33a, but the distribution of the poles is slightly elongated towards RD due to the texture gradients developed in the as-received sheet during rolling.

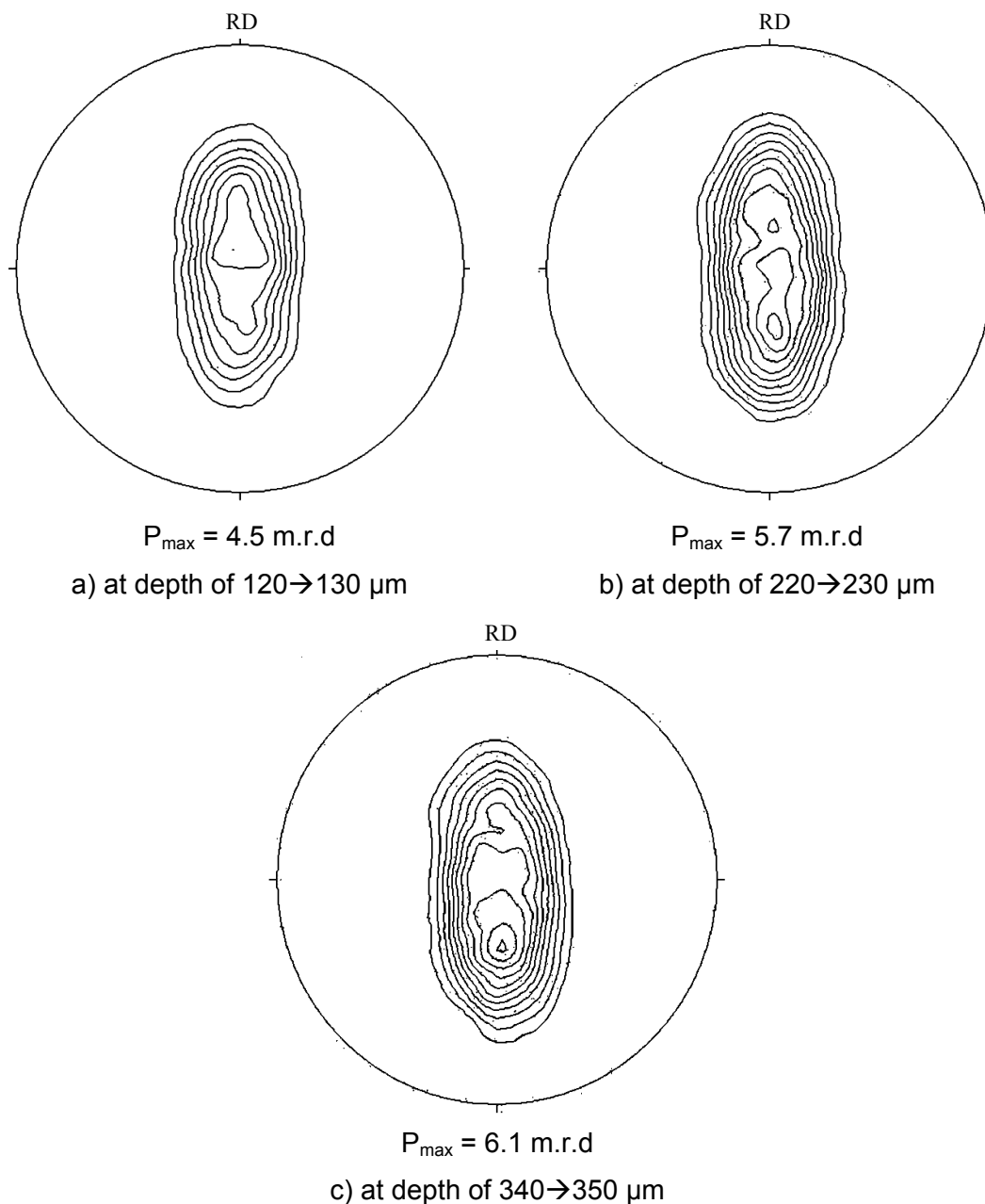


Figure 4.35: Basal pole figures of shot peened Ti-2.5Cu at depth of 120→130 μm (a), 220→230 μm (b) and 340→350 μm (c).

Conclusions and Recommendations

Conclusions

1. The presented results indicate that the high cycle fatigue (HCF) performance of Ti-2.5Cu was more improved by applying laser shock peening without coating (LPwC) than that by applying conventional shot peening (SP). This is due to the greater amount and depth of compressive residual stresses in the surface layer after LPwC. On the other hand, ball-burnishing (BB) resulted in better HCF performance of Ti-2.5Cu than SP or LPwC. The same beneficial influence of LPwC on Ti-2.5Cu was also observed for LCB. On the contrary, LPwC deteriorated the HCF performance of Ti-54M. It was argued that the reason could be the high sensitivity of ($\alpha+\beta$) alloys to tensile mean stress.
2. Balancing tensile residual stress could play more significant role in LCF behavior during rotating beam loading compared to that in the HCF performance.
3. The compressive residual stresses are thermally more stable in LPwC surface layer than those in the surface layers after SP, ultrasonic shot peening (USP) or BB.
4. Resolidified droplets and craters produced after LPwC led to very rough surfaces. This could be an advantage for biomaterials applications such as implants which require higher surface roughness beside greater compressive residual stresses.
5. By combining energy dispersive X-ray and neutron diffraction, results revealed that the higher compressive residual stress distribution induced by BB on one side influenced the residual stress state on the other side. This can be explained by generating relatively higher balancing tensile residual stress (200 MPa) compared to the tensile residual stress (50 MPa) induced in Ti-2.5Cu (SHT) after performing BB on one side only.
6. The crystallographic textures of the surface layers were changed by applying mechanical surface treatments. These local texture changes might affect surface and near-surface properties, such as the resistance to fatigue crack nucleation and microcrack growth. Furthermore, weaker texture developed during SP is the reason why no difference between in-plane residual stress components was observed. The

weaker texture, the more accurate residual strain measurements by energy dispersive X-ray diffraction.

7. By using synchrotron radiation micro-computed tomography with a resolution of 5.63 μm , no manufacturing defects were observed with a size greater than 6 μm in the surface layer or in the bulk of Ti-2.5Cu (SHT) fatigue samples.

Recommendations

For further investigations on this field of study, the following points are recommended:

1. Further investigations should be carried out on Ti-54M by either removing a shallow layer (about 30-50 μm) from the surface after LPwC by electropolishing or by optimizing LPwC parameters to obtain reasonable surface quality without coating and enhancement of fatigue performance.
2. To understand the role of balancing tensile residual stresses on the fatigue crack nucleation, axial fatigue tests should be carried out.
3. In situ three-dimensional fatigue cracks distributions in mechanically surface treated Ti-alloys should be investigated by using synchrotron radiation micro-computed tomography with a high resolution.
4. Mechanical residual stress relaxation in mechanically surface treated Ti-alloys should be studied.
5. Stability of crystallographic textures during axial and rotating fatigue loading should be investigated.

References

- [1] J. Gambogi, S. J. Gerdemann, DOE/ARC (1999) 60.
- [2] G. Lütjering, J. C. Williams, *Engineering Materials and Processes, Titanium*, second ed., Berlin, 2007, pp 15.
- [3] M. F. Ashby, *Materials Selection in Mechanical Design*, third ed., London, 2005, pp 54
- [4] M. Peters, J. Hemptenmacher, J. Kumpfert, C. Leyens (Eds.), *Structure and Properties of Titanium and Titanium Alloys*, Weinheim, 2003, pp 1.
- [5] I.J. Polmear, *Light Alloys, Metallurgy of Light Metals*, second ed., New York (1989), pp 211.
- [6] ASM Handbook, *Materials Properties, Titanium Alloys*, Ohio, 1994, pp 415
- [7] ASM Handbook, *Alloy Phase Diagrams, Vol. 3*, Ohio, 1992, pp 2/180
- [8] V. Venkatesh, Y. Kosaka, J. Fanning, S. Nyakana, in: *Proc. of the 11th Int. World Conference on Titanium (JIMIC5)*, M. Niinomi, S. Akiyama, M. Ikeda, M. Hagiwara, K. Maruyama (Eds.), Kyoto, Japan, 2007, pp. 713.
- [9] Y. Kosaka, S. P. Fox, K. Faller and S. H. Reichman, *Mater. Eng. Perform.* 14 (6) (2005) 792.
- [10] O. Schauerte, *Adv. Eng. Mater.* 5 (6) (2003) 411-418.
- [11] E. Maawad, S. Yi, H.-G. Brokmeier, L. Wagner, in: *Proc. of the 10th Int. Conference on Shot Peening*, K. Tosha (Ed.), Tokyo, Japan, 2008, p. 499.
- [12] L. Wagner: *Mater. Sci. Eng. A* 263 (1999) 210.
- [13] E. Maawad, H.-G. Brokmeier and L. Wagner, *Solid State Phenomena* 160 (2010) 141.
- [14] V. Schulze, in: *Proc. of the 8th Int. Conference on Shot Peening*, L. Wagner (Ed.), Garmisch-Partenkirchen, Germany, 2002, pp 145.
- [15] G. Maurer, H. Neff, B. Scholtes and E. Macherauch: *Textures and Microstructures Vol. 8* (1988), pp 639.
- [16] T. R. Shives (Ed.), *Advanced Technologies in Failure Prevention*, Cambridge University Press, Cambridge, 1991, pp 92
- [17] S. Baiker (Ed.), *Shot Peening, A Dynamic Application and Its Future*, first ed., Switzerland, 2006.

- [18] S. K. Cheong, D. S. Lee, J. H. Lee, in: Proc. of the 10th Int. Conference on Shot Peening, K. Tosha (Ed.), Tokyo, Japan, 2008, pp 494.
- [19] Y. Watanabe, K. Hattori, M. Handa, N. Hasegawa, K. Tokaja, M. Ikeda. J. M. Duchazeaubeneix, in: Proc. of the 8th Int. Conference on Shot Peening, L. Wagner (Ed.), Garmisch–Partenkirchen, Germany, 2002, pp 305.
- [20] J.-M. Duchazeaubeneix, V. Desfontaine, S. Forgues, B. Labelle, in: Proc. of the 10th Int. Conference on Shot Peening, K. Tosha (Ed.), Tokyo, Japan, 2008, pp 401.
- [21] P. S. Prev y, in: Proc. of the 20th ASM Materials Solutions Conference & Exposition St. Louis, Missouri, 2000, pp 1.
- [22] N.H. Loh, S.C. Tam, *Precis. Eng.* 10–4 (1988) 215.
- [23] E. Maawad, H.–G. Brokmeier, M. Hofmann, Ch. Genzel, L. Wagner, *Mater. Sci. Eng. A* 527 (2010) 5745.
- [24] L. Wagner; M. Mhaede, K. Zay, *Metal Finishing News* 10 (2009) 58.
- [25] P. S. Prev y, J. T. Cammett, *Int. J. Fatigue* 26–9 (2004) 975.
- [26] E. Kannatey-Asibu, Jr., *Principles of Laser Materials Processing*, Hoboken, New Jersey, 2009, pp 603.
- [27] J.-E. Masse and G. Barreau, *Surf. Coat. Technol.* 70 (1995) 231.
- [28] X.C. Zhang, Y.K. Zhang, J.Z. Lu, F.Z. Xuan, Z.D. Wang and S.T. Tu, *Mater. Sci. Eng. A* 527 (2010) 3411.
- [29] R.K. Nalla, I. Altenberger, U. Noster, G.Y. Liu, B. Scholtes, R.O. Ritchie, *Mater. Sci. Eng. A* 355 (2003) 216.
- [30] I. Nikitin , B. Scholtes , H.J. Maier , I. Altenberger, *Scr. Mater.* 50 (2004) 1345.
- [31] M. Turski, S. Clitheroe, A. D. Evans, C. Rodopoulos, D. J. Hughes, P. J. Withers, *Appl Phys A* 99 (2010) 549.
- [32] S. Spanrad, J. Tong, *Mater. Sci. Eng. A* 528 (2011) 2128.
- [33] I. Altenberger, E.A. Stach, G. Liu, R.K. Nalla, R.O. Ritchie, *Scr. Mater.* 48 (2003) 1593.
- [34] S. Srinivasan, D. B. Garcia, M. C. Gean, H. Murthy, T. N. Farris, *Tribol. Int.* 42 (2009) 1324.
- [35] X.D. Ren, Y.K. Zhang, H.F. Yongzhuo, L. Ruan, D.W. Jiang, T. Zhang, K.M. Chen, *Mater. Sci. Eng. A* 528 (2011) 2899.
- [36] C. Yang, P. D. Hodgson, Q. Liu, L. Ye, *Mater. Process. Technol.* 201 (2008) 303.
- [37] Y. Sano, N. Mukai, K. Okazaki and M. Obata, *Nucl. Instrum. & Methods Phys. Res.*

- B, 121(1997) 432.
- [38] Y. Sano, M. Obata, T. Kubo, N. Mukai, M. Yoda, K. Masaki and Y. Ochi: *Mater. Sci. Eng. A* 417 (2006) 334.
- [39] E. Maawad, H.-G. Brokmeier, L. Wagner, Y. Sano and Ch. Genzel, *Surf. Coat. Technol.* 205 (2011) 3644.
- [40] N.R. Tao, Z.B. Wang, W.P. Tong, M.L. Sui, J. Lu, K. Lu, *Acta Mater.* 50 (2002) 4603.
- [41] K. Lu, J. Lu, *Mater. Sci. Eng. A* 375–377 (2004) 38.
- [42] A. L. Ortiz, J.-W. Tian, L. L. Shaw, and P. K. Liaw, *Scr. Mater.* 62 (2010) 129.
- [43] L. L. Shaw, J.-W. Tian, A. L. Ortiz, K. Dai, J. C. Villegas, P. K. Liaw, R. Ren, D. L. Klarstrom, *Mater. Sci. Eng. A* 527 (2010) 986.
- [44] J. Lindemann, L. Wagner, *Mater. Sci. Eng. A* 234-236 (1997) 1118.
- [45] L. Wagner, in: C. Leyens, M. Peters (Eds.), *Titanium and Titanium Alloys, Fundamentals and Applications*, first ed., Weinheim, 2003, pp 153.
- [46] J. Goodman, *Mechanics Appl. to Eng.*, London, 1899.
- [47] T. Ludian, M. Kocan, H. J. Rack and L. Wagner, *Mater. Res.* 97–9 (2006) 1425.
- [48] K. Zay, E. Maawad, H.-G. Brokmeier, L. Wagner and Ch. Genzel, *Mater. Sci. Eng. A* 528 (2011) 2554–2558.
- [49] J. Müller, H. J. Rack, T. Ludian, L. Wagner, in: *Proc. of the 7th Int. Conference on Titanium, Ti-2007 Sci. Technol.*, M. Niinomi, S. Akiyama, M. Hagiwara, K. Maruyama (Eds.), Japan, 2007, pp 375.
- [50] M. Kocan, H. J. Rack, L. Wagner, in: *Proc. of the 7th Int. Conference on Titanium, Ti-2007 Sci. Technol.*, M. Niinomi, S. Akiyama, M. Hagiwara, K. Maruyama (Eds.), Japan, 2007, pp 1241.
- [51] M. Kocan, H. J. Rack, L. Wagner, in: *Proc. of the 7th Int. Conference on Titanium, Ti-2007 Sci. Technol.*, M. Niinomi, S. Akiyama, M. Hagiwara, K. Maruyama (Eds.), Japan, 2007, pp 367.
- [52] G. M. Lohse, A. Senemmar, H.-J. Christ, in *Proc. of the 6th Int. Conference on Titanium, Ti-2003*, G. Lütjering, J. Albrecht (Eds.), Hamburg, 2003, pp 1723.
- [53] M. Sugano, S. Kanno, T. Satake, *Acta Mater.* 37–7 (1989) 1811.
- [54] C. D. Beacham, *Metall. Trans. A* 3 (1972) 432.
- [55] E. Sirois, H. K. Birnbaum, *Acta Metall. Mater.* 40 (1992) 1377.
- [56] E. A. Steigerwald, F. W. Schaller, A. R. Troiana, *Trans. AIME* 218 (1960) 125.

- [57] S. Gahr, M. L. Grossbeck, H. K. Birnbaum, *Acta Metall.* 25 (1977) 125.
- [58] P. J. Withers, H. K. D. H. Bhadeshia: *Int. J. Mat. Sci. Technol.* 17 (2001) 355.
- [59] G. Totten, M. Howes, T. Inoue (Eds.), *Handbook of Residual Stress and Deformation of Steel*, ASM International, OH, 2002, pp 347.
- [60] W. Zinn, J. Schulz, R. Kopp, B. Scholtes, in: *Proc. of the 8th Int. Conference of Shot peening*, L. Wagner (Ed.), Garmisch-Partenkirchen, Germany, 2002, pp 161.
- [61] P. S. Prev y, J. Cammett, in: *Proc. of the 8th Int. Conference of Shot peening*, L. Wagner (Ed.), Garmisch-Partenkirchen, Germany, 2002, pp 295.
- [62] F. Petit-Renaud, in: *Proc. of the 8th Int. Conference of Shot peening*, L. Wagner (Ed.), Garmisch-Partenkirchen, Germany, 2002, pp 119.
- [63] E. B. Chef, *Effect of Peening and Re-Peening on the Improvement of Fatigue Life of In-Service Components*, Cranfield University, 1982.
- [64] Metal Improvement Company, *Shot peening Application*, seventh ed., USA, 1980.
- [65] D. Kirk, *Shot peening*, Seminar, USF Vacublast Slough, 1998.
- [66] Y. Mutoh, G. H. Fair, B. Noble, R. B. Waterhouse, *Fatigue Fract. Eng. Mat. Struct.* 10 (1987) 261.
- [67] P. S. Prev y, in: *Proc. of the 5th Natl. Turbine Engine HCF Conference*, Chandler, AZ, 2000.
- [68] D.W. Hammonda, S.A. Meguid, *Eng. Fract. Mech.* 37 (1990) 373.
- [69] L. Wagner, M. Wollmann, in: *Proc. of the 10th Int. Conference on Shot Peening*, K. Tosha (Ed.), Tokyo, Japan, 2008, pp 355.
- [70] T. Ludian, J. Atoura, L. Wagner, in: *Proc. of the 10th Int. Conference on Shot Peening*, K. Tosha (Ed.), Tokyo, Japan, 2008, pp 375.
- [71] R. Menig, L. Pintschovius, V. Schulze, O. Voehringer, *Scr. Mater.* 45 (2001) 977.
- [72] S. Clitheroe, M. Turski, A. Evans, J. Kelleher, D. Hughes, P. Withers, in: *Proc. of the 10th Int. Conference on Shot Peening*, K. Tosha (Ed.), Tokyo, Japan, 2008, pp 47.
- [73] A. N. Ezeilo, G. A. Webster, P. S. Webster, L. Castex, in: *Proc. of the 5th Int. Conference of Residual Stresses*, T. Ericsson, M. Oden, A. Andersson (Eds.), Inst. Tech., Linkopings University, Sweden, 1997, pp 726.
- [74] P. Kesavan, R. Vasudevan, *S adhan * 20–1 (1995) 39.
- [75] Manual BRUKER AXS, DIFFRAC^{plus}, *Residual Stress Determination (STRESS)*, Germany, 1998, p 2.
- [76] C.O. Ruud, *NDT Int.* 15–1 (1982) 15.

- [77] I. C. Noyan and J. B. Cohen, *Residual Stress: Measurement by Diffraction and Interpretation*, Springer-Verlag, New York, 1987.
- [78] T. Kuntz, H. Wadley, D. Black, *Mettall. Trans. A* 24A (1993) 1117.
- [79] A. Pyzalla, *J. Nondestructive Eval.* 19 (2000) 21.
- [80] L. Suominen, D. Carr, *International Centre for Diffraction Data (JCPDS)* 43 (2000) 21.
- [81] Ch. Genzel, C. Stock, B. Wallis and W. Reimers, *Nucl. Instrum. Methods A* 467- 468 (2001) 1253.
- [82] B. Kämpfe, F. Luczak, B. Michel, *Part. Part. Syst. Charact.* 22 (2005) 391.
- [83] P. S. Prevéy, *Develop. in Mater. Charact. Technol.*, G. Vander Voort, J. Friel (Eds.), ASM International, Materials Park, OH, 1996, pp 103.
- [84] P. S. Prevéy, *Shot Peening Theory and Application*, A. Niku-Lari (Ed.), IITT-International, Gournay-Sur-Marne, France, 1990, pp 81.
- [85] P. S. Prevéy, *Residual Stress for Designers & Metallurgists*, ASM International, Metals Park, OH, 1981, pp 151.
- [86] P. S. Prevéy, *X-ray Diffraction Residual Stress Techniques*, *Metals Handbook*, 10, ASM International, Materials Park, OH, 1986, pp 380.
- [87] W. Pfeiffer, in: *Proc. of the 9th Int. Conf. on Shot Peening. Technology Transfer Series*, IITT-International, France, 2005, pp 414.
- [88] G. Bruno, C. Fanara, D. J. Hughes, N. Ratel, *Nucl. Instrum. Methods in Phys. Res. B* 246 (2006) 425.
- [89] A. J. Allen, M.T. Hutchings, C.G. Windsor, C. Andreani, *Adv. Phys.* 34 (1985) 445.
- [90] P. J. Withers, H. K. D. H. Bhadeshia, *Mater. Sci. Tech.* 17 (2001) 355.
- [91] G. Albertini, G. Bruno, A. Carrad , F. Fiori, M. Rogante, F. Rustichelli, *Meas. Sci. Technol.* 10 (1999) R56.
- [92] J. R. Santisteban, L. Edwards, A. Steuwer, P. J. Withers, *Appl. Cryst.* 34 (2001) 289.
- [93] H. G. Priesmeyer, J. Larsen, K. Meggers, *Neutron Res.* 2-1 (1994) 31.
- [94] J. Hoffmann, B. Scholtes, O. Vöhringer, E. Macherauch, *Residual Stresses in Sci. and Technol.* 2 (1987) 695.
- [95] C. Lykins, P. Prevéy, P. Mason, *Aero Propulsion and Power Directorate, Wright-Patterson AFB, OH, Report No. WL-TR-95-2108*, 1995.
- [96] P. Prevéy, D. Hornbach, P. Mason, in: *Proc. of the 17th Heat Treating Society Conference and Exposition*, D.L. Milam et al. (Eds.), ASM, Materials Park, OH,

- 1998, pp 3.
- [97] M. C. Berger, J. K. Gregory, *Mater. Sci. Eng. A* 263 (1999) 200.
- [98] A. Medvedeva, J. Bergström, S. Gunnarsson, P. Krakhmalev, *Mater. Sci. Eng. A* 528–3 (2011) 1773.
- [99] Y. Hu, W. Floer, U. Krupp, H. J. Christ, *Mater. Sci. Eng. A* 278 (1999) 170.
- [100] D. Banerjee, J. C. Williams, *Def. Sci. J.*, 36 (1986) 191.
- [101] A. T. Churchman, *Proc. Royal Soc., A. London* 226 (1954) 216.
- [102] J. C. Williams, M. J. Blackburn, *Phys. Stat. Sol.*, 25 (1968) K1.
- [103] N. E. Paton, J. C. Williams, G. P. Rauscher, *Titanium Sci. Technol.*, Plenum Press, R.J. Jaffee, H.M. Burte (Eds.), New York, Vol. 2, 1973, pp 1049.
- [104] Paton, N. E. & Backofen, W. A., *Metall. Trans.*, 1 (1970) 2839.
- [105] I. P. Jones, W. B. Hutchinson, *Acta Meter.* 29 (1981) 951.
- [106] H. Baker, H. Okamoto, S.D. Henry, *ASM Handbook, Alloy Phase Diagram*, Vol. 3, ASM International, Materials Park, Ohio, 1992, pp 180.
- [107] J.C. Williams, R. Taggart, D.H. Polonis, *Metall. Trans.* 2 (1971) 1139.
- [108] S.-H. Wang, C. Müller, *Fatigue Fracture Eng. Mater. Struct.* 21 (1998) 1077.
- [109] Q.Y. Sun, Z.T. Yu, R.H. Zhu, H.C. Gu, *Mater. Sci. Eng. A* 364 (2004) 159.
- [110] F. R. Larson, A. Zarkades, and D. H. Avery: in *Proc. of the 2nd Int. Conference on Titanium Sci. and Technol.*, R. I. Jaffee (Ed.), Vol. 2, Massachusetts, 1972, p. 1169.
- [111] V. Randle, O. Engler, *Introduction to Texture Analysis, Macrotecture, Microtexture and Orientation Mapping*, part 1, *Fundamental Issues*, 2000, pp 3.
- [112] P. Yvrk, *Texture-Dependent Mechanical Properties of Metals and Alloys*. In: *Trans. of the Indian Institute of Metals*, 37–4 (1984) 399.
- [113] H. J. Bunge (Ed.), *Quantitative Texture Analysis, General Outline and Series Expansion Method*, C. Esling, 1986, pp 3.
- [114] Y.N. Wang, J.C. Huang, *Mater. Chem. Phys.* 81 (2003) 11.
- [115] ASM, *Metals Reference Book*, 3rd Edition, 1993, pp 67.
- [116] H.-G. Brokmeier, S. Yi, in: W. Reimers, A. Pyzalla, A. Schreyer, H. Clemens (Eds.), *Neutrons and Synchrotron Radiation in Engineering Materials Science*, Weinheim, 2008, pp 61.
- [117] D. Raabe, *Textures and Microstructures* 23 (1995) 115.
- [118] H. J. Bunge, *Zeit. Metallkunde* 56 (1965) 872.

- [119] H. J. Bunge, *Zeit. Metallkunde* 70 (1979) 411.
- [120] R. Roe, *Appl. Phys.* 36 (1965) 2024.
- [121] R. D. Williams, *Appl. Phys.* 39 (1968) 4329.
- [122] D. Ruer, R. Baro, *Adv. X-ray Anal.* 20 (1977) 187.
- [123] J. Imhof, *Zeit. Metallkunde* 68 (1977) 38.
- [124] S. Matthies, G. W. Vinci, *Phys. Star. Sol., (b)* 112 (1982), K111.
- [125] H. Schaeben, *Phys. Star. Sol., (b)* 123 (1984) 425.
- [126] K. Pawlik, *Phys. Stat. Sol., (b)* 134 (1986) 477.
- [127] K. Pawlik, J. Pospiech, K. Lticke, in: *Proc. of ICOTOM 9*, H. J. Bunge (Ed.), Vol. 14, 1991, pp 25.
- [128] H.-G. Brokmeier, S. Yi, J. Homeyer, *Microstructure and Texture in Steels*, A. Haldar, S. Suwas, D. Bhattacharjee (Eds.), 2009, pp 307.
- [129] H. G. Brokmeier, *Phys. B* 234–236 (1997) 977.
- [130] H. J. Bunge: *Textures and Microstructures*, 10 (1989) 265.
- [131] H.-G. Brokmeier: *Phys. B* 385–386 (2006) 623.
- [132] H.-R. Wenk, P. V. Houtte, *Texture and anisotropy*, *Rep. Prog. Phys.* 67 (2004) 1367.
- [133] U. F. Kocks, C. N. Tomé, H.-R. Wenk, *Texture and anisotropy*, Cambridge, 2000. pp 204.
- [134] T. Donath, *Quantitative X-ray Microtomography with Synchrotron Radiation*, GKSS 2007/17.
- [135] S. Rolland du Roscoat, J.-F. Bloch, X. Thibault, *Phys. D: Appl. Phys.* 38 (2005) A78.
- [136] F. Beckmann, R. Grupp, A. Haibel, M. Huppmann, M. Nöthe, A. Pyzalla, W. Reimers, A. Schreyer, R. Zettler, *Adv. Eng. Mater.* 9–11 (2007) 939.
- [137] C. Verdu, J. Adrien, J. Y. Buffière, *Mater. Sci. Eng. A* 483–484 (2008) 402.
- [138] E. Ferrie, J.-Y. Buffière, W. Ludwig, A. Gravouil, L. Edwards, *Acta Mater.* 54 (2006) 1111.
- [139] H. Zhang, H. Toda, P. C. Qu, Y. Sakaguchi, M. Kobayashi, K. Uesugi, Y. Suzuki, *Acta Mater.* 57 (2009) 3287.
- [140] S. Biroasca, J.Y. Buffière, F.A. Garcia-Pastor, M. Karadge, L. Babout, M. Preuss, *Acta Mater.* 57 (2009) 5834.
- [141] *Proc. of the 6th International Topical Meeting on Neutron Radiography*, 2008, Japan,

- Nucl. Instr. and Meth. A 605 (2009).
- [142] A.S. Tremsin, J.B. McPhate, J.V. Vallerga, O.H.W. Siegmund, W.B. Feller, E. Lehmann, L.G. Butler, M. Dawson, Nucl. Instrum. and Methods A (2010), doi:10.1016/j.nima.2010.08.009 (in press)
- [143] R. Flitney, Seals and Searling Handbook, fifth ed., General information, 2007. pp 478.
- [144] J.W. Flowers Jr., K.C. O'Brien, P.C. McElenery, Less Common Metals 7-5 (1964) 393-395.
- [145] Ch. Genzel, I. A. Denks, M. Klaus, Mater. Sci. Forum 524–525 (2006) 193.
- [146] Ch. Genzel, C. Stock and W. Reimers, Mater. Sci. Eng. A 372 (2004) 28.
- [147] E. Kröner: Z. Phys. 151 (1958) 504.
- [148] T. Ungár, Mater. Sci. Eng. 14219 (2000) 1.
- [149] T. Ungár, Scr. Mater. 51 (2004) 777.
- [150] J. Pelleg, E. Elish: Vac. Sci. Technol. A20 (2001) 745.
- [151] M. Hofmann, R. Schneider, G.A. Seidl, J. Rebelo-Kronmeier, R.C. Wimpory, U. Garbe, H.-G. Brokmeier, Phys. B 385–386 (2006) 1035.
- [152] T. Lorentzen, M. T. Hutchings, P. J. Withers and T. M. Holden, Introduction to the Characterization of Residual Stress by Neutron Diffraction, Appendix 2, 2005, p 365.
- [153] G. Bruno, C. Fanara, D. J. Hughes, N. Ratel: Int. J. Nucl. Instrum. Methods in Phys. Res. B 246 (2006) 425.
- [154] M. Mhaede, Corrosion Performance of High Strength Al Alloys- Effect of Mechanical Surface Treatments, PhD Thesis, Clausthal University of Technology, Clausthal-Zellerfeld, Germany, 2009.
- [155] H.-G. Brokmeier, Phys. B 234–236 (1997) 1144.
- [156] L. Lutterotti, S. Gialanella. Acta Mater. 46 (1998) 101.
- [157] H.M. Rietveld, Appl. Cryst. 2 (1969) 65.
- [158] F. Beckmann, Entwicklung, Aufbau und Anwendung eines Verfahrens der Phasenkontrast Mikrotomographie mit Röntgen- Synchrotronstrahlung. PhD Thesis, University of Dortmund, Dortmund, Germany, 1998.
- [159] J. Atoura, L. Wagner, in: Proc. of the 12th Int. Conference on Titanium, Ti-2011 Sci. Technol., L. Zhou (Ed.), China, 2011 (in print).
- [160] BP. Fairand, AH. Clauer, BA. Wilcox, Metall. Trans. A 8A (1977) 119.
- [161] C. S. Montross, T. Wei, L. Ye, G. Clark, Y.-W. Mai, Int. J. Fatigue 24 (2002) 102.

-
- [162] C. Leyens, M. Peters (Eds.), *Titanium and Titanium Alloys, Fundamentals and Applications*, first ed., Weinheim, Germany, 2003, p. 65.
- [163] C. M. Brakman, *Appl. Cryst.* 16 (1983) 325.
- [164] C. M. Brakman, P. Penning, *Acta Cryst.* A44 (1988) 163.
- [165] Y. D. Wang, R. Lin Peng, X.-L. Wang, R.L. McGreevy, *Acta Mater.* 50 (2002) 1717.
- [166] B. Clausen, T. Lorentzen, T. Leffers, *Acta Mater.* 46 (1998) 3087.
- [167] I. Nikitin, I. Altenberger, *Mater. Sci. Eng. A* 465 (2007) 176.
- [168] R. Stephens, A. Fatemi, R. R. Stephens, H. O. Fuchs, *Metal Fatigue in Engineering*, second ed., Wiley-Interscience, New York, 2001, pp 80.
- [169] L. Wagner, M. Mhaede, M. Wollmann, I. Altenberger, Y. Sano, *Struct. Integr.* 2–2 (2011) 185–199.

Curriculum Vitae

Personal Information

Surname, name: Maawad, Emad Kamel Soliman
Sex: Male
Date of birth: 25.08.1977
Place of birth: Alexandria, Egypt
Nationality: Egyptian
Marital status: Single
Current address: Onckenstrasse 13
D-22067 Hamburg
Tel.: +49 (0) 15 11 43 79 33 & +49 (0) 40 89 98 69 05
E-mail: emad.maawad@hzg.de
eksoliman@yahoo.com

Academic Qualifications

09/1996 – 05/2001 Bachelor degree
Production Engineering – Faculty of Engineering
Alexandria University – Egypt

09/2001 – 06/2006 M.Sc. degree
Production Engineering – Faculty of Engineering
Alexandria University – Egypt

11/2007 – 04/2012 PhD student
Institute of Materials Science and Engineering
Clausthal University of Technology – Germany

Employment

07/2002 – 09/2006 Demonstrator at the Production Engineering Department
Faculty of Engineering – Alexandria University – Egypt

09/2006 – 10/2007 Teaching assistant at the Production Engineering
Department, Faculty of Engineering – Alexandria
University – Egypt for the following courses:
- Materials Engineering
- Solid Mechanics
- Theory of Plasticity
- Machine Tools
- Forming Processes
- Design of Machine Elements
- Steel Making and Casting
- Welding Techniques
- Polymers and Composite Materials

Since 11/2007 Research assistant at the Institute of Materials Science and
Engineering – Clausthal University of Technology –
Germany

Since 07/2012

Research associate in the framework of *Energy Storage System* project – Helmholtz-Zentrum Geestacht Outstation at DESY

Research Experience

Residual stress and crystallographic texture measurement by using laboratory X-ray, energy-dispersive X-ray and neutron diffraction

In situ tensile test and phase analysis by using synchrotron radiation

Improvement of fatigue life of engineering materials by using mechanical surface treatments such as shot peening, ball-burnishing, ultrasonic shot peening and laser shock peening

Research Interests

Analysis of X-ray line profile to study micro-strains and crystal defects produced in surface layers after performing mechanical surface treatments on titanium alloys

Use of electron backscatter diffraction (EBSD) to study crystal orientation mapping, crystal defects and grain boundaries in titanium alloys after performing severe plastic deformation (SPD)

Finite elements method (FEM) to simulate traditional, ultrasonic shot peening and ball-burnishing processes

Optimizing laser shock peening parameters for various titanium alloys to improve fatigue lives

Investigation of thermal and mechanical stability of residual stress and crystallographic texture in mechanically surface treated titanium alloys during fatigue and creep tests

Work Responsibilities

Measurement of residual stress and crystallographic texture by using X-ray diffraction

Phase analysis of various alloys by using X-ray diffraction

Teaching assistant for “X-ray and Neutron Diffraction” course

Award

The Outstanding Student Award of the third International Conference on Laser Peening and Related Phenomena, hold in Osaka, Japan from 11 Oct. to 14 Oct., 2011.

EIDESSTATTLICHE ERKLÄRUNG

Hiermit erkläre ich an Eides Statt, dass ich die bei der Fakultät für Natur- und Materialwissenschaften der Technischen Universität Clausthal eingereichte Dissertation selbständig und ohne unerlaubte Hilfe verfasst und die benutzten Hilfsmittel vollständig angegeben habe.

Unterschrift

EIDESSTATTLICHE ERKLÄRUNG

Hiermit erkläre ich an Eides Statt, dass die eingereichte Dissertation weder in Teilen noch in Ihrer Gesamtheit einer anderen Hochschule zur Begutachtung vorliegt oder vorgelegen hat und dass ich bisher noch keinen Promotionsversuch unternommen habe.

Unterschrift